EXPERIMENTAL PROBING OF CHARGE AND VALLEY COUPLED SPIN DEGREES OF FREEDOM IN TWO-DIMENSIONAL TRANSITION METAL DICHALCOGENIDES

A Dissertation

Submitted to the Faculty

of

Purdue University

by

Terry Y.T. Hung

In Partial Fulfillment of the

Requirements for the Degree

of

Doctor of Philosophy

August 2019

Purdue University

West Lafayette, Indiana

THE PURDUE UNIVERSITY GRADUATE SCHOOL
STATEMENT OF DISSERTATION APPROVAL

Dr. Zhihong Chen, Chair

School of Electrical and Computer Engineering

Dr. Supriyo Datta

School of Electrical and Computer Engineering

Dr. Peide Peter Ye

School of Electrical and Computer Engineering

Dr. Joerg Appenzeller

School of Electrical and Computer Engineering

Approved by:

Dr. Dimitrios Peroulis

Head of the Graduate Program

ACKNOWLEDGMENTS

First and for most, I would like to thank my advisor Prof. Zhihong Chen who taught me how to be a careful independent researcher, how to always keep the reality and potential practical applications in mind while not losing the curiosity to science. It has truly been my great pleasure to work with her. She has always been supportive, warm and taking care of us in many ways. I would not achieve any of my works without her guidance. She allowed me the freedom to conduct and schedule my own experiments. The way she led the group made my PhD life much more joyful and I am extremely thankful and lucky for being part of her group.

Besides my advisor, I would also like to thank my committee members, who are so talented and yet patient enough to educate us. Prof. Supriyo Datta, I started learning spin-related knowledge from his courses. His classes are one of the best that I have ever taken. His enthusiasm in teaching and insightful ideas are what I admire the most. Prof. Joerg Appenzeller, he has given me many fruitful suggestions that has turned out to be very critical to make my work complete. He taught us invaluable knowledge and experience on low-dimensional device physics. Prof. Peide Peter Ye, he utilized his sharp sense in the new materials to inspire me a lot.

I would like to thank Dr. Chia-Ching Lin who brought me into the group and introduced me to the field. He is not only my mentor in research but also in my professional career. Dr. Kerem Y. Camsari, is my advisor in friends. He not only taught me professional knowledge but also how to deal with many non-scientific things in academia. I would also like to acknowledge Prof. Pramey Upadhyaya, who provided me a lot of his strong theoretical support. I would also like to thank my research

buddies, Punyashloka, Sam, Feng, Peng, Tingting and many others. They are so talented and friendly which are rarely seen in one person.

I cannot express enough how much I love my dearest family, my mom and dad. They have continuously supported me unconditionally and raised me in an environment that is full of love, trust, and respect. Lastly, I would like to give a special shout out to my lovely girlfriend Phoebe Lee, who cheered me up and stood by my side all the time. She helped me overcome at my lowest and celebrate with me at my cheery moment. She is even prouder of my achievement for me than myself.

TABLE OF CONTENTS

Page

LIST OF FIGURES

Figure Page

Figure Page

Figure Page

Figure Page

ABSTRACT

Hung, Terry Y.T. PhD, Purdue University, August 2019. Experimental Probing of Charge and Valley Coupled Spin Degrees of Freedom in Two-Dimensional Transition Metal Dichalcogenides. Major Professor: Zhihong Chen.

Charge degree of freedom has been successfully manipulated in the semiconductor industry over the past few decades. The trend of doubling the number of transistors every two years in each chip was observed by Gordon Moore at 1965 and this observation was named after him, Moores law. People have kept up with the prediction fairly well till very recently when the fundamental physics limitations has reached in the conventional Si-based devices. All variety of materials and different degrees of freedom are being explored intensively to make novel device designs to overcome this challenge. In this dissertation, we will focus on two-dimensional transition metal dichalcogenides (TMDs) materials and explore not only charge but also valley and spin degrees of freedom. 2D TMDs have attracted a lot of attention for many reasons and one of them is their superior electrostatic control due to the lowering of dimensionality from 3D to 2D. Such reduction of the dimensionality besides the easiness of doping, on the other hand, makes good metal contact harder to achieve due to its inert surface comparing to the existing Si technology. To evaluate the possibility of being one of the promising candidates of post-CMOS (complementary metal oxide semiconductor) devices, the access to both electrons (conduction band) and holes (valence band) is required in order to make CMOS devices. Fermi-level pinning in these materials, however, severely limits the tunability of the Fermi level alignment between metal and semiconductor by choosing different metal work functions. In Chapter 2, we will discuss our results on making good contact by lowering the Schottky barrier height and having atomically precise doping layer control and its associated doping

level where we also achieved the record high hole branch current at the bias voltage of -1V. Besides the manipulation of charge degree of freedom, we also explored and demonstrated the unique valley degree of freedom that can be electrically generated and detected for the first time in Chapter 3. Many fascinating properties of valley physics can be analogized to spin physics, such as, zero dissipation pure spin/valley current and binary nature (spin +1/2 and -1/2, valley K and K'). Due to the unique lattice structure in TMDs, monolayer particularly, the inversion symmetry is intrinsically broken which lifts the Kramers degeneracy and leads to non-zero Berry curvature. As a result, it possesses valley Hall effect. Even more interestingly, when the transport carriers are in the valence band of monolayer TMDs, spin and valley are locked and it is called spin-locked valley Hall effect. Owing to the nature of being 2D materials, these spins' polarization is out-of-plane unlike the conventional spin Hall effect materials, such as Pt, Ta, and W, where spins are polarized in the surface plane. This out-of-plane polarization is particularly favorable in the SOT-magnetic random access memory (SOT-MRAM) applications due to the lowering of critical switching current and consequently the reducing of power consumption. We directly observed this spin-locked valley Hall effect for the first time and we will discuss it in Chapter 4.

1. INTRODUCTION

1.1 Brief History of Hall effects

The discovery of ordinary Hall effect can be traced back to 1879. Edwin Hall, a PhD student in Physics at Johns Hopkins University, performed the measurements of potential difference on the opposite sides of a thin gold leaf under perpendicular magnetic field with current flowing in the material. This effect, later on, was named after him, a well-known, Hall effect. People have used the Hall measurement configuration, namely driving current in y direction and measuring voltage in x direction in the presence of magnetic field, in various systems including ferromagnets, 2DEG, semiconductors, two dimensional materials and so on resulting many significant findings not only in scientific interests but also practical applications. Moreover, in some of the systems, typically those with large spin orbital coupling, have the Hall-like effect even in the absence of external magnetic field. In general, the systems with certain type of carrier imbalance accumulated (chemical potential difference) on the opposite sides transverse to the applied current or electric field are called some kind of Hall effect, such as spin Hall effect and valley Hall effect. To take closer look of the large Hall family, some of them will be addressed in the following sessions.

1.1.1 Ordinary Hall Effect, Anomalous Hall Effect, and Quantum Hall Effect

Ordinary Hall effect (OHE) In order to distinguish the original Hall effect discovered by Edwin Hall from many other Hall effects that came later, people sometimes refer the former one as ordinary Hall effect (OHE). In the electromagnetism, the force experienced by the electrons is governed by the Lorentz force described in Eq. 1.1

where **F** is the force, **E** is the electric field, and **B** is the magnetic field perpendicular to the **xy** plane.

$$\mathbf{F} = q\mathbf{E} + q\mathbf{v} \times \mathbf{B} \tag{1.1}$$

Eq. 1.1, in the steady state, equals zero, as a result, $E_y = v_x B_z$. Taking the geometry into account and I_x equals flux into charge, one can find the Hall voltage V_H as shown in Eq. 1.2.

$$\mathbf{V_H} = \frac{I_x B_x}{nte} \tag{1.2}$$

As a powerful method, sheet carrier concentration (n) and Hall mobility (μ_H) can be extracted from the Hall measurements with the relations described in Eq. 1.3

$$\frac{1}{en} = \frac{dR_H}{dB}, \quad \mu_H = \rho \, \frac{dR_H}{dB}, \quad where \; R_H = V_H/Ix, \tag{1.3}$$

This method can also be used inversely with pre-characterized Hall resistance with respect to the magnetic field and is called Hall sensor. In other words, one can use it as a magnetic field sensor to detect the magnetic field spatially by measuring the responding Hall voltage.

Anomalous Hall Effect (AHE)

In ferromagnets, conducting the same measurement as ordinary Hall effect, one will observe a much steeper slop within the small magnetic field range and ODE slope superposed on it [1]. Depending on weather the ferromagnet has in-plane magnetic anisotropy (IMA) or out-of-plane/perpendicular magnetic anisotropy (PMA), Hall measurements will possess hysteresis free and hysteresis loop shown in Fig. 1.1 and Fig. 1.2 respectively . In the IMA magnets, hysteresis free and continuous change occurs in the low magnetic field region (in our case, $-0.8T < B < +0.8T$) due to the magnetization in z direction ($\mathbf{m_z}$) of the IMA magnet being pulled toward out-of-plane continuously. In the PMA magnet, on the other hand, shows a hysteresis loop with sharp switching behavior within low magnetic field (in our case, $-170Oe < B < +170Oe$) due to the field induced magnitization switching in z direction. OHE slope in both cases superimposes on the steeper slope described above and can be seen more clearly in the larger B-field regions when m_z is saturated. This extra effect, beyond

the straight line in OHE, can be described by the second term in Eq. 1.4 where ρ_H is Hall resistivity, R_o is related to the carrier concentration, and R_s is extraordinary Hall constant which is responsible for the steeper slope in IMA or sharp switching in PMA. Note, R_s is usually much larger than R_0 resulting a significant change in the slope.

$$\rho_{\mathbf{H}} = R_o B_z + R_s 4\pi M_z \tag{1.4}$$

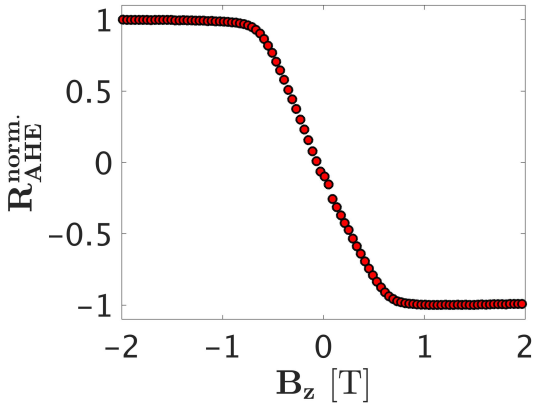

Fig. 1.1. Anomalous Hall effect measurement on Py (IMA) Hall cross shape device.

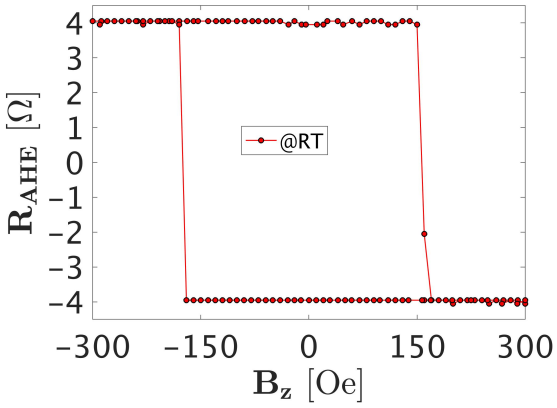

Fig. 1.2. Anomalous Hall effect measurement on CoFeB (PMA) Hall cross shape device.

Quantum Hall Effect (QHE)

Beyond ODE and AHE, when the applied magnetic field is very large, typically in the range of 10T, many fascinating effects show up and that is called quantum Hall effect. Nobel prizes were awarded to Klaus von Klitzing for integer quantum Hall effect and jointly to Robert B. Laughlin, Horst L. Strmer and Daniel C. Tsui for fractional quantum Hall effect. That is no need to emphasize the importance of quantum Hall effect in physics. Let us have a brief discussion to understand the concept of it. First of all, quantum Hall effect measurement can be conducted in the exact same configuration as ordinary Hall effect. What determines if one can measure the quantum Hall effect beyond ordinary Hall effect? There are two key quantities, mobility and the magnitude of out-of-plane magnetic field. They are bounded together. You can phenomenologically think of the multiplication of them needs to be larger than some value in order to observe QHE. Consequently, the material either has very high mobility or the measurement tool has the capability of applying high enough magnetic field. First, to achieve high mobility, people usually minimize the impurity in the material (extremely pure), reduce the material dimensionality, and lower the temperature. Graphene with the mobility higher than $10^4 cm^2 V^{-1} s^{-1}$ at 1.7K makes it one of the ideal materials to observe quantum Hall effect [2]. Second, quantized ρ_{xy} values are observed due to the separation of Landau levels. Moreover, they match precisely to the multiplication of integer filling factor and the fundamental resistant value h/e^2. Despite of the carrier materials and filling factor, it can be as precise as to the level of a few parts in 10^{10}. Third, ρ_{xy} shows Shubnikovde Haas oscillation and reaches zero resistivity due to the spatially separated positive and negative density of states which, consequently, highly suppress back scatterings.

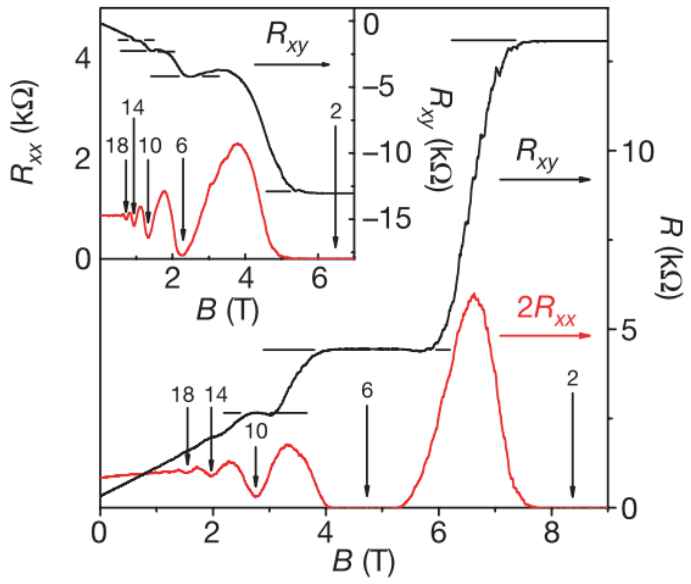

Fig. 1.3. Quantum Hall effect measurements on graphene device. reprinted by permission from Nature Research Publishers : Nature [2], Copyright 2005

1.1.2 Spin Hall Effect

Unlike the above-mentioned Hall effects, external magnetic field is not involved in spin Hall effect (SHE). To separate spins polarized oppositely to the opposite direction, there are two big groups of possible mechanisms, namely intrinsic and extrinsic SHE. The former one is attributed to the band structure which is in the absence of scattering and was predicted theoretically [3, 4]. Those predictions were also observed experimentally [5,6](Also Ch4 in this dissertation). On the other hand, the later one is associated with the asymmetric scattering of up and down spins. It was not drawing a lot of attention for the practical applications, due to very small Hall angel which is corresponding to the efficiency of charge to spin conversion, until relatively large Hall angle was reported in Pt, Ta, and W at room temperature [7–9]. Giant spin Hall effect measured in Ta at room temperature with both IMA and PMA magnetic tunnel junctions (MTJs) on top of it inspires great interests among physics

and engineers. Despite of the unsettled underlying physics, pure spin current is the composition of spin up electrons flowing in one direction while spin down electrons flowing in the opposite direction resulting charge current free. This can be expressed by Eq. 1.5 where $\mathbf{I_c}$ is charge current, $\mathbf{I_s}$ is spin current, and $\mathbf{I_{up}}/\mathbf{I_{up}}$ are spin up current and spin down current.

$$\begin{aligned} \mathbf{I_c} &= \mathbf{I_{up}} + \mathbf{I_{dn}} \\ \mathbf{I_s} &= \mathbf{I_{up}} - \mathbf{I_{dn}} \end{aligned} \tag{1.5}$$

Not only its rich physics but also the promising engineering ways to tailor the next generation devices have attracted a lot of attention. For example, spin-orbit-torque-magnetic random access memory (SOT-MRAM) has been considered as a more efficient way to manipulate memory bits compared to spin-transfer-torque-magnetic random access memory (STT-MRAM) for many reasons. Lower critical switching current is one of them and better durability is another due to more efficient use of spins and not requiring large current passing through MTJ tunneling layers.

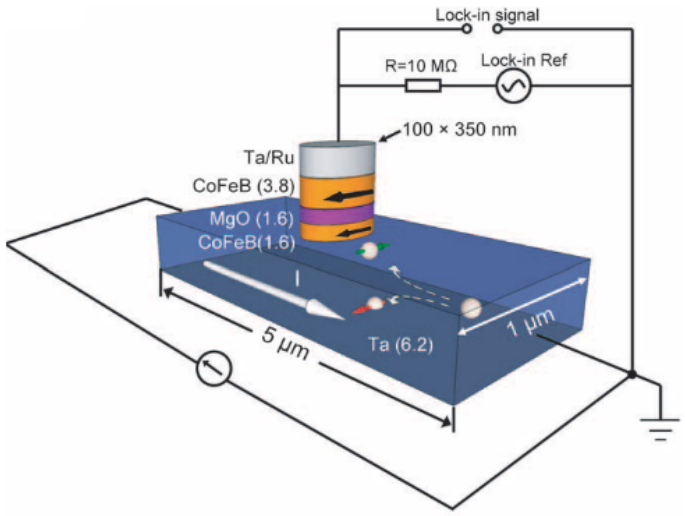

Fig. 1.4. Three-terminal device including SHE material (Ta) and MTJ. From [9]. Reprinted with permission from AAAS

1.1.3 Valley Hall Effect and Inverse Valley Hall Effect

Besides charge and spin degree of freedoms, here, we will introduce another degree of freedom from the orbital angular momentum, called valley. In certain type of materials (we will come to it in the later sections), similar to spins' spin up and spin down, there are two kinds of valleys and we will refer them as K and K'. Moreover, valley current can also be described in the same way as Eq. 1.5 with spin up and spin down being replaced by K and K' shown in Eq. 1.6.

$$\begin{aligned} \mathbf{I_c} &= \mathbf{I_K} + \mathbf{I_{K'}} \\ \mathbf{I_v} &= \mathbf{I_K} - \mathbf{I_{K'}} \end{aligned} \tag{1.6}$$

Unlike spins that are originated from spin angular momentum, valleys normally won't be affected by the applied external magnetic field since the original internal effective magnetic field is way too stronger than the external magnetic field that is applicable. To select and detect valley in the optical fashion, circularly polarized light and magneto optical Kerr effect (MOKE) are widely used. As we mentioned above, valley is coming from the orbital angular momentum and thus has angular momentum of -1, 0, and 1. As a result, left/right-handed circularly polarized (LCP/RCP) light that has angular momentum of -1 and 1 couples to valley degree of freedom. Let me briefly talk about what are the LCP and RCP. Suppose you have two linearly polarized electromagnetic waves and you superimpose them with phase shift of angle ϕ. Depends on the shifted angle ϕ, one will have linearly polarized light when $\phi = 0, \pm\pi$, LCP or RCP light when $\phi = \pm\pi/2$, and elliptic polarized light when $\phi = otherwise$. Reversely, a linearly polarized light is a superposition of LCP and RCP with the same magnitude. Thus, when the linearly polarized light reflects from the valley materials, it will change the originally 50-50 percent LCP and RCP to other percentage to the different absorption of them which allows one to detect valley degree of freedom. This coupling mechanism is widely used to select and detect valley degree of freedom [10–16]. In addition to the above-mentioned optical methods, manipulating

valley degree of freedom electrically can also be achieved and it will be the focus of this dissertation. This is called valley Hall effect (VHE). VHE has been theoretically studied and experimentally measured. What is valley Hall effect? Like many other Hall effects, valleys will be separated transversely when current is applied longitudinally. Furthermore, many properties can be almost one to one mapped from spin Hall effect by simply replacing spin Hall angle and spin diffusion length with valley Hall angle and inter-valley scattering length respectively. Although the fundamental physics might be vastly different between spin Hall and valley Hall effect, especially extrinsic spin Hall effect, many well-known phenomena can still be adopted. Note, normally in most of the spin Hall effect systems, Hall angle is not comparable to one; as a result, some assumptions are reasonably made, e.g. only taking first order effect on Hall angle, take approximation of $tan^{-1}(\theta_{SHE}) \sim \theta_{SHE}$. In valley Hall systems, however, Hall angle can be comparable or even exceed unity. Therefore, second order effect needs to be taken care of and the approximation needs to be modified. Here we will focus on two dimensional materials such as graphene and TMDs. In such materials, K and K' inequivalent valleys located at the band edges dominate the electronic transport. Furthermore, in the absence of inversion symmetry, these materials carry a non-zero Berrys curvature (Ω) which I will come to more details later in the section 1.2. Ω acts like an effective magnetic field and results in the development of an anomalous velocity component (v) for carrier transport that is transverse to the applied electric field (E), i.e. $v \propto \Omega \times E$. Importantly, K and K' valleys are correlated by time reversal symmetry, under which Berrys curvature flips its sign, i.e. $\Omega(K) = -\Omega(-K)$. Consequently, K and K' valleys develop opposite v, providing a route to electrically generate pure valley-coupled topological currents transverse to an applied electric field (schematic of this phenomenon is depicted in Fig. 1.5, occurring in the left electrode of the Hall bar). Analogous to the spin current, such pure valley current comprises of carriers of opposite (valley) polarization moving along the opposite directions (resulting in charge neutral valley carrier transport along the x axis in Fig. 1.5). Onsager reciprocity [17] then ensures the reciprocal effect, a phenomenon

defined as inverse valley Hall effect (iVHE). Namely, a non-zero valley current results in a built-up of an electric field transverse to the direction of the valley current and the corresponding voltage difference across the right electrode of the Hall bar in Fig. 1.5.

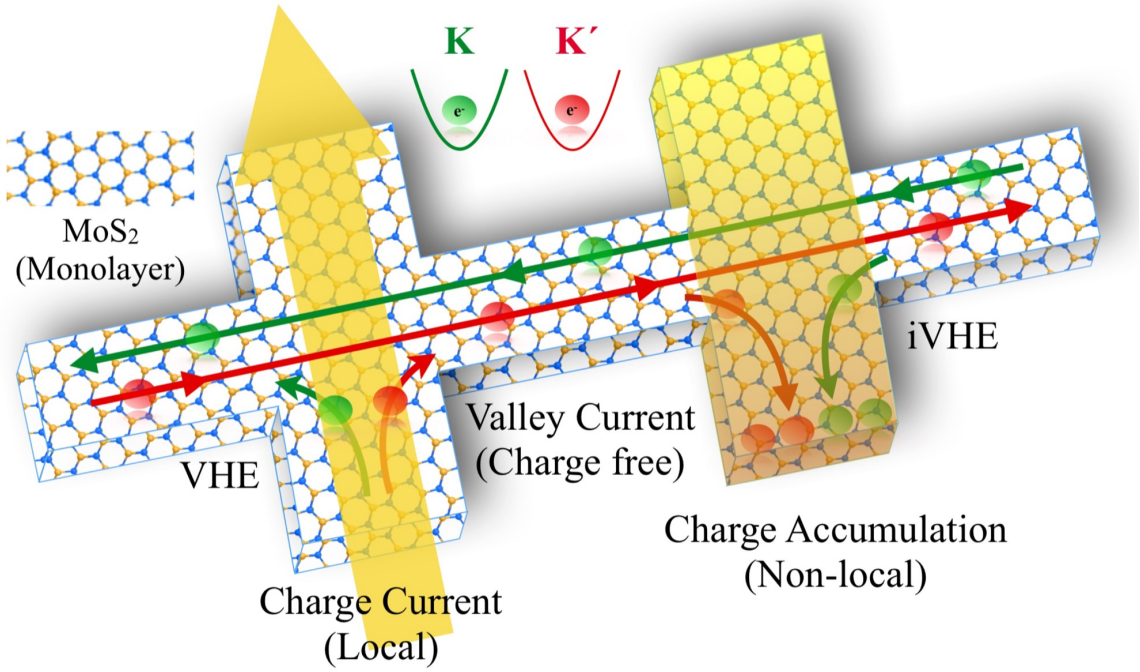

Fig. 1.5. Schematic of valley current due to VHE and iVHE in monolayer MoS_2 [18].

1.2 Time Reversal Symmetry and Inversion Symmetry

In two dimensional materials such as graphene and transition metal dichalcogenide (TMDs), consist of two inequivalent valleys K and K' shown in Fig. 1.6. Under time reversal symmetry, Berry's curvature denoted as Ω follows $\Omega(K) = -\Omega(K')$. Besides, inversion symmetry insures $\Omega(K) = \Omega(K')$. Clearly, the only solution for Ω under the presence of both symmetries is trivial solution, $\Omega = 0$. In order to have non-trivial solution for Ω, one of the symmetries needs to be broken. Similarly, the energy of spin up and down can be shown as $E^{up}(K) = -E^{dn}(K')$ and $E^{up}(K) = E^{dn}(K')$ due to time reversal symmetry and inversion symmetry respectively and it is called Kramer's degeneracy. This can be lifted if inversion symmetry is broken. Therefore, spins are no longer degenerated. In this dissertation, I will focus on two dimensional systems with broken inversion symmetry.

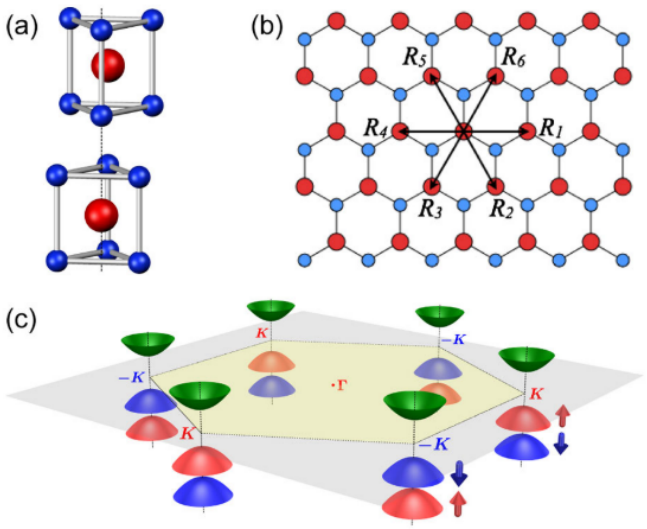

Fig. 1.6. (a) The unit cell of bulk 2H-MoS_2, which has the inversion center located in the middle plane. It contains two unit cells of MoS_2 monolayers, which lacks an inversion center. (b) Top view of the MoS_2 monolayer. R_i are the vectors connecting nearest Mo atoms. (c) Schematic drawing of the band structure at the band edges located at the K points. Reprinted figure with permission from [10] Copyright (2012) by the American Physical Society.

1.2.1 Berry Curvature

There are few ways to break the inversion symmetry. In graphene, for example, inversion symmetry can be broken by stacking a sheet of BN on top of single layer graphene and they form a supperlattice structure [19] or applying perpendicular electric field through bilayer graphene [20, 21]. To those who are familiar with bandgap engineering in bilayer graphene, opening bandgap with perpendicular electric field will come along with the broken inversion symmetry, i.e. $\Omega \neq 0$. In TMDs, however, inversion symmetry is intrinsically broken in the monolayer and, in principle, in odd number of layers as well. The Ω strength in monolayer TMDs is shown in Fig. 1.7. The Bulk or even number of layers will recover its inversion symmetry. That results again in trial solution for Berry's curvature. It is worth mentioning that in TMDs, increasing layer number from monolayer to any other layers will change the transporting bands. In other words, K valleys contribute to the electrical transport in monolayer while Γ and between K and Γ will take over for in layer other than monolayer. Applying perpendicular magnetic field in bilayer TMDs has also been demonstrated similar to the bilayer graphene mentioned above.

In the systems mentioned above with broken inversion symmetry, group velocity in Eq. 1.7 alone is not sufficient to describe the system. $E \times \Omega$ induced velocity, as a result, is needed and can be called as an anomalous velocity which leads to topological current/valley current.

$$\mathbf{v_k} = \frac{1}{\hbar}\frac{\partial \epsilon_k}{\partial k} \; + \; \frac{qE}{\hbar} \times \Omega(k) \tag{1.7}$$

This extra Berry curvature induced term is similar to the magnetic field term in Lorentz force 1.1 and it can be taken as if it is a magnetic field but in momentum space. Moreover, due to K and K' valley carry Berry curvature with opposite sign, valley concentration imbalance will be accumulated on the opposite sides resulting the valley Hall voltage. Note, the valley Hall voltage is due to the imbalance of valley concentration not the charge concentration. This imbalance, therefore, cannot be detected through a voltmeter like people did in ordinary Hall effect. Valley

Hall conductivity denoted σ_{xy}^{VH} as a result of imbalanced valley concentration can be calculated by Eq. 1.8.

$$\sigma_{\mathbf{xy}}^{\mathbf{VH}} = \mathbf{2}\,\frac{\mathbf{e^2}}{\hbar}\int_{\mathbf{BZ}}\frac{\mathbf{d^2k}}{\mathbf{(2\pi)^2}}\,\mathbf{f(k)}\,\mathbf{\Omega(k)} \tag{1.8}$$

As mentioned previously, valley Hall imbalance is not like charge imbalance which can be detected by a voltmeter in the ordinary Hall effect system. In this section, we will discuss two types of detection method, namely optical and electrica methods. In optical method, circularly polarized light can be used to select and detect valley degree of freedom, e.g. LCP will excite valley K and RCP will excite valley K', where LCP and RCP are the short hand writing for left-circular polarized light and right-circular polarized light respectively. Electrical method, on the other hand, will require reciprocal effect, namely inverse valley Hall effect (iVHE). As long as time reversal symmetry is preserved, the reciprocal effect iVHE will always come along with VHE. Through careful device design, therefore, charge imbalance can be induced by first converting charge current into topological current (valley current) through VHE, second, converting topological current back to charge current through VHE and last being detected nonlocally due to the build up potential difference shown in Fig. 1.5.

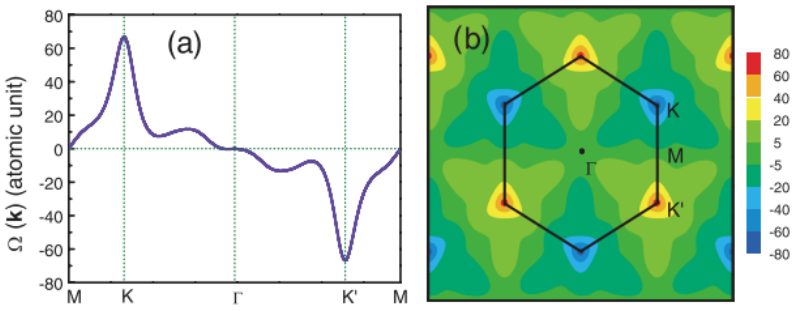

Fig. 1.7. The Berry curvatures of monolayer MoS_2 along the high-symmetry lines (a) and in the 2D k plane (b). The spin Berry curvatures of monolayer MoS_2 along the high-symmetry lines. Reprinted figure with permission from [22] Copyright (2912) by the American Physical Society.

1.3 Two-dimensional Transition Metal Dichalcogenides

"What could we do with layered structures with just the right layers" asked by Richard Feynman in one of his famous lectures in 1959. In this section, hopefully we can understand some of the aspects that could make us closer to the answer. Two-dimensional materials normally have strong in-plane covalent bonds and are stacked through weak out-of-plane van der Waals force. This property enables us to exfoliate it from the bulk form and obtain few layers to even monolayer. The reduction of dimensionality gives rise to many amazing properties. Graphene, for example, considered to be the mother of 2D materials exists many relativistic phenomena, such as mass less quasiparticle, non-trivial Berry phase, half-integer shift in QHE, etc... However, when it comes to the semiconducting industry applications, lack of bandgap makes it somewhat less useful. On the other hand, 2D Transition Metal Dichalcogenides (TMDs) with the bandgap on the order of $1eV$ have attracted a lot of attention due to their exceptional properties and the compatibility to the semiconductor industry. Due to the nature of 2D materials, stacking one with dissimilar others allows researchers to create all kinds of heterostructures and leads to a wild range of complicated outcomes just like how one can use Lego to create various beautiful things. In this section, we will focus on the electrical applications and the unique spin-valley locking effects in TMDs.

1.3.1 Charge Degree of Freedom

Charge degree of freedom is a key aspect in the logic CMOS devices. Manipulating charge carriers through three terminal configuration, namely source, drain, and gate, consists of all kinds of engineering challenge. Over the past few decades, people have spent a lot of efforts to keep Moore's law going. It has been an amazingly successful story of the history. This progressive scaling is approaching the physical limitation as the length or width approaching $5nm$. To keep on improving it, new materials need to be introduced. TMDs with atomically smooth surface without dangling bond and

the bandgap on the order of $1eV$ makes it a very promising candidate. The bandgap of it changes from indirect to direct when the number of layer becomes one from anyother layer numbers shown in Fig. 1.8 [23]. This makes particular interests to many optical and optoelectrical applications. The atomically thin channel thickness gives rise to an excellent electrostatic control which is extremely important to the device scaling and low power device applications. This 2D nature, on the other hand, makes the good contact non-trivial and severely hinder their encouraging intrinsic properties. Fermi-level pinning between metal and TMDs channel materials makes it even harder due to the deviation from Schottky-Mott limit [24]. For example, in MoS_2, Fermi energy alignment in the contact channel interface is pinned to be closer to the conduction band [25]. As a result, it shows unipolar behavior and is irrespective of the metal work function selection. Another example is WSe_2, where the Fermi energy is pinned almost in the middle of the bandgap and shows ambipolar behavior. Contact resistance, as a result, is one of the bottle necks that needs to be overcome. Since 2012 or so, tremendous efforts all over the world have been put to tackle this problem. Let me briefly address some of the possible solutions. First, utilizing different TMDs phase can drastically reduce the contact resistance [26]. In TMD materials, 2H is a semiconducting phase while 1T is a metallic phase shown in Fig. 1.9. Therefore, integrating 1T phase TMDs underneath the contact while leaving the channel to be 2H phase to preserve its semiconducting behavior has been demonstrated to have very low contact resistance of 240Ω. Second, combing semi-metal graphene and TMDs to form a vertical heterostructure is also used to reduce the contact resistance [27]. Third, de-pinning the Fermi level alignment by inserting an oxide as a buffer layer or peel the metal and transfer it to the TMDs channels [24,28]. Last, chemical doping is also widely adopted to achieve lower channel resistance and the reduction of contact resistance [29–31]. In section 2, we will show our atomically precise doping method which can give rise to the control of doping level as well as lower contact resistance (more transparent Schottky contact). More importantly, it is an air stable doping.

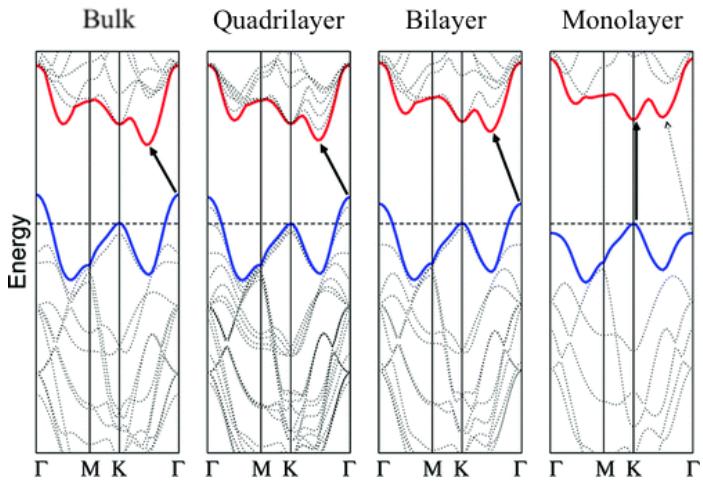

Fig. 1.8. Calculated band structures of (a) bulk MoS_2,(b) quadrilayer MoS_2,(c) bilayer MoS_2, and (d) monolayer MoS_2. The solid arrows indicate the lowest energy transitions. Bulk MoS_2 is characterized by an indirect bandgap. The direct excitonic transitions occur at high energies at K point. With reduced layer thickness, the indirect bandgap becomes larger, while the direct excitonic transition barely changes. For monolayer MoS_2 in d, it becomes a direct bandgap semiconductor. This dramatic change of electronic structure in monolayer MoS_2 can explain the observed jump in monolayer photoluminescence efficiency. Reprinted with permission from [23]. Copyright (2010) American Chemical Society.

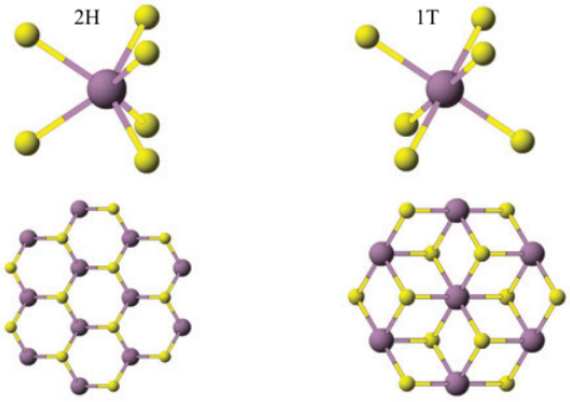

Fig. 1.9. Crystal structures of the 2H and 1T phases, respectively. Trigonal prismatic (left) and octahedral (right) coordinations are shown. Reprinted by permission from Springer Nature: Nature Materials [26], copyright (2014)

1.3.2 Spin and Valley Degrees of Freedom

Besides the charge degree of freedom that has been used successfully as the binary units to store and process information, spin degree of freedom has also attracted and actually implemented for the same purpose due to the spin fermion nature, i.e. spin +1/2 and -1/2. In addition to graphene's superior electron properties, extremely low spin-orbital torque (SOT) makes it an excellent spin propagating material where the spin-flip length λ_s can be as high as few tens of μm. Usually, non-local lateral spin valve [32,33] is used to characterized the spin related material properties, such as polarization in the interface of ferromagnet and channel and spin-flip length λ_s. In this type of measurement, in-plane magnetic field (along the easy axis of the magnet) is applied to flip the electrodes one by one and the step-wise non-local resistance due to different amount of spins get accumulated underneath the injection and diffuse to the detector can be resolved. Alternatively, out-of-plan magnetic field can also be used to perform the so-called Hanle measurement where the spins that are perpendicular to the applied magnetic field will precess around it as a function of the field's magnitude.

$$\begin{aligned} \mathbf{I_{up}} &= -\frac{\sigma \mathbf{A}}{\mathbf{2q}} \frac{\mathbf{d}\mu_{\mathbf{up}}}{\mathbf{dz}} \\ \mathbf{I_{dn}} &= -\frac{\sigma \mathbf{A}}{\mathbf{2q}} \frac{\mathbf{d}\mu_{\mathbf{dn}}}{\mathbf{dz}} \end{aligned}$$

$$\frac{\mathbf{d^2}\mu_{\mathbf{up}}}{\mathbf{dz^2}} = \frac{\mu_{\mathbf{up}} - \mu_{\mathbf{dn}}}{\mathbf{2}\lambda_{\mathbf{s}}^{\mathbf{2}}} = -\frac{\mathbf{d^2}\mu_{\mathbf{dn}}}{\mathbf{dz^2}} \tag{1.9}$$

$$\lambda_{\mathbf{s}} = \sqrt{\sigma \mathbf{A}/\mathbf{4qK}}$$

Valley degree of freedom which can be analogized to spin in many aspects has been explored intensively over the past few years. Valleys K and K' can be represented by the pseudo-spin up and down respectively. As a result, just like spins, valleys can be used as a binary element. These binary pseudo-spins can be optically excited and

detected. The circularly polarized light couples to the inter-band transition within K and K' valleys through right-handed circularly polarized light (RCP) and left-handed circularly polarized light (LCP) denoted as $\sigma+$ and $\sigma-$ respectively. The corresponding valley polarization is defined as

$$\eta = \frac{\mathbf{PL}(\sigma+) - \mathbf{PL}(\sigma-)}{\mathbf{PL}(\sigma+) + \mathbf{PL}(\sigma-)} \tag{1.10}$$

In MoS_2, the coupling of circularly polarized light and valley degree of freedom has been demonstrated by Zeng et al. and Mak et al. [12, 13]. In both works, circularly polarized light was used to excite the exciton within K or K' valley depending on which handedness was used and detected the photoluminism (PL) after the recombination process. The valley polarization defined in Eq. 1.10 is then used to quantify it. Combing this selection rule with VHE and iVHE in section 1.1.3, Mal et al. used polarized light to populate the imbalanced valley carriers in the Hall cross junction. Electric field is then applied longitudinally in the MoS_2 FET-like device and the charge imbalance is accumulated transversely due to the valley Hall current in the transverse direction. In bilayer MoS_2, Lee et al. [15] spatially resolves the Kerr signal reflecting the valley carriers accumulation along the edges where one type of carrier goes to one edge while the other goes to the opposite edge when the electric field is applied. Although bilayer MoS_2 is considered to have recovered inversion symmetry in which the VHE does not exist, the perpendicular electric gating field was applied to break the symmetry.

Despite of many successful demonstrations through either optical or optoelectrical ways to manipulate valley degree of freedom, all electrical scheme remains unexplored till our work [18] on monolayer MoS_2 and Wu et al. [34]. Similar to graphene VHE works, non-local structure was patterned and charge current was applied on, for example, left pair to generate valley current transversely through VHE as shown in Fig. 1.5. Next, the valley current diffuses to the right pair and generate the charge imbalance longitudinally ensured by Onsager reciprocity [35], called iVHE.

Lastly, let me introduce another very physics-rich and yet having various very promising properties that can potentially be used in practical applications from monolayer TMDs family, WSe_2 particularly. Monolayer WSe_2's broken inversion symmetry in combine with the unique band structure inherited from strong SOT gives rise to the spin-locked valley Hall effect (SVHE). On top of all the promising properties in VHE systems, spins are now coupling to it. Due to the nature of two-dimensional systems, these spins are oriented perpendicularly to the transport plane and called out-of-plane spins. In SOT-MRAM type of applications, PMA magnet is desirable due to the better scalability and thermal stability. Out-of-plane spins have been wanted desperately to reduce the critical switching current which result in the lowering of power consumption. We are the first one who demonstrated SVHE in monolayer WSe_2 and directly probed the spin orientation through the interaction of the spins and the ferromagnet. Note, spin momentum and valley momentum are convoluted in the MOKE measurements. Therefore, to decouple and further probe them directly, all electrical measurement is needed. We will discuss more details in section 4.

2. ELECTRICAL PROPERTIES IN TMD MATERIALS

Part of the material in this chapter would be submitted for review, Terry Y.T. Hung, Chin-Sheng Pang, Xiangkai Liu, Dmitry Zemlyanov and Zhihong Chen, Atomically Thin p-doping Layer and Record High Hole Current on WSe_2 77th IEEE Device Research Conference (2019).

Part of the material in this chapter would be submitted for review, Terry Y.T. Hung, Chin-Sheng Pang, Ava Khosravi, Rafik Addou, Robert M. Wallace, and Zhihong Chen, Ultra-low Schottky Barrier Height and Strong p-doping in Direct O_2 Plasma Treated WSe_2 Devices

2.1 Introduction

Two-dimensional (2D) transition metal dichalcogenides (TMDs) that can be exfoliated from bulk crystals or obtained through high quality growth [36–40] have attracted significant attention due to their outstanding electrical, optical, chemical, and mechanical properties. Especially, excellent electrostatic control allowing for ultimate device scaling [41,42] and unique spin-valley coupling enabling novel valleytronic devices [10, 22, 43–45] are of particular interests in the consideration of extending the roadmap beyond CMOS. In this work, we focus on 2D field-effect transistor (FET) applications and chose tungsten diselenide (WSe_2) as our channel material because the accessibility of both electron and hole transport, which is ideal for CMOS implementation. However, substantially high contact resistance [46–50] associated with Schottky barriers (SBs) formed at the metal and semiconductor interface is one of the bottlenecks that impede device performance compared to theoretically predicted values in TMDs-based devices [51–53]. Furthermore, it has been found that metal Fermi-levels [54–57] are normally pinned in the WSe_2 band gap and the correspond-

ing SB height on the order of $\sim 300\ to\ 700meV$ is barely sensitive to the metal work function, i.e., deviating from the Schottky-Mott limit [24, 25]. Several approaches based on chemical doping are proposed to achieve higher current drive through channel doping and contact resistance lowering [29–31, 58, 59]. For instance, degenerate doping and contact resistance of $\sim 1.5k\Omega - \mu m$ were achieved through chemisorption of NO_2 on WSe_2 devices [31]; reduced SB height of $\sim 240meV$ to the valence band edge of WSe_2 was obtained via ozone exposure [30], and a contact resistance of $\sim 0.8k\Omega - \mu m$ along with a strong doping effect was realized by depositing MoO_3 as a dopant layer on WSe_2 [29]. All of these works, however, require a proper post-process channel passivation due to the lack of air stability. To date, only ref. [60] showed air-stable p-doping of WSe_2 using remote O_2 plasma. In this section, a direct O_2 plasma technique was applied to realize air stable p-doping in WSe_2 devices. Despite the direct exposure to plasma, no obvious device performance degradation was observed. In the following sections, comprehensive analyses from Raman, x-ray photoelectron spectroscopy (XPS) , and electrical measurements were carried out to understand the doping mechanism and evaluate the conversion of WSe_2 into WO_{3-x} in section 2.4. A precise one layer conversion is observed and supported by the vanishing interlayer interacting peak of B^1_{2g} Raman mode at 310 cm^{-1} after room temperature (RT) O_2 plasma treatment on bilayer WSe_2. Interestingly, the penetration of WO_{3-x} underneath devices contact regions is revealed, explaining the ultra-low Schottky-barrier (SB) height of $\sim 70meV$ for the hole transport which will be discussed in more detailed in section 2.2.

2.2 Hole Transport Enhancement

It is very clear in Fig. 2.3 that after direct O_2 plasma treatment at various temperatures, threshold voltages (V_th) shift towards right and the p-branch on-currents are enhanced by more than one order of magnitude. Different doping levels can be seen easily by comparing the shifting amount of transfer characteristics among

different treatment temperatures. The p-doping effect was further quantified by $Q = C_{ox}(\Delta\ V_{th})$ where Q is the charge density, $C_{ox} \sim 3 \times 10^{-4} Fm^2$ is the capacitance from the 90nm SiO_2 substrate, and ΔV_{th} is the threshold voltage shifting between the pristine and after O_2 plasma treatment. The p-doping levels ranging from $\sim 2.2 \times 10^{12}(cm^{-2})$ to $\sim 8.6 \times 10^{12}(cm^{-2})$ at room temperature and 150^oC treatment respectively were extracted. Moreover, among different temperature treatments, V_{th} shifting (doping level) increases with increasing treatment temperature. We believe that this behavior can be attributed to the different numbers of WO_{3-x} layers that leads to noticeable increasing p-type doping levels with increasing temperatures. Although the substoichiometric form (WO_{3-x}) was proven to have higher vertical conductivity compared to its stoichiometric form (WO_3) that is known to be an insulator37, we exclude the possibility that the on-current enhancement is due to the lateral shunting of WO_{3-x} for the following reasons. First, the treated devices were able to be completely turned off and showed on/off ratios exceeding 10^7. Second, we conducted another experiment with the same fabrication and treatment on pristine monolayer WSe_2. It shows clearly in Fig. 2.5 that the device after treatment conducts no current in the lateral direction since only the WO_{3-x} layer is left as the channel. This zero conductance along the lateral transport direction was also shown by Bilu Liu et al. [61].

From one to three orders of magnitude on-current enhancements were clearly observed in Fig. 2.3, which could potentially come from both/either channel doping (V_{th} shifting) and/or Schottky contact reduction. To identify the source of the improvement, we measured the change in contact and sheet resistance through 4 probe measurements of Type II devices, depicted in Fig. 2.1a. It is clear that the stronger the doping (more conversion layers with higher treatment temperature) the lower the contact resistance and the ratio of contact reduction ($\frac{R_c^{before}}{R_c^{after}}$) could be as drastic as changing from factor of six to more than two orders of magnitude. Such huge contact resistance reductions observed among different treatment temperatures show that

the treatment is not only affecting the channel region but also lowering the Schottky barrier height in which we will get into in the following section.

Output characteristics on behalf of our best-performed device is shown in Fig. 2.7 with the record high hole-current of 320 $\mu A/\mu m$ being achieved at V_{ds} of -1V. Finally, promising results among different treatment temperatures are air stable that are confirmed by exposing devices to the air ambient before re-measurements. A difference is negligible for the devices as shown in Fig. 2.4, even without any encapsulated layer on top of the WO_{3-x}, indicating a robust p-doping scheme for high performance electronics. Next, we fabricated a top-gated WSe_2 FET and utilized the direct O_2 plasma doping scheme to realize a genuine p-MOSFET. The S/D contacts were first defined on an exfoliated WSe_2 flake, followed by a lift-off process to form a gate stack of ALD HfO_2 and Ni electrode in the middle channel segment, with the gate underlapping the S/D by a distance of 250nm, as shown in Fig. 2.8a. In Fig. 2.8b, transfer characteristics of a pristine device show that current injection can be significantly modulated by varying the back-gate voltage (V_g). The hole injection is observed at $V_g = -40V$ (red dots curve), while the current is not detectable at $V_g = 0V$ (red triangles curve) due to the lack of sufficient contact gating to enable carrier injection. After the direct O_2 plasma treatment, WO_{3-x} was formed in the extended S/D regions by a self-aligned process. The enhanced hole current injection measured at floating V_g (no gating, blue curve) indicates a strong p-doping effect and a low contact resistance attributed to the intimate WO_{3-x} layer. Again, Fig. 2.8b shows no current degradation after the device being exposed to air for two weeks (green curve), suggesting good air-stability of the WO_{3-x} layer to maintain the doping strength in the extended S/D regions.

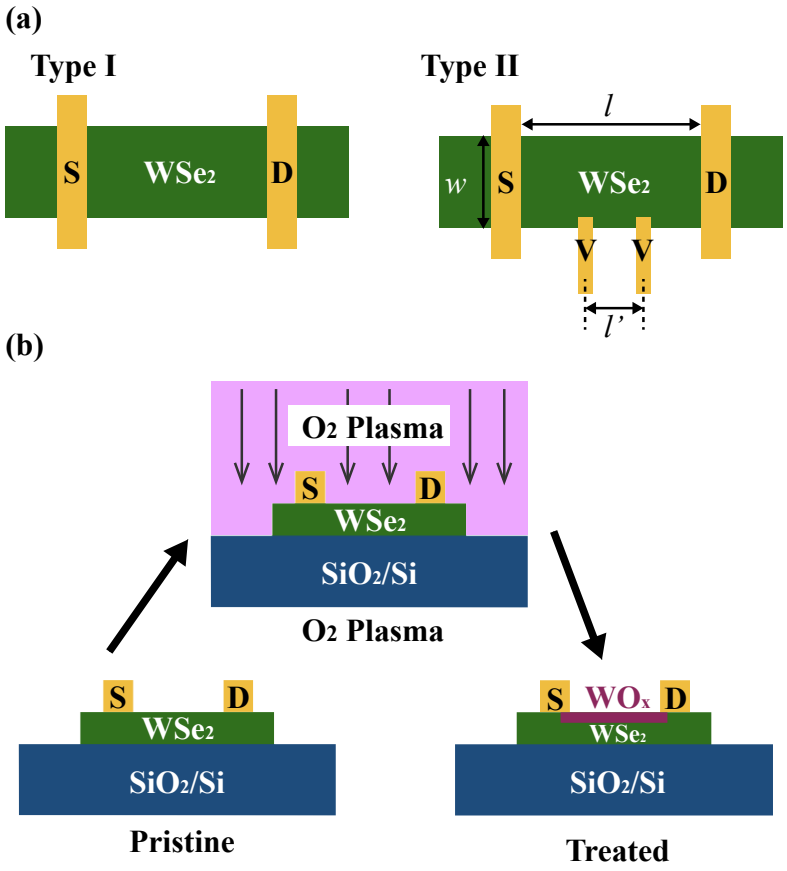

Fig. 2.1. (a) Illustrations of Type I and Type II devices. (b) Schematics of a WSe_2 device before and after being exposed to direct O_2 plasma at 150^{o}C for 1 min.

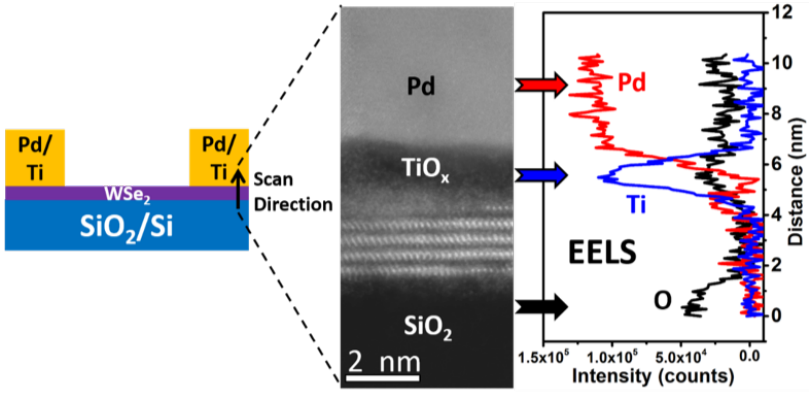

Fig. 2.2. HR-STEM and EELS line scan along the SiO_2/WSe_2/contact region.

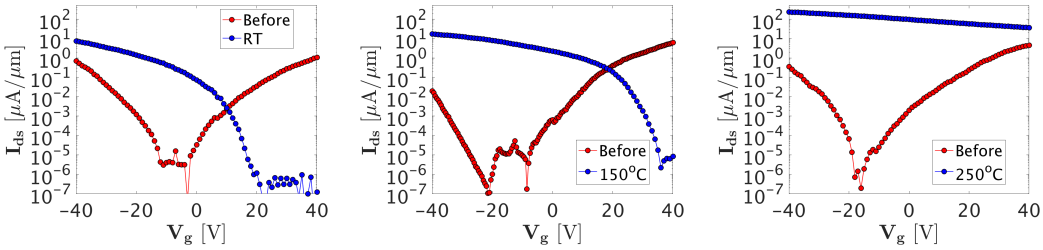

Fig. 2.3. Transfer characteristics comparison of pristine WSe_2 FETs and after O_2 plasma treatment at RT, 150^{o}C, and 250^{o}C.

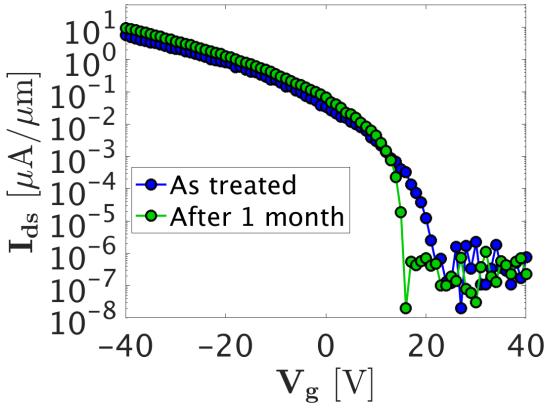

Fig. 2.4. Transfer characteristics measured after exposing to air for one month.

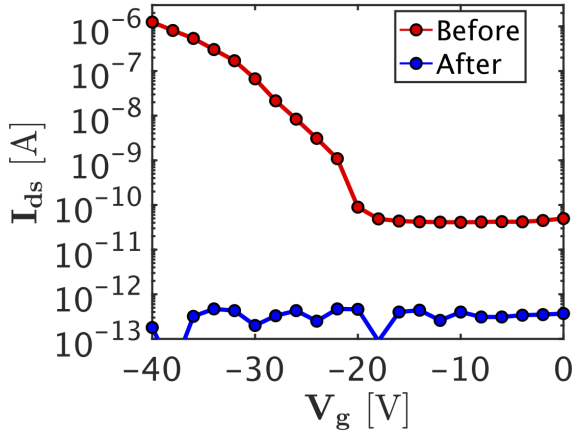

Fig. 2.5. Transfer characteristics on monolayer WSe_2 before and after the treatment. WSe_2 was converted to WO_x by the O_2 plasma treatment.

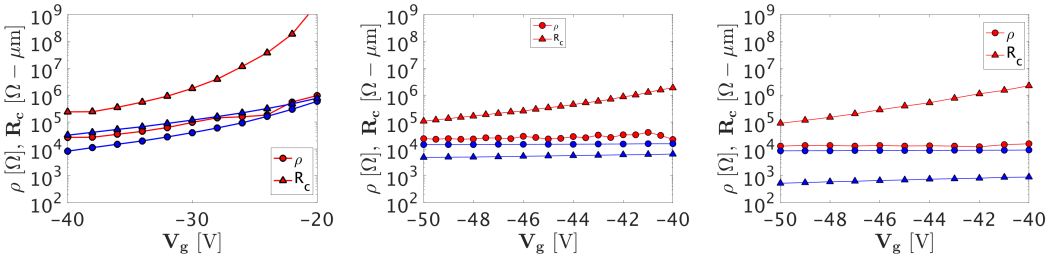

Fig. 2.6. Channel and contact resistances comparison of pristine WSe_2 and after O_2 plasma treatment at RT, 150^{o}C, and 250^{o}C. Red and blue are before and after treatment. Circles and triangles are resistivity and contact resistance.

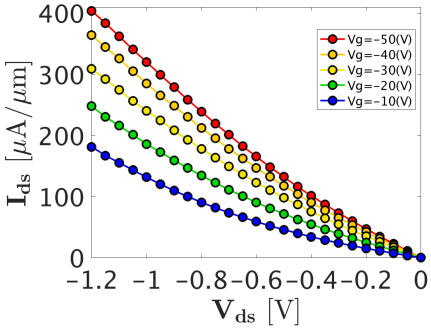

Fig. 2.7. Out-put characteristics at different V_g

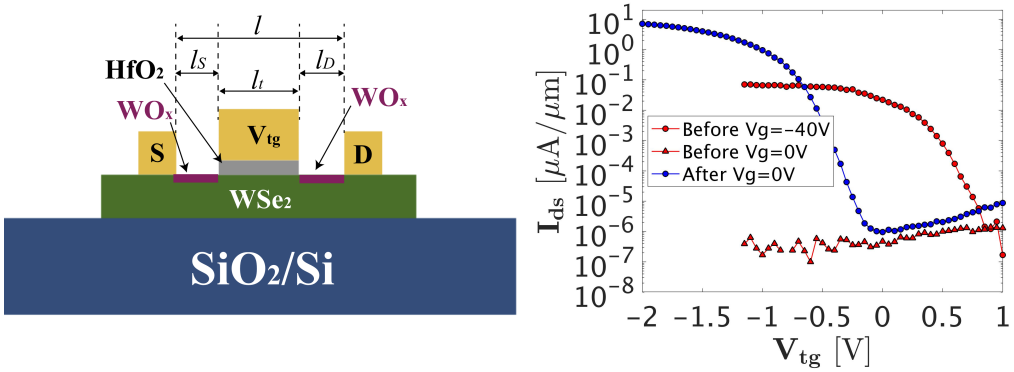

Fig. 2.8. On the left, schematic of a top-gated structure after the exposure to 150^{o}C direct O_2 plasma. Device dimensions: l=0.6um, w=1um, l_t=0.1um, and l_S= l_D=0.25um. On the right, transfer characteristics at V_{ds} = -0.9V with V_g = -40V and 0V before and at V_{ds} = -0.8V with floating V_g after the O_2 plasma treatment (blue)

2.3 Schottky Barrier Height

Almost linear output characteristics in the low V_{ds} regime shown in Fig. 2.10 suggests a rather transparent Schottky contact formed between the metal and the WSe_2 channel. Indeed, the SB height was extracted to be as small as $\sim 70meV$ from the valence band edge. Fig. 2.11a shows a set of temperature dependent type I measurements that were used to extract SB height, through the same technique presented by Saptarshi Das et al. [25]. The effective barrier heights at any given gate voltages are shown in Fig. 2.11b, which were extracted from the Arrhenius plot of the current (I_{ds}) as a function of inverse temperature (1/T) at a given gate voltage (V_g) shown in Fig. 2.9 by a linear fitting using the conventional thermionic emission theory Eq. 2.1

$$\mathbf{I_{ds} = AT^2 exp\left(\frac{\Phi_B}{k_B T}\right)\left[exp\left(\frac{qV_{ds}}{k_B T}\right) - 1\right]} \tag{2.1}$$

The deviations from the linear response shown as the red and blue lines in Fig. 2.11b can be used to determine where the device threshold voltage, V_{th} and flat band voltage, V_{FB} occur correspondingly and reveal the SB height. Here, let us compare the temperature dependence at a given V_g in three regions, i.e. region A (red $V_g < V_{th}$), region B (white $V_{FB} > V_g > V_{th}$), and region C (blue $V_g > V_{FB}$), shown in Fig. 2.11a. Among them, the strongest temperature dependence occurred in region C (and blue line in Fig. 2.11b) due to the dominant thermionic current. On the other hand, region A showed the weakest temperature dependence (and red line in Fig. 2.11b) due to the tunneling current dominated transport, while region B was in between. In Fig. 2.11c, comparisons of p-type WSe_2 devices using Ni contact, Pd contact [62], exposed to O_3 treatment [30], vacuum/forming gas annealing [63] and our work clearly suggest that the direct O_2 plasma treatment significantly lowers the SB height to $\sim 70meV$ for easy hole injection. This lowering is also supported by the high-resolution transmission electron microscopy (HRTEM) which will be discussed in the following section that not only the exposed channel are converted to WO_{3-x} but also underneath

the contact. The higher work function and/or high vertical conductivity of WO_{3-x} could both/either potentially be responsible for the extracted ultra-low SB height. Although the conversion of WO_{3-x} that penetrates into the contact is only about 12nm, the transport is solely dominated near the contact edge of around 30nm and that is defined as transfer length (L_T). In principle, we would expect that the higher treatment temperature the lower Schottky barrier height it becomes. However, as we discussed in the previous section, higher treatment temperature results in degenerate doping where the thermionic part shown in Fig. 2.11a can not be resolved through electrical gating. Therefore, SB height extraction through the same method is not feasible.

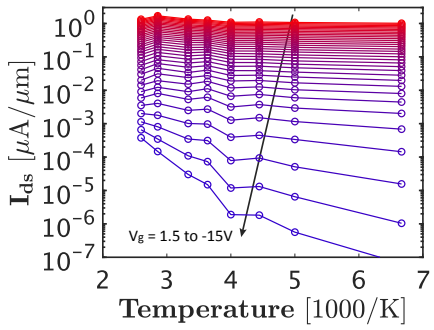

Fig. 2.9. Arrhenius plot of normalized current with respect to 1/T

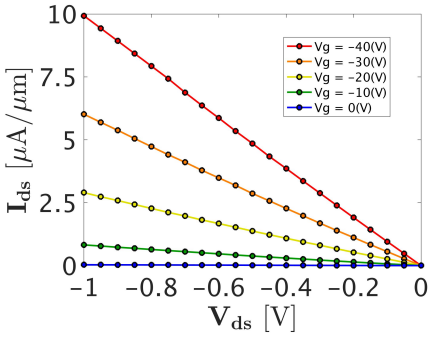

Fig. 2.10. Output characteristics of the after O_2 plasma treatment device at different back gate voltages.

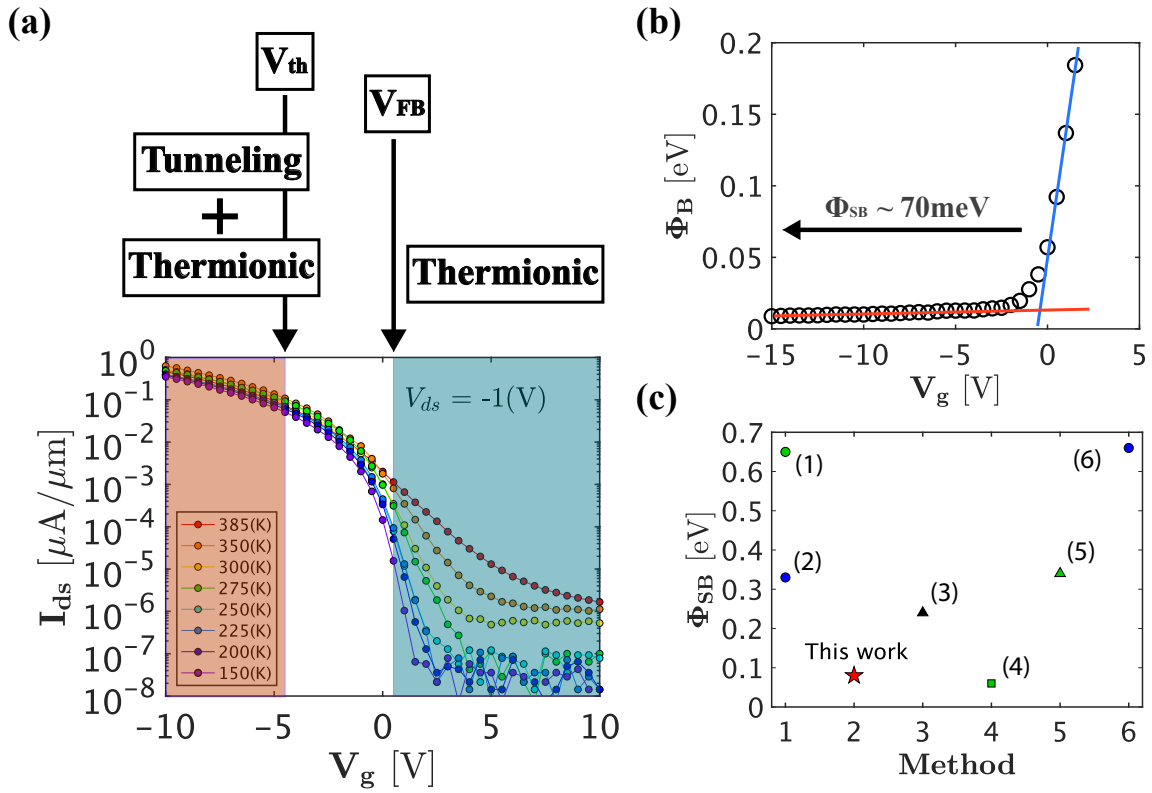

Fig. 2.11. (a) Temperature dependent transfer characteristics and the corresponding threshold voltage (V_{th}) and flat band voltage (V_{FB}). (b) Effective barrier height as a function of back gate voltage (V_g) and the extracted Schottky barrier (SB) height around 70meV. (c) Comparisons of SB height of devices using different metal contacts or different treatments. Method 1: Pd contacts (1) [63], (2) [62], method 2: direct O_2 plasma treatment with Pd contacts, method 3: O_3 exposure with Ti/Au contacts (3) [30], method 4: forming gas annealing with Pd contacts (4) [63], method 5: ultra-high vacuum annealing with Pd contacts (5) [63], and method 6: Ni contacts (6) [62]

2.4 Optical and Surface Study

Raman and XPS Analysis

To characterize the pristine CVD grown bilayer WSe_2 (before the treatment) and monolayer WSe_2 (after the treatment), Raman and XPS measurements were performed. From the Raman spectra shown in Fig. 2.12(a), the peak around 310 cm^{-1} observed in bilayer WSe_2 (left) and vanished in the WSe_2 (right) film after treatment is a clear indication that the bilayer is converted to a monolayer. XPS was measured on a monolayer WSe_2 film transferred onto a Au substrate to analyze the chemical composition before and after the treatment. In Fig. 2.12(b), upper (lower) panels show XPS scans of W, Se, and O peaks before (after) the treatment. The clearly vanishing W 4f and Se 3d peaks from WSe_2 and emerging WO_x peak in both W 4f and O 1s spectra after the treatment unambiguously proves the conversion of monolayer WSe_2 to monolayer WO_x

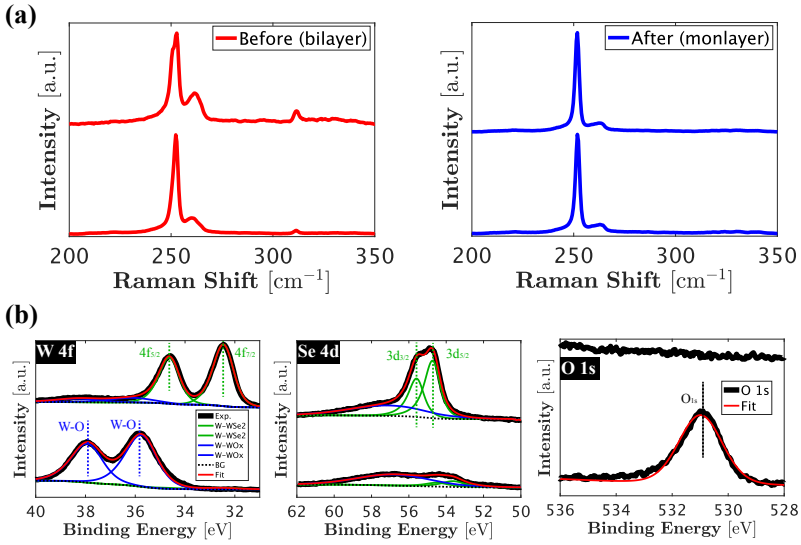

Fig. 2.12. (a) Raman spectra where before and after treatments are shown on the left and right figures respectively. Right figure shows the missing 310 cm^{-1} peak after treatment. (b) XPS spectra Upper panels show scans for pristine CVD monolayer WSe_2 and lower panels show scans after the O_2 plasma treatment.

AFM Study

AFM images and height profiles of before and after O2 plasma treatment are shown in Fig. 2.13. No roughness degradation is detected on the WO_{3-x} surface, and thus rules out the concern of AFM-detectable surface damages after the O_2 plasma treatment. Besides, no change in the height profile indicates a different bonding mechanism from the previously reported ozone treatment [30], which could possibly explain why this method shows no degradation of the doping effect even after being exposed to air for more than two weeks. Therefore, we have confirmed that both atomically precise layer control and doping level modulation can be achieved through different treatment temperatures and the surface remains atomically smooth.

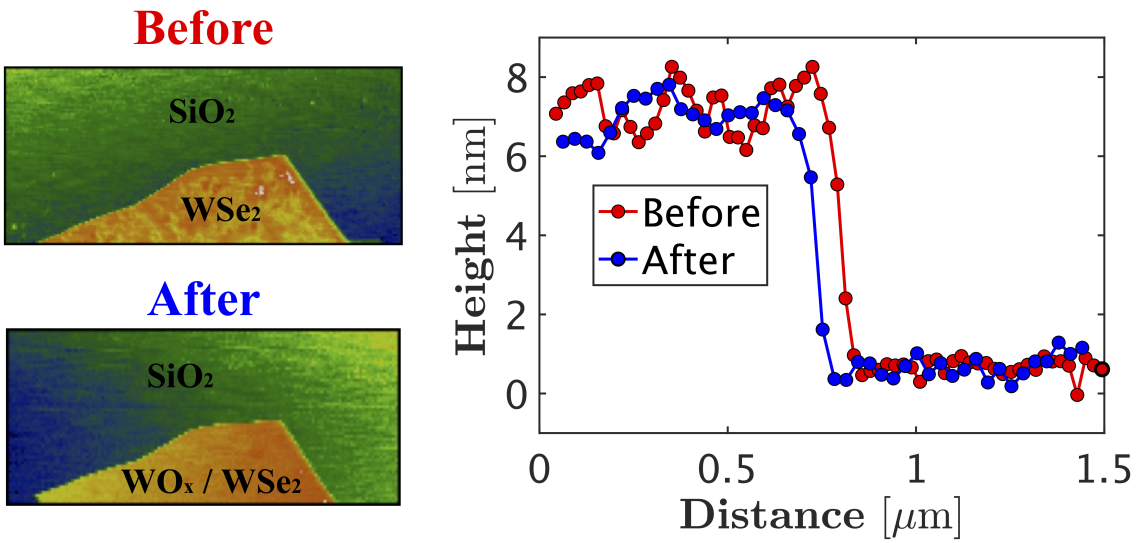

Fig. 2.13. AFM images before (upper) and after (lower) O_2 plasma and the corresponding height profiles (right). Corresponding RMS of SiO_2 and WSe_2 (before/after) are 0.5/0.7nm and 0.6/0.5nm.

3. VALLEY HALL EFFECT IN MONOLAYER MOS_2

Most of the material in this chapter has been reprinted with permission from Terry Y. T. Hung, Kerem Y. Camsari, Shengjiao Zhang, Pramey Upadhyaya and Zhihong Chen, "Direct observation of valley-coupled topological current in MoS_2" Science advances 5.4 (2019): eaau6478.

3.1 Introduction

Electronic devices exploring the carrier transport with spin and valley degree of freedom (DOF) have emerged as promising candidates for information storage and transport since pure spin and valley currents do not accompany energy dissipation associated with Joule heating. The ability to electrically generate and detect such pure spin and valley currents in these devices is of particular importance. Over the last decade, driven by the emergence of the spin-orbit coupling engineering, tremendous experimental progress has been achieved to efficiently generate spin current by charge current. On the other hand, electrical control of the valley DOF has just started to attract interest in the past few years, initiated by theoretical studies of valleytronics in two dimensional honeycomb lattice systems, such as gapped graphene and transition metal dichalcogenides (TMDs) [10, 22, 43, 45, 64, 65], revealing the interplay of their unique band structures and topologies. Experimentally, topological valley transport has been observed in graphene systems when a superlattice structure or perpendicular electric field is employed to break the inversion symmetry of this zero bandgap semiconductor [19–21]. In contrast, monolayer TMDs, such as molybdenum disulfide (MoS_2), is a direct bandgap semiconductor. Electronic transport in these materials is dominated by the inequivalent K and K valleys of the Brillouin zone located at band edges. Because of the inherent absence of inversion symmetry

in monolayer TMDs, carriers in these two valleys possess non-zero Berry curvature (Ω) without needing the assistance of external mechanisms to break the symmetry like in graphene systems. Importantly, K and K' valleys are related by time-reversal symmetry, which forces Berry curvature to flip its sign, i.e., $\Omega(K) = -\Omega(K')$ and allows for optical selection through optical pumping of valley polarization [11,12,66]. Ω acts as a pseudo-magnetic field in the momentum space and results in an anomalous transverse velocity in the presence of an electric field, i.e.

$$\mathbf{v}_{\perp} = -\frac{\mathbf{e}}{\hbar}\mathbf{E} \times \mathbf{\Omega}(\mathbf{k}) \tag{3.1}$$

Consequently, carriers from K and K' valleys develop opposite, providing a route to electrically generate pure valley currents transverse to the applied electric field. This so-called valley Hall effect (VHE) has been employed by Mak et al. [13] in monolayer MoS2 devices to measure valley polarization created by circularly polarized light and has successfully generated polarization in gated bilayer MoS2 that was then visualized by Kerr rotation microscopy [15]. It is important to note that this unique VHE phenomenon would not appear in thick multi-layer MoS_2 devices, because inversion symmetry is completely protected in samples with even layers and starts to recover in thick odd layer samples [67]. In addition, carrier transport in these indirect bandgap multi-layer samples does not involve K and K' valleys, which can result in very small or even zero Berry curvature. In our experiments, we use multi-layer MoS_2 devices as direct comparison or control samples to monolayer devices. Fig. 3.1 illustrates the VHE occurring in the left vertical electrode of a monolayer MoS_2 Hall bar device. Analogous to the spin current, such valley current comprises of carriers of opposite (valley) polarization moving along opposite directions, resulting in charge neutral valley current along x-axis. Onsager reciprocity [35] then ensures the reciprocal effect, a phenomenon defined as the inverse valley Hall effect (iVHE) that converts a non-zero valley current into a transverse electric field, and finally develops charge accumulation across the right vertical electrode of the Hall bar in Fig. 3.1. In this section, we demonstrate electrical generation and detection of valley current in monolayer MoS_2 by combining VHE and iVHE in the above-described non-

local Hall bar device geometry. We observe large non-local signals at distances more than four micrometers away from the charge current path and a unique temperature dependence that is consistent with valley transport physics.

3.2 Giant Non-local Valley Signal

A colored scanning electron microscopy (SEM) image of one of the measured MoS_2 Hall bar devices is shown in Fig. 3.1. Two types of measurements can be made, as illustrated in Fig. 3.1. A conventional four probe measurement (type II) allows the extraction of sheet resistance and contact resistance, while the non-local set up (type I) measures the Hall voltage induced by any carrier distributions due to the valley Hall effect or classical Ohmic contribution. A back gate voltage (V_g) is applied to the SiO_2/Si substrate in order to modulate the carrier concentration in the MoS_2 channel. Device fabrication is provided in the materials and methods below. Optical and electrical characterizations, and measurement details are provided in section 3.8. Typical n-type MoS2 field-effect transistor behaviors are observed in two probe measurements of all devices; sheet resistance and contact resistances are extracted from type II measurements for various temperatures ranging from 4K to 300K (see section 3.8). Field effect mobility of $10\ cm^2/Vs$ and $30\ cm^2/Vs$ are typically measured at room temperature for monolayer and multi-layer devices, respectively. The most important spurious signal to be ruled out in our measurements is the Ohmic contribution that can result in a van der Pauw like signal [68] in a typical non-local, type I measurement. When a DC bias of $V_{ds} = 5V$ is applied to the left electrode of the Hall bar, non-local Hall voltage (V_{nl}) measured in the on-state of a monolayer MoS2 device ($40V < V_g < 60V$) can reach 0.6V at T = 300K and increase to $\sim 1.2V$ at T = 4K, as compared to $\sim 10mV$ $50mV$ V_{nl} readings in the on-state of a multi-layer (9-10 layers) device ($20V < V_g < 40V$), shown in Fig. 3.3. As mentioned above, VHE does not exist in thick multi-layer MoS_2 since inversion symmetry is either preserved or weakly broken and transport does not

occur in K and K' valleys. Therefore, the detected finite V_{nl} signals in multi-layer devices can only be associated with Ohmic contribution or any other unknown effects. The magnitude of the non-local voltage due to the Ohmic contribution is expected to be dependent on the sheet resistance (ρ) of the channel and device geometry: $V_{Ohmic} = I_{DC}\ \rho_{sh}\ (W/W_1)\ e^{(-L)/W)}$ [68], where L is the channel length and W and W_1 are the width of the channel and the current electrode, respectively (labeled in Fig. 3.1).

Experimentally, we performed the same non-local measurements for multi-layer MoS_2 devices in which the channel is known to have inherent (even layer) or weakly broken (thick odd layer) inversion symmetry [67]. Furthermore, even if we ignore the fact that the inversion symmetry is largely recovered in thick odd layer samples, the magnitude of the Berry curvature varies a lot across the Brillouin zone in the momentum space. This is shown theoretically in [22] that the Berry curvature has maximum value around the K valley and is close to be zero at the Γ valley. This has a significant impact on electrical measurements since transport properties are dominated by K valleys in monolayers and the conduction band edge is between K and Γ valleys in multi-layer samples. Therefore, we believe that the presented multi-layer samples have no or negligible valley Hall contribution and the measured non-local voltage is attributed to the Ohmic contribution only. Fig. 3.4 shows qualitative agreement between the measured local V_nl in multi-layer MoS_2 devices and the Ohmic contribution Eq. 3.2

$$\mathbf{V_{Ohmic}} \ = \ \mathbf{I_{ds}}\ \rho_{\mathbf{sh}}\ \frac{\mathbf{W}}{\mathbf{W_1}}\ \mathbf{exp}\left(\frac{-\pi \mathbf{L}}{\mathbf{W}}\right) \tag{3.2}$$

Using individual I_{DC} and ρ_{sh} measured for monolayer and multi-layer MoS_2, we are able to calculate the Ohmic contribution as a function of the back gate voltage (V_g) for each device, as presented in Fig. 3.3. We notice that the magnitude of the measured V_{nl} of the multi-layer device from Fig. 3.3 matches the values of the calculated Ohmic contribution, while more than 1 order of magnitude larger V_nl signals are measured in the monolayer MoS_2 device with an opposite temperature trend that we will discuss

later. This significant magnitude difference in measured non-local voltages is also supported by a detailed potential analysis that resembles our experimental setup as shown in Fig. 3.2. Using experimentally measured contact resistance and MoS_2 sheet resistance obtained from the four-probe measurement, only a fraction of the supply voltage ($V_{ds} = 5V$) is actually applied across the injector lead, i.e. $V_{in} = 1.8V$. We then simulate in SPICE a resistor network with 4×10^6 identical resistors uniformly distributed over the Hall bar and observe that when a constant voltage of 1.8V is applied at the injector, the non-local voltage drop across the detector lead in the given geometry due to the Ohmic contribution is expected to be $\sim 29mV$. This picture can get more complicated by the gate field controlled Schottky-barrier contacts [27]. Nevertheless, we conclude that the magnitude of V_{nl} due to the Ohmic contribution calculated from the resistor network is in good agreement with the experimental measurements in multi-layer MoS_2 devices. We rule out the possibility of magnitude difference coming from the characteristic difference between monolayer and multi-layer by evaluating the impact of mobilities on non-local signals. (Section 3.8)

Last, non-local signals measured with in-plane magnetic field applied up to 5T were presented in Fig. 3.5. As expected, no impact from the magnetic field is observed, indicating the robustness of the valley polarization in monolayer MoS2 and further excluding the possibility of spin Hall effect responsible for our measurements. Therefore, these results once again resonate with the mechanism of the valley Hall effect [11, 69].

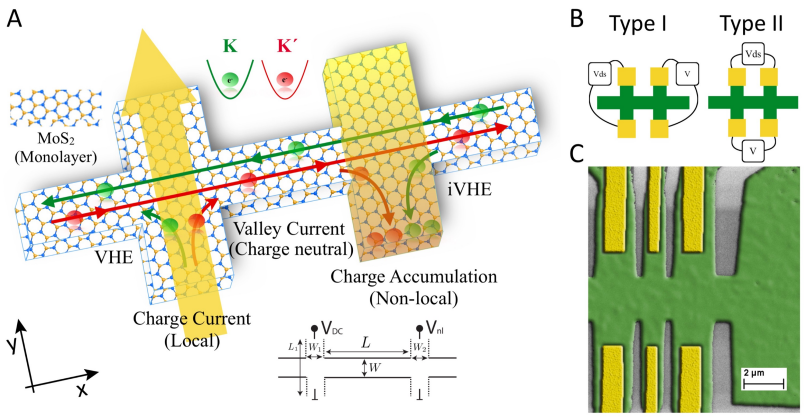

Fig. 3.1. Valley-coupled topological current. (A) Schematic of valley-coupled topological current due to VHE and iVHE in monolayer MoS2 and the device ge- ometry(bottom),where W_1=1mm, W=W_2=2mm,L_1=4.5mm,and L=0.5mm. (B) Schematics of two measurement setups: type I and type II. (C) Patterned MoS_2 flake (green) and lithographically defined metal electrodes (yellow).

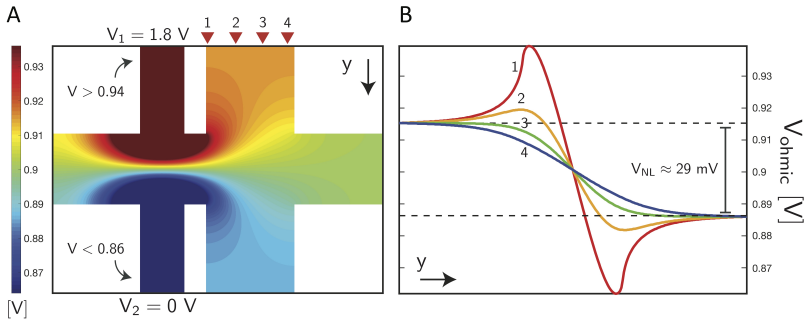

Fig. 3.2. Electric potential mapping from a SPICE-based resistor network simulation. (A) SPICE simulation of a resistor grid with $\sim 4 \times 10^6$ uniform resistors, where each resistor corresponds to 3-nm channel length, with (x = 1500, y = 1400) points. V_{ds} values applied at the two ends of the injector are V_1 = 1.8 V and V_2 = 0 V, respectively. Values greater than 0.94 V and less than 0.86 V are denoted with the same colors to resolve the nonlocal voltage distribution. (B) Voltage profiles along the y direction for four different positions denoted by arrows (1 to 4) in (A). Nonlocal voltage difference under open circuit condition is calculated to be 29 mV.

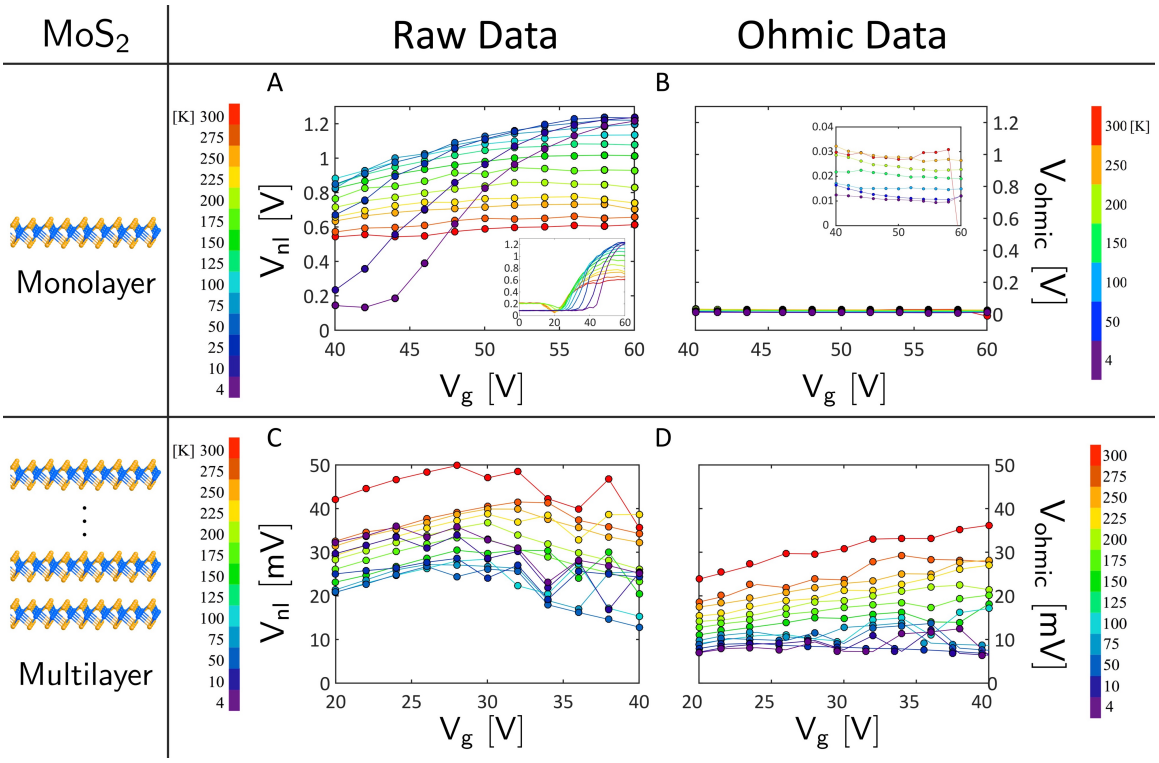

Fig. 3.3. Comparison of nonlocal voltages obtained in monolayer and multilayer MoS_2 devices. (A) Measured nonlocal voltage with respect to global back-gate voltage V_g in monolayer MoS_2 using type I setup. Inset: Full range of V_g. Note that data points in the range of V_g ¡ 40 V are not included in analysis because these large device resistances become comparable to the input impedance of the nanovoltmeter. (B) Ohmic contribution calculated from the measured sheet resistance: $V_{ohmic} = I_{DC}\rho_{sh}\frac{w}{w_1}e^{\frac{-\pi L}{w}}$ as a function of V_g, plotted with the same y-axis range as in (A). Inset: Zoom-in data. (C and D) Nonlocal voltage response in a multilayer MoS_2 device for the same measurements performed in (A) and (B). Note that the y axis in both plots has a unit of millivolts.

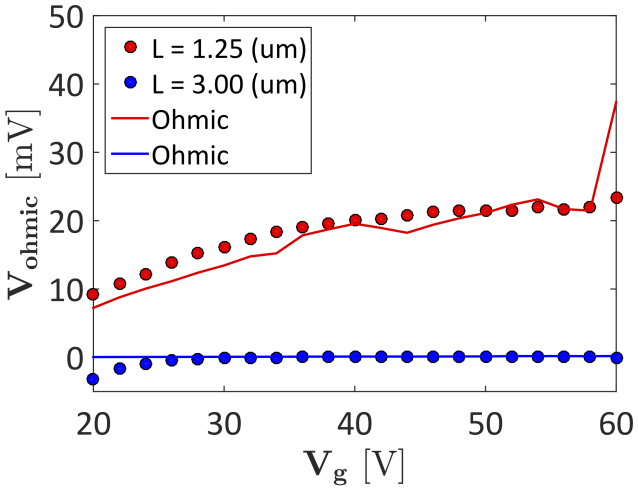

Fig. 3.4. Type I, non-local measurements were performed in additional multilayer MoS_2 devices with different channel lengths. Dotted lines are the calculated Ohmic contribution as described in the text. Close to zero non-local voltages are measured in the device with channel length of $L = 3\mu m$.

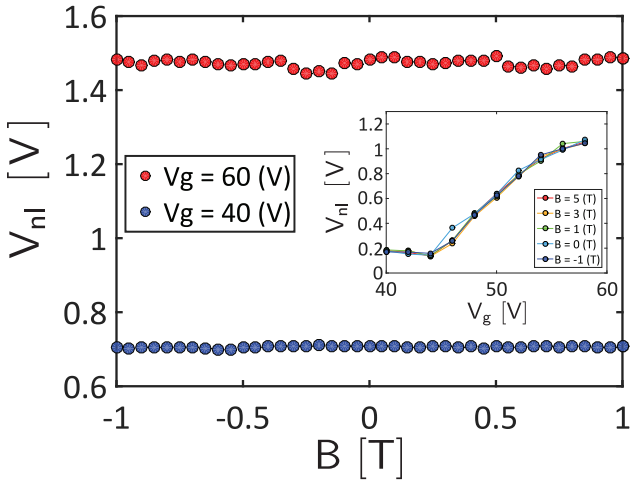

Fig. 3.5. V_{nl} measurements with in-plane magnetic field applied. Measured V_{nl} as a function of the applied in-plane magnetic field. (Inset) Non-local voltage, V_{nl} as a function of V_g under in-plane magnetic fields up to 5T.

3.3 Temperature Dependence

In addition to the magnitude of V_{nl} in the previous section, its temperature dependence provides another evidence in support of the VHE being responsible for the non-local carrier transport in monolayer MoS_2. Fig. 3.6 shows increasing V_{nl} with decreasing temperature down to 50K in monolayer MoS2, while a completely opposite trend is observed for the multi-layer in Fig. 3.6. Note that, since a voltage source, V_{ds}, is used in our measurements (instead of a constant current source), the temperature dependence of Vohmic mentioned in the previous section due to the sheet resistance (ρ_{sh}) is expected to be cancelled out. However, finite contact resistance (R_c) needs to be considered in all MoS_2 devices, which prevents ρ_{sh} to be eliminated in the evaluation of the Ohmic contribution. In fact, it is expected that $V_{Ohmic} = \frac{V_{ds}}{2R_C+\rho_{sh}\frac{L_1}{W_1}}\rho_{sh}\frac{W}{W_1}e^{\frac{-\pi L}{W}}$. Different temperature dependence of R_c and ρ_{sh} are observed in four probe measurements, presented in section 3.8. Indeed, the increasing V_{nl} with increasing temperature observed in Fig. 3.6 for the multi-layer MoS_2 device (dots) can be fitted by the modified Vohmic equation, considering the contribution from the contact resistance (lines). On the other hand, the increasing V_{nl} with decreasing temperature down to 50K for the monolayer MoS_2 device is expected for enhanced intervalley scattering length (λ) at low temperatures [14, 70, 71], confirming that valley transport is responsible for the observed large signals. More detailed analyses of non-local signals and intervalley scattering length will be discussed in the following section. Interestingly, this increasing V_{nl} with decreasing temperature trend stops at T $\sim 50K$ and reaches its maximum value. This unique maximum point results from two extreme limits of λ approaching either zero or infinity. While smaller V_{nl} is expected with increasing temperature due to a shorter λ, large λ at temperatures lower than 50K can also lead to reduced non-local resistances, $R_{nl} = V_{nl}I_{DC}$. This transition can actually be analogized to the well-studied quenched Hall effect [72, 73], where the Hall voltage vanishes when the carriers longitudinal velocity is much higher than the transverse velocity. We suggest that the

observed non-monotonic temperature dependence of V_{nl} for monolayer MoS_2 is an outcome of the monotonically increasing λ with decreasing temperature. We highlight that such temperature dependence of λ is consistent with the recent observation of increased intervalley scattering rate at higher temperatures in TMDs, which is attributed to phonon activated intervalley relaxation [74]. We will now quantitatively analyze this interesting temperature dependence of R_{nl} for monolayer MoS_2 using a self-consistent theoretical model describing the VHE. This model, similar to other theoretical descriptions in the literature [21, 68] assumes a uniform and rectangular geometry without considering the arm lengths (Fig. 3.6). Also following [21, 68], we use a circuit model that is equivalent [75, 76] to the standard spin-diffusion equation used in the context of materials with spin Hall effect to describe the VHE by defining the valley Hall angle as, $\theta = \sigma_{xy}/\sigma_{xx}$, where σ_{xx} and σ_{xy} denote longitudinal and transverse Hall conductivities, respectively. The valley Hall conductivity includes both intrinsic and extrinsic contributions and can be written as $\sigma_{xy} = \sigma_{xy}^{in} + \sigma_{xy}^{ex}$ [1]. When the Fermi-level lies close to the conduction band minima, a condition that is fulfilled by our MoS_2 devices (see section 3.5), σ_{xy}^{in} dominates over σ_{xy}^{ex} (30). Using $\sigma_{xy}^{in} \sim (2e^2)/h$ [19] and measured σ_{xx}, we estimate $\theta \sim 0.4$ at T = 50K for our devices which is similar to Gorbachev et al.s estimation [19](see section 3.5 for a detailed calculation of θ as a function of temperature). As also noted in [21], when θ is not small (i.e. $\theta \sim 1$), one needs to self-consistently solve R_{nl} considering the feedback impact of iVHE that behaves as a load to the generating section (induced by the direct VHE), and the impact of VHE that serves as a load to the detecting section (governed by the iVHE). Our circuit model automatically captures such self-consistencies to arbitrary order when solved in SPICE, but it is possible to derive an analytical equation considering only the iVHE at the generator side and the VHE at the detector side as second order effects. Further, our model takes the width of the arms explicitly and we can analytically obtain the following expression for the non-local resistance :

$$\mathbf{R_{nl}} \equiv \frac{\mathbf{V_{nl}}}{\mathbf{I_{DC}}} = \frac{2\rho\lambda W exp[-\frac{L}{\lambda}]\ sinh[\frac{W_1}{2\lambda}]\ sinh[\frac{W_2}{2\lambda}]\ \theta^2}{(exp[\frac{W_1}{2\lambda}]\ W_1 + 2\lambda\ sinh[\frac{W_1}{2\lambda}]\ \theta^2)(exp[\frac{W_2}{2\lambda}]\ W_2 + 2\lambda\ sinh[\frac{W_2}{2\lambda}]\ \theta^2)} \quad (3.3)$$

where λ is the intervalley scattering length, $W_{1,2}$ are the widths of the generating and detecting arm respectively, ρ_{sh} is the sheet resistance and W is the width of the channel in Fig. 4C. We combine our VHE model [76] with non-magnetic circuit models that are also derived from a valley-diffusion equation (without any spin-orbit coupling) to obtain the infinite valley-loads on both ends, as well as to obtain the valley-diffusion in the middle channel whose length is denoted by L, based on the spin-circuit modeling described in [75]. Conversely, the VHE model only considers charge transport in the vertical direction and valley coupled topological current in the longitudinal direction. It is important to note that, Eq. 3.11 is validated by a self-consistent numerical simulation of the composite valley-circuit in SPICE simulations and can be analytically reduced to the expression generally used in the literature [68], if we assume $\theta^2 << 1$ and $W_{1,2}/\lambda << 1$, yielding: $R_{nl} = \frac{1}{2}(\theta^2 \frac{W}{\sigma\lambda})exp(\frac{-L}{\lambda})$. It is clear from the complete Eq. 3.11) and reduced equation that the two extreme limits of λ naturally lead to an optimal intervalley scattering length to reach the maximum non-local resistance value. This unique behavior enables us to quantitatively extract λ. Suggested by Eq. 3.11, the temperature dependence of R_{nl} comes from that of λ and θ. With the calculated $\theta(T)$ shown in the inset of Fig. 3.6D we are able to fit the normalized non-local resistance, R_{nl}^{norm}curve (dashed blue line in Fig. 3.6D, labeled as Empirical) by tuning $\lambda(T)$. Since different physical mechanisms are responsible for the decreasing R_{nl}^{norm} in the low and high temperature regimes, we can separately fit the high temperature trend with a power law function of $\lambda \propto T^{-0.73}$, which is in line with the temperature dependence of intervalley scattering that will be discussed later. Fitting for $T > 75K$ regime is shown as the solid green line in Fig. 3.6D. $\lambda(T)$ is then quantitatively extracted from R_{nl}^{norm} and plotted (blue dots) in Fig. 3.6E, in a good agreement with the power law fitting at high temperatures. Furthermore, using the analytical expression in [77] describing both acoustic and optical intervalley phonon scattering together with the field effect mobility extracted from type II measurements, we are able to analytically derive $\lambda(T)$ as shown as the solid line in the inset of

Fig. 3.6E (see section 3.5 and 3.8). A power law fitting of $\lambda \propto T^{-0.6}$ (dashed line) is obtained here, which is consistent with the experimental fitting of $\lambda \propto T^{-0.73}$ at $T > 100K$. At low temperatures, the extraction of $\lambda > 1\mu m$ from the experimentally measured non-local signals is comparable to other valley Hall systems, as reported in [19–21]. In addition to this unique λ extraction through fitting the temperature dependence plot, three distinguished long channel devices were fabricated on the same monolayer MoS_2 flake to allow λ extraction through the channel length dependence and more details will be provided in the following section. In general, λ is believed to be governed at low temperatures by atom-like defects that provide the necessary momentum required for carriers to scatter between K and K' valleys in the conduction band. In MoS_2, these atom-like defects arise due to molybdenum and sulfur vacancies. Recently, it has been pointed out that owing to the symmetry of atomic defects, only molybdenum vacancies can participate in intervalley scattering [78]. Fourier transform scanning tunneling spectroscopy studies also provide further evidences [79, 80]. The relatively large λ on the micron-scale extracted from our devices could be a result of relatively low molybdenum vacancy density in our MoS_2 sample.

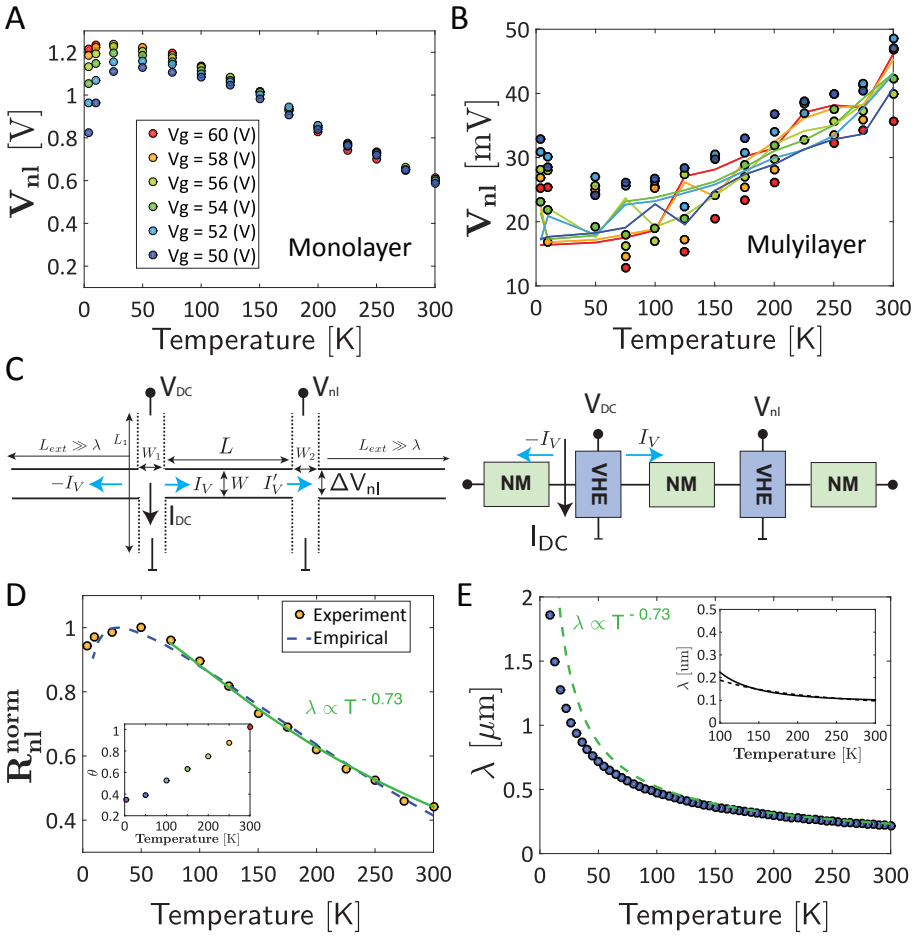

Fig. 3.6. Temperature dependence and extraction of intervalley scattering length. (A) Measured V_{nl} as a function of temperature at different V_g for monolayer MoS_2. (B) Temperature dependence of multilayer MoS_2 at different V_g (dots) and the calculated trends (lines) using the modified ohmic equation, $V_{ohmic} = \frac{V_{ds}}{2R_c+\rho_{sh}\frac{L_1}{w_1}}\rho_{sh}\frac{w}{w_1}e^{\frac{-\pi L}{w}}$, with the consideration of the contact resistance contribution (see section 3.8). Note that the trends of V_{nl} with respect to temperature in (A) and (B) are completely opposite. (C) Device geometry and corresponding valley-circuit model that define the geometric parameters in Eq. 3.11. Details are given in section 3.6. (D) Temperature dependence of R_{nl}^{norm}(normalized to the maximum point) measured at $V_g = 58$ V [orange dots in (A)]. The empirical fittings use $\lambda(T) = 5.5T^{-0.47} - 0.16$ (dashed blue line) and $\lambda(T) = 15T^{-0.73}$ at T > 100 K (green line). Inset: Calculated temperature dependence of valley Hall angle,Θ.(E) $\lambda(T)$ extracted from R_{nl} and the power-law dependence described in (D). Inset: Theoretically calculated intervalley scattering length (solid line) and $\lambda \propto T^{-0.6}$ to guide the eye (dashed line).

3.4 Geometry Dependence in Monolayer MoS_2 Devices

We fabricated another batch of devices with three distinguished channel lengths, $L = 2,\ 4,\ 5.5\mu m$ on the same monolayer MoS_2 flake for direct comparison, while the channel width (W), electrode widths (W_1 and W_2), and electrode length (L_1) are all fixed at 2um (see Fig. 3.3A inset in the main text for respective labeling). Non-local signals larger than $\sim 450mV$ were observed at room temperature for the device with $L = 2\mu m$ and 120mV for $L = 4\mu m$, and finally diminish when the channel is $5.5\mu m$ long. $\lambda \sim 600nm$ is extracted for valley transport at room temperature, which is consistent with the temperature fitting method within a reasonable range considering sample to sample variations. In contrast, non-local voltages of $\sim 20 - 30mV$ were measured for multi-layer devices shown in Fig. 3.3C and Fig. 3.4 with $L = 0.5\mu m$ and $1.25\mu m$. The signals become too small to be measured when $L > 3\mu m$ for multi-layer devices. These large magnitude differences between monolayer and multi-layer devices are consistent with what we presented in the main text. Furthermore, exponential channel length dependence is observed in the monolayer devices fabricated on the same MoS_2 flake. To eliminate any artifacts originated from using different charge current paths, we divided V_{nl} by I_{DC} correspondingly. In Fig. 3.7, semi-log R_{nl} vs. L is plotted and intervalley scattering length $\lambda \sim 600nm$ is extracted through the slope fitting. This is of the same order of magnitude as what we extracted from the temperature dependent measurements yielding $\lambda \sim 250nm$. We attribute the difference to fabrication variations and MoS_2 flake differences. Channel width dependence (W) comparison was not able to be made on the same flake for quantitative analysis. Based on Eq. 3.11 or its reduced format Eq. 3.14, W appears as a pre-factor in the non-local signal equation. When the devices have similar channel length (L), but different channel width ($W = 1\mu m$ and $2\mu m$), large non-local signals were observed in the wider device ($\sim 230\ k\Omega$) compared to the narrow device ($\sim 40\ k\Omega$). The width ratio is not exactly reflected as the pre-factor, primarily due to the flake differences and fabrication variations.

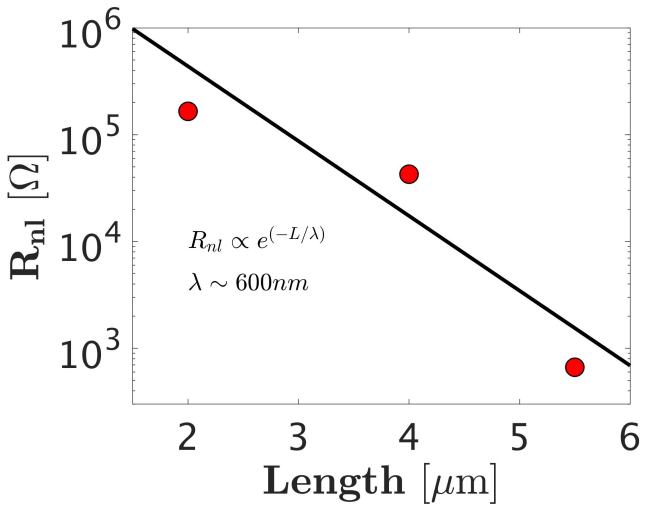

Fig. 3.7. Non-local resistance R_{nl} as a function of channel lengths at $V_g = 40V$.

3.5 Detailed θ and λ Calculation and Their Temperature Trends

In the previous section, we define θ in Eq. 3.4. In order to estimate θ, we calculate σ_{xy} due to intrinsic (Berry phase) contribution to the valley Hall conductivity, σ_{xy}^{in}, while directly extracting σ_{xx} from type II measurements shown in Fig. S2C. It should be noted that in doing so, we have ignored possible impurity scattering-induced extrinsic contributions (1, 41) to the valley Hall effect. As pointed out in [10, 81], this approximation is justified for the case when Fermi-level (E_F) lies close to the conduction band edge. This is indeed the case for the voltage range explored in our measurements. In particular, $E(k) = \pm\sqrt{\Delta^2 + v^2\hbar^2k^2}$, for $V_g - V_{th} = 40\ V$, the position of the Fermi-level (as measured from the middle of the band gap) is given by Eq. 3.5. Here, $2\Delta \sim 1.72eV$ is the band gap for MoS_2, $\hbar$ is the Plank constant divided by 2π, $m_e^* = 0.4m_e$ is the electron effective mass in MoS_2, and $n \sim (V_g - V_th)\epsilon_r\epsilon_0/t_{SiO_2}\ e$ is the surface charge accumulated by the gate, with $V_g - V_{th}$ being the overdrive volt-

age, $\epsilon_r\epsilon_0$ as the permittivity in SiO_2, and $t_{SiO_2} = 90\ nm$ as the dielectric thickness. The intrinsic valley Hall conductivity is given by Eq. 3.6 [81]

$$\theta = \frac{\sigma_{\mathbf{xy}}}{\sigma_{\mathbf{xx}}} \tag{3.4}$$

$$\mathbf{E_F} \sim \frac{\mathbf{n\pi\hbar^2}}{\mathbf{2m_e^*}} + \mathbf{\Delta} \sim \mathbf{0.89eV} \tag{3.5}$$

$$\sigma_{\mathbf{xy}}(\mathbf{E_F}) = \mathbf{\Sigma}_{\tau_\mathbf{Z}}\tau_\mathbf{Z}\ \Sigma_{S_Z,\alpha}\frac{e^2}{\hbar}\frac{1}{(2\pi)^2}\int dk_x dk_y \Omega(k,\tau_Z,\alpha) f(E_{k,\alpha}) \tag{3.6}$$

$$\mathbf{\Omega} = \tau_\mathbf{Z}\frac{\mathbf{\Delta^2 v^2\hbar^2}}{\mathbf{2(\Delta^2 + v^2\hbar^2k^2)^{3/2}}}$$

where E_F is the Fermi-level, τ_z is the valley index ($\tau_z = -1$ for K and $\tau_z = +1$ for K), α is the band index ($\alpha = -1$ for the valance band and $\alpha = +1$ for the conduction band), s_z is the spin index ($s_z = -1$ for up spin and $s_z = +1$ for down spin), and $v^2 = \Delta/m_e^*$ [10, 21, 81]. Here, putting $E_F \sim 0.89\ eV$ we find $\sigma_{xy} \sim \frac{2e^2}{h}$. This value is consistent with the fact that for the Fermi-level position close to conduction band minima, the valley Hall conductance is dominated by the filled valence bands. Substituting this value in the definition of θ and using σ_{xx} from Fig. 3.13C, we plot θ v.s. temperature in the inset in Fig. 3.6D. In general, increasing the temperature decreases σ_{xy}. This is because conduction and valence band contribute opposite signs to σ_{xy}, and increasing temperature increases conduction band occupation at the expense of the valence bands population. However, we highlight that for the Fermi-level position near the conduction band minima, and the band gap of 1.72 $eV >> k_BT$ for T = 300K, the value of σ_{xy} is independent of temperature (as verified by directly calculating σ_{xy} for T = 1 K and T = 300 K using Eq. 3.6 and noting a decrease of less than 0.4%). In this case, the temperature dependence of θ comes primarily from the temperature dependence of σ_{xx} in Fig. 3.13C. In Fig. 3.8, we plot this temperature dependence of θ, which is also presented in the inset of Fig. 3.6D in the main text.

Now, let us take a look at the dependency of λ and temperature. Within the deformation potential approximation, the analytical expression of intervalley scattering rate τ, as obtained from Fermis golden rule, is given by Eq. 3.7 [77],

$$\frac{\mathbf{1}}{\tau} \;=\; \mathbf{g_d}\;\frac{\mathbf{m^* D_o^2}}{\mathbf{2\hbar^2}\rho\omega}\;[\mathbf{N\Delta_1} + \;(\mathbf{N}\;+\;\mathbf{1})\mathbf{\Delta_2}] \tag{3.7}$$

Here g_d is the valley degeneracy for the final electron states, m^* is density-of-state effective mass for the K valley, D_0 is the deformation potentials in K valley (D_0^{op},D_0^{ac} are for optical and acoustic phonon respectively), ρ is the mass density ($= 3.1 \times 10^{-7} g/cm^2$) for MoS_2, $\hbar\omega$ is phonon energy, N is Bose-Einstein distribution and Δ_1, Δ_2 are the onset of scattering for phonon absorption and emission respectively. Using Eq. 3.7, $\lambda = \sqrt{D_{diff}\tau}$), Einstein relation for diffusion coefficient ($D_{diff} = \mu k_B T/q$), and experimentally extracted field effect mobility (μ), we calculate intervalley scattering length (λ) in high temperature regime ($T > 100\ K$) shown in Fig. 3.8. The calculated λ(T) (solid line) can be fitted with a power law dependence of $\lambda \;\propto T^{-0.6}$ (dashed line).

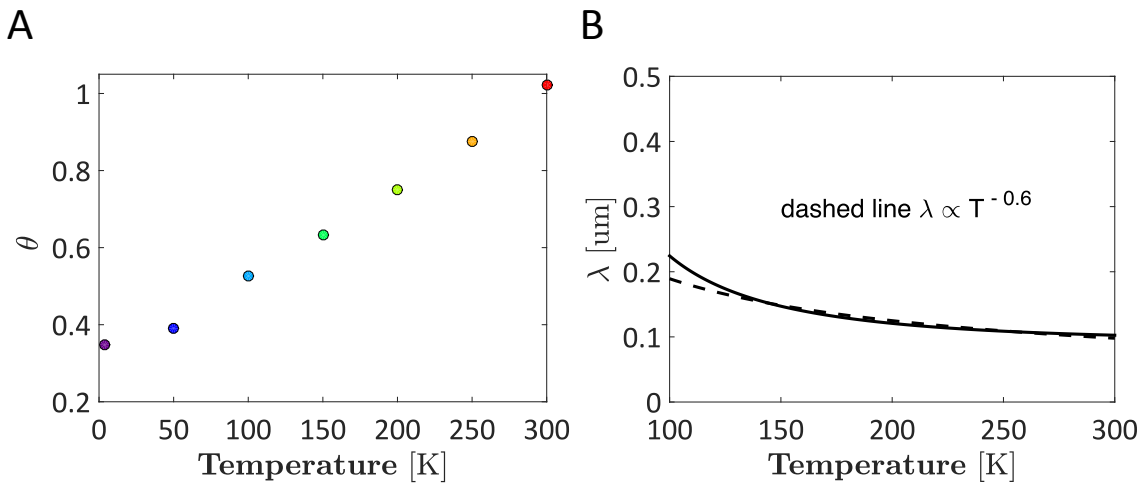

Fig. 3.8. (A) Temperature dependence of valley Hall angle. (B) Temperature dependence of intervalley scattering length.

3.6 Derivation of Non-local Resistance

In this section, we outline the derivation details of Eq. 3.11, starting from a lumped valley-circuit model whose results are equivalent to those of the commonly used spin-diffusion equations [82]. We then compare the analytical expression with a fully self-consistent SPICE-based numerical solution of the circuit. Fig. 3.9 shows the circuit diagram that is based on [75]. The lumped model combines non- magnetic (NM) regions that act as boundary conditions that are much longer than the diffusion length (λ) with two VHE layers that are bridged by another NM region that the valley polarized carriers diffuse over. We neglect the VHE physics in this middle layer but explicitly consider the spin-diffusion and loss. The VHE layers are composed of a charge-circuit and a valley-circuit that treat the charge and spin flows differently, as in [76]. The model takes into account both the direct VHE and the inverse VHE with dependent current sources in the valley-circuit I_1, I_2 and in the charge circuit I_3, I_4, respectively. Therefore, the model captures effects such as self-induced inverse VHE due to a charge current flowing in the injection layer and a self-induced direct VHE in the detection layer due to an induced open-circuit voltage. We define σ as the sheet conductivity of the material ($\sigma = \sigma_{xx}t$) where σxx is the longitudinal conductivity and t is the thickness of the sample. The charge and valley conductance are defined in Fig. 3.9. We assume that a constant charge current I_{DC} is being injected between nodes V_{1c} and V_{2c} and this gives rise to an open-circuit, non-local voltage ΔV_{NL} between nodes V_{5c} and V_{6c}. We are then interested in a closed-form expression relating these two quantities, $R_{nl} \equiv \Delta V_{NL}/I_{DC}$. We consider three terms contributing to this expression: i_1: Self-generated VHE current (opposing) due to an injected current I_{DC}. i_{2R}: Direct VHE current due to an injected I_{DC}. i_{2L}: Direct VHE current (opposing) due to an induced ΔV_{NL}. We ignore the higher order terms assuming they get progressively smaller since $\theta < 1$, and later show (Fig. 3.10) that the results are in good agreement with a full SPICE-based solution of the circuit without any assumptions. We start with the derivation of the current i_1 which increases the ef-

fective resistance of the injecting layer, similar to the Spin Hall Magnetoresistance effect. With a straightforward solution of the circuit we find:

$$\mathbf{i_1} \;=\; \frac{\mathbf{2V_{DC}}\sigma\theta}{\mathbf{1+\exp[W_1}/\lambda]} \tag{3.8}$$

Using this current term, we can specify the induced charge voltage (due to inverse VHE through the current source I_3) and solve for the modified V_{DC} that develops under a constant injected current I_{DC}:

$$\mathbf{V_{DC}} \;=\; \frac{\mathbf{I_{DC}W}}{\sigma\Big(\mathbf{W_1} \;+\; \theta^{\mathbf{2}} \;\lambda\; \Big(\mathbf{1-\exp(-W_1}/\lambda)\Big)\Big)} \tag{3.9}$$

which, in the limit $\lambda << W_1$ reduces to, $R = V_{DC}/I_{DC} = W/W_1\sigma(1+\theta^2)$, implying that the resistance of the injector arm increased by a factor proportional to 2 due to the self-induced inverse VHE. We then use Eq. 3.9 to derive the term i_{2R}.

$$\mathbf{i_{2R}} \;=\; \theta\;\sigma\;\mathbf{V_{DC}}\;\frac{\mathbf{exp}\Big[-(\mathbf{W_1} \;+\; \mathbf{L})/\lambda\Big]\Big[\mathbf{exp(W_1}/\lambda)-\mathbf{1}\Big]}{\mathbf{exp}\Big(\mathbf{W_2}/\lambda\Big)+\mathbf{1}} \tag{3.10}$$

Similarly, we obtain the current i_2L by keeping ΔV_{NL} as a variable and combine it with eq. 3.10 to self-consistently solve for a ΔV_{NL} in terms of I_{DC}. With full simplifications, we obtain the following expression:

$$\mathbf{R_{nl}} \;=\; \frac{\mathbf{2}\rho\lambda\mathbf{W exp}[-\frac{\mathbf{L}}{\lambda}]\;\mathbf{sinh}[\frac{\mathbf{W_1}}{\mathbf{2}\lambda}]\;\mathbf{sinh}[\frac{\mathbf{W_2}}{\mathbf{2}\lambda}]\;\theta^{\mathbf{2}}}{(\mathbf{exp}[\frac{\mathbf{W_1}}{\mathbf{2}\lambda}]\;\mathbf{W_1}+\mathbf{2}\lambda\;\mathbf{sinh}[\frac{\mathbf{W_1}}{\mathbf{2}\lambda}]\;\theta^{\mathbf{2}})(\mathbf{exp}[\frac{\mathbf{W_2}}{\mathbf{2}\lambda}]\;\mathbf{W_2}+\mathbf{2}\lambda\;\mathbf{sinh}[\frac{\mathbf{W_2}}{\mathbf{2}\lambda}]\;\theta^{\mathbf{2}})} \tag{3.11}$$

We note that this expression reduces to the well-known non-local resistance formula under the following limits, $\theta^2 << 1$ and $W_{1,2}/\lambda << 1$, yielding:

$$\mathbf{R_{nl}} = \frac{\mathbf{1}}{\mathbf{2}}\;\theta^{\mathbf{2}}\;\rho\;\frac{\mathbf{W}}{\lambda}\;\mathbf{exp}\Big(\frac{-\mathbf{L}}{\lambda}\Big) \tag{3.12}$$

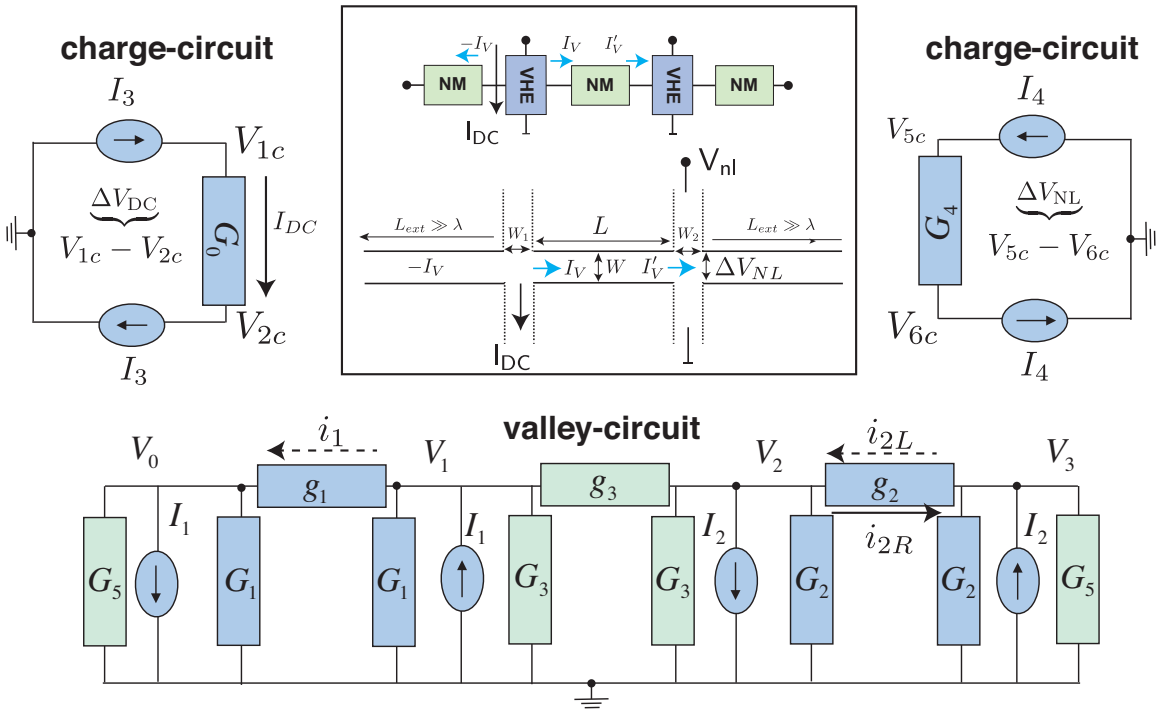

Fig. 3.9. The lumped valley-circuit model that is used to derive Eq. 3.11 in the text. The charge-circuit captures the injected and induced charge currents and voltages in the vertical direction, while the valley-circuit captures the valley diffusion currents in the horizontal direction. The charge-circuit parameters are defined as: $G_0 = \sigma W_1/W$, $G_4 = \sigma W_2/W$, $I_3 = \sigma\theta(V_1 - V_0)$ and $I_4 = \sigma\theta(V_2 - V_3)$ where θ is the valley Hall angle, σ is the sheet conductivity, and W_1, W_2, W are the width of the injector, detector and the middle region, as shown in the figure. $(V_1 - V_0)$ and $(V_2 - V_3)$ are the non-equilibrium valley potentials that control the inverse valley Hall terms in the charge circuit. The valley-circuit parameters are defined as: $g_i = \sigma W/\lambda csch(W_i/\lambda)$, $G_i = \sigma W/\lambda tanh(W_i/(2\lambda))$, where $i \in 1, 2, 3$ with $W_3 = L$ and $G_5 = \sigma W/\lambda$. Finally, the current sources $I_1 = \theta\sigma V_{DC}$ and $I_2 = \theta\sigma V_{nl}$ where V_{DC} is the applied voltage and ΔV_{NL} is the induced non-local voltage as defined in the figure. See text for the description of the current terms i_{2R}, i_{2L} and i_1 that are used in the derivation.

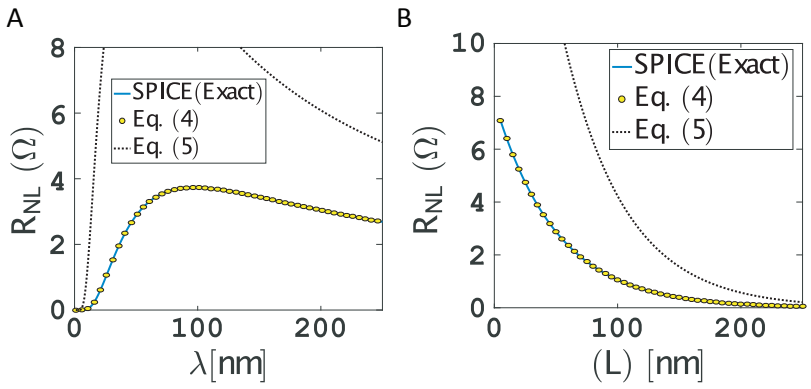

Fig. 3.10. Comparison of analytical equations for R_{nl} with the full SPICE simulation of the circuit shown in Fig. 3.10. Excellent agreement is observed between SPICE and Eq. 3.11, while deviations are clearly shown for the reduced Eq. 3.14. The parameters are $\theta = 0.5$, $\sigma = 2mS$, $W_1 = 50nm$, $W_2 = 75nm$, $W = 25nm$, $L = 50nm$ for (A) and $\lambda = 50nm$ for (B). It is interesting to note that the expression based on Eq. 3.14 overestimates the magnitude of the signal and for large θ and a self-consistent model as described here.

3.7 Non-local Internal Resistance

We add external resistors into the measurement set-up to extract the internal resistance ($R_{MoS_2} = 2R_c + 2R_{arm} + R_{cross}$) in the non-local arm in both monolayer and multi-layer MoS_2 devices, as depicted in Fig. 3.11A. The measured voltage drop across the external resistor (R_{ext}), can be described by $V_{ext} = I_{ext}(R_{ext}R_{MoS_2})/(R_{ext} + R_{MoS_2})$. Simpler expression can be derived by normalizing to its maximum point:

$$\mathbf{V_{norm}} = \frac{\mathbf{R_{ext}}}{\mathbf{R_{ext} + R_{MoS_2}}} \tag{3.13}$$

By changing over a large range (10^2 to 10^8 Ω) of external resistance values (R_{ext}) depicted in Fig. 3.11A and fitting with Eq. 3.13, we are able to extract the internal resistance. We notice that $V_{nl} \neq \Delta V_{nl}$, since ΔV_{nl} should be a fraction of V_{nl}, denoted in Fig. 3.6C in the main text. Intuitively, one might think that the ratio of ΔV_{nl} to V_{nl} should be equal to the ratio of R_{cross} to R_{MoS_2} (non-local total resistance)

shown in the Fig. 3.11A. However the extracted internal resistance ($24M\Omega$) by fitting presented in Fig. 3.11B does not agree with the non-local total resistance ($7M\Omega$) in monolayer MoS_2. In contrast, the extracted internal resistance ($25k\Omega$) presented in Fig. 3.11C is very close to the non-local total resistance ($35k\Omega$) in multi-layer MoS_2. Furthermore, we use SPICE resistor network discussed in section 3.6 to simulate this internal resistance extraction for multi-layer MoS2 with two vastly different resistor values of 10^3 (red) and 10^6 (blue) shown in Fig. 3.11D. As expected, it shows very good agreement between the extracted internal resistance and the non-local total resistance. Thus we speculate that for VHE governed monolayer MoS2 devices, it is not sufficient to take the resistance ratio (R_{cross} to R_{MoS_2}) for the internal resistance calculation. Instead, one should carefully take into account some resistance amplification due to the VHE over the entire electrode lead. Both Eq. 3.11 and SPICE capture the physics of the $(L \times W)$ rectangle shown in Fig. 3.6C without considering the extended arm. Further experiments, such as varying the arm length, directly measuring R_{cross} and independently controlling the contact and channel resistance, are required to understand the discrepancy of internal resistances between the valley Hall and non-valley Hall systems.

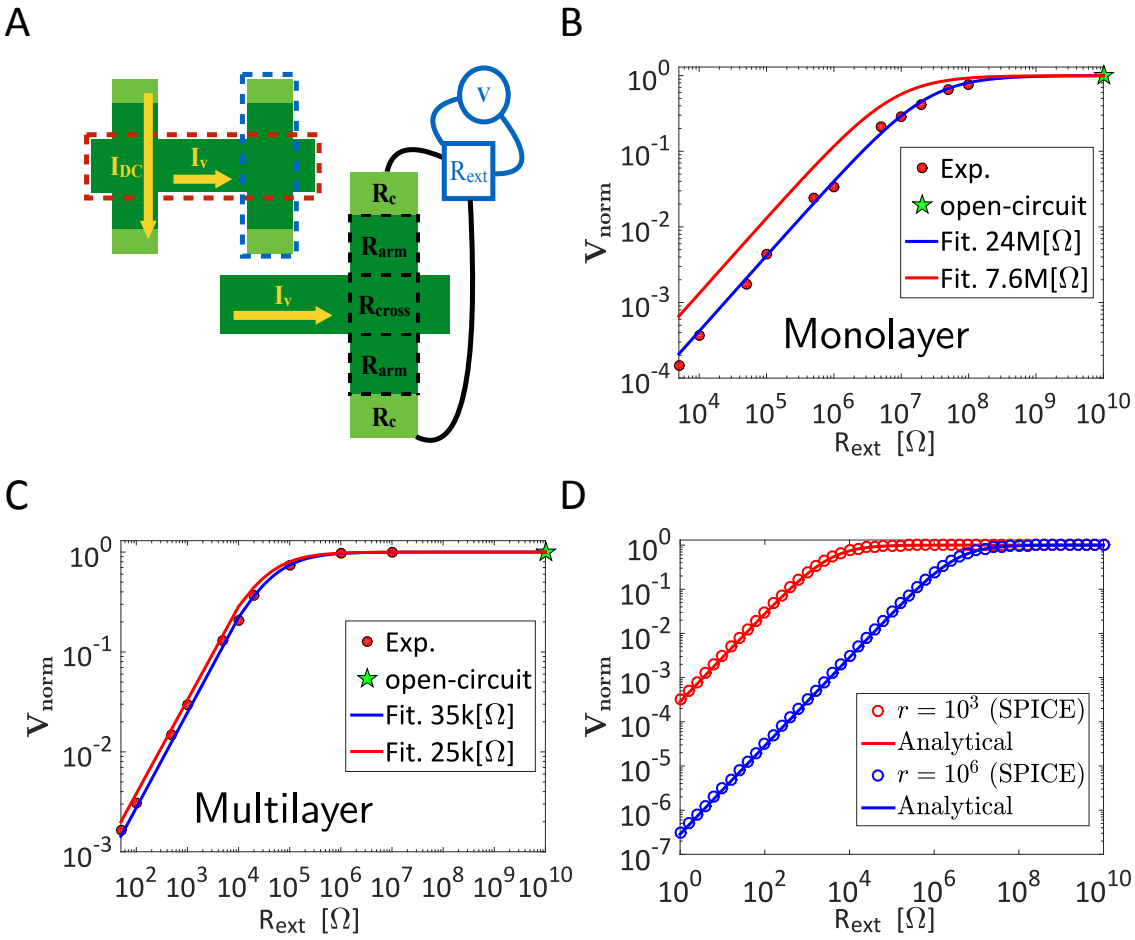

Fig. 3.11. Extraction of internal resistance in the non-local electrode. (A) Schematic of the measurement set-up with an external resistor. (B) Monolayer, (C) multilayer internal resistance (R_{MoS_2}) extraction and comparison between total resistance (R_{tot}) and internal resistance (R_{MoS_2}). (D) SPICE modeling in a uniform resistor Hall structure shown in Fig. 3.2.

3.8 Device Characterization and Methods

CVD grown MoS2 films were transferred to 90nm SiO_2 substrates with highly doped Si on the back side serving as a global back gate (V_g). The transfer process includes: 1) the sample was spin-coated with Polystyrene (PS) followed by immersing in DI water; 2) the PS/MoS_2 stack was then detached from the substrate and scooped up by the receiving SiO_2 substrate; 3) PS was subsequently dissolved by toluene and bathed in acetone and isopropyl alcohol (IPA) to thoroughly clean it. Standard e-beam lithography using PMMA A4 950 resist was employed to pattern electric contacts on the CVD MoS_2 flakes. Ti/Au (20/80nm) was deposited in an e-beam evaporator followed by a lift-off process in acetone. CVD grown BN film was transferred from Cu foil onto the devices through a process that involves etching the Cu foil with iron chloride ($FeCl_3$) and immersing it in diluted HCl and DI water alternatingly for few times before scooping up. This BN layer was inserted to minimize device degradation from PMMA residues after the RIE etching process. RIE etching mask was defined by e-beam lithography using PMMA A4 950 resist and BN/MoS_2 flakes were etched using Ar/SF_6 for 10 seconds. The final devices were annealed in forming gas (N_2/H_2) at 300C for three hours followed by vacuum annealing ($\sim 10^8$ torr) at 250^oC for 4 hours to minimize PMMA residue and threshold voltage shift due to trap charges.

Raman spectroscopy, Photoluminescence (PL) spectroscopy, Atomic Force Microscopy (AFM), and contrast in optical images were used to confirm the thickness of the MoS_2 flakes in both of the VHE device (monolayer) and the control sample (multilayer) shown in Fig. 3.12(A-D). Raman spectra were obtained using an excitation wavelength of 532nm with a 50X objective lens. A Raman shift of $18cm^{-1}$ between the E^1_{2g} and A_{1g} modes in the monolayer is clearly different from that in the multilayer, as shown in Fig. 3.12A [83–85]. PL shows the direct band gap peak at 1.83eV for monolayer MoS2. Red shift and much smaller intensity was observed in multi-layer MoS_2 shown in Fig. 3.12C. Thickness of 1nm and 7nm was measured for the mono-

layer and multi-layer MoS_2 flakes used in the device fabrication, respectively, shown in Fig. 3.12D. The reason why we measured 1nm in our monolayer sample instead of the expected 0.7nm thickness for an atomic layer is due to the air gap ($\sim 0.3nm$) between the MoS2 flake (a layered material) and the SiO_2 substrate (a non-layered material), which has been widely observed in literatures. Therefore, the measured AFM thickness should be roughly equal to $0.7nm \times numberoflayers + 0.3nm$. Due to the measurement limitation of the current meter used in our experiments, the lowest current that can be measured was $\sim 10^{-10}A$ (Fig. 3.13A, B), In MoS_2 devices, subthreshold current above $10^{-10}A$ is dominated by tunneling current injected through the source/drain Schottky barriers, which shows weak temperature dependence. The observed threshold voltage shift is as expected since a larger gate voltage is required to compensate fewer carriers in the Fermi distribution at a lower temperature. Shown in Fig. 3.13(C, D), conventional four-probe measurements (type II) were used to extract sheet resistance (ρ) and contact resistance (R_c) for monolayer and multi-layer devices, respectively [27, 86]. Filed-effect mobilities for both monolayer and multi-layer devices were extracted as a function of temperature, shown in Fig. 3.13(E, F). Less power law temperature dependence in monolayer compared to literatures comes from the contact resistance variations in different devices. Nevertheless, it is clear that mobility difference between monolayer and multi-layer is only around factor of 2-3, which will not be able to explain the more than one order of magnitude difference in the non-local signals. Second, we know that the valley coupled topological current can be described by the diffusion model. Based on Eq. 3.11 or the reduced equation Eq. 3.14

$$\mathbf{R_{nl}} = \frac{\mathbf{1}}{\mathbf{2}}\,\theta^{\mathbf{2}}\,\rho\,\frac{\mathbf{W}}{\lambda}\,\mathbf{exp}\left(\frac{-\mathbf{L}}{\lambda}\right) \tag{3.14}$$

it is expected that higher mobility (longer diffusion length λ) in the exponential term would result in larger non-local signals, which is what we observed in the temperature dependent study the non-local signal increases with decreasing temperature for monolayer MoS_2. In contrast, our study shows that the VHE device (monolayer

MoS_2) has lower mobilities while delivering much larger non-local signals compared to multi-layer MoS_2 devices, which further rules out the possibility that the magnitude difference comes from the material characteristics.

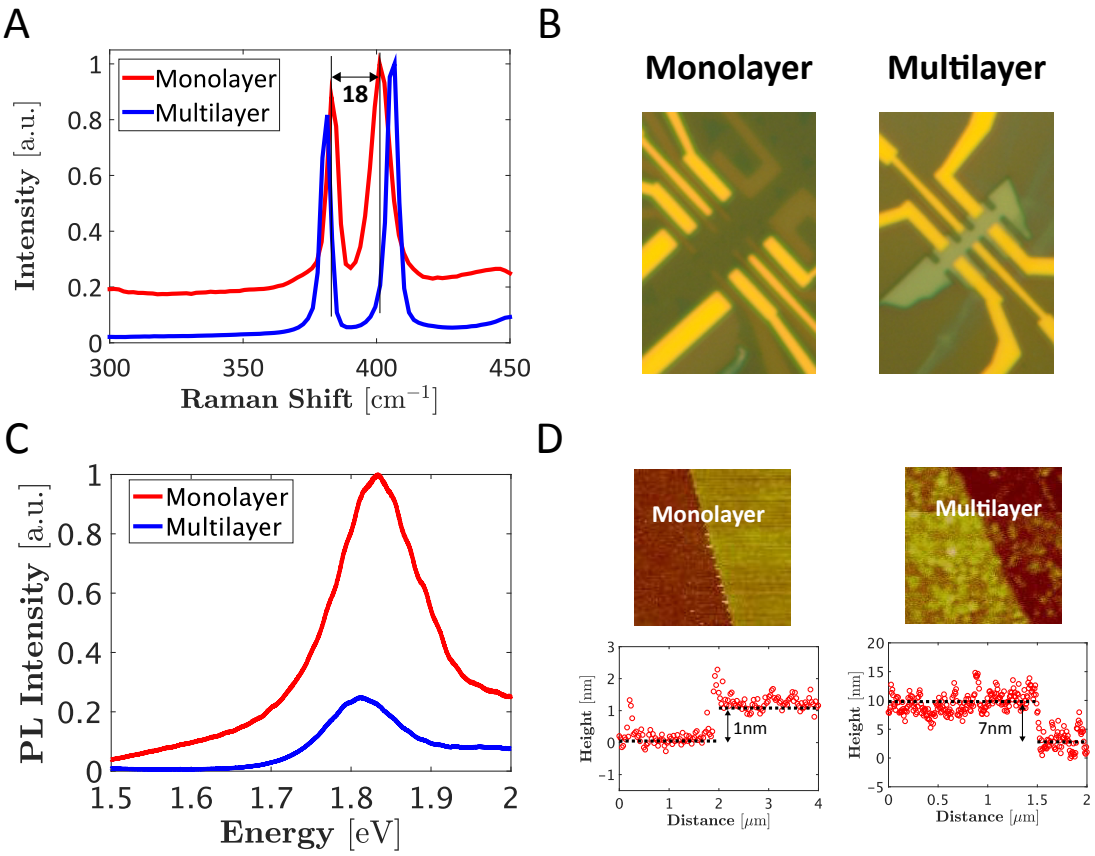

Fig. 3.12. Device layer number confirmations. (A) Two prominent Raman characteristic peaks for MoS_2 flakes. Monolayer presents a distinguished Raman shift of $18cm^1$ between the E^1_{2g} and A_{1g} peaks. (B) Representative optical images for monolayer and multilayer MoS_2 devices. (C) Photoluminescence spectroscopy (PL) of monolayer and multi-layer MoS_2. (D) AFM images and height profiles of monolayer and multi-layer MoS_2.

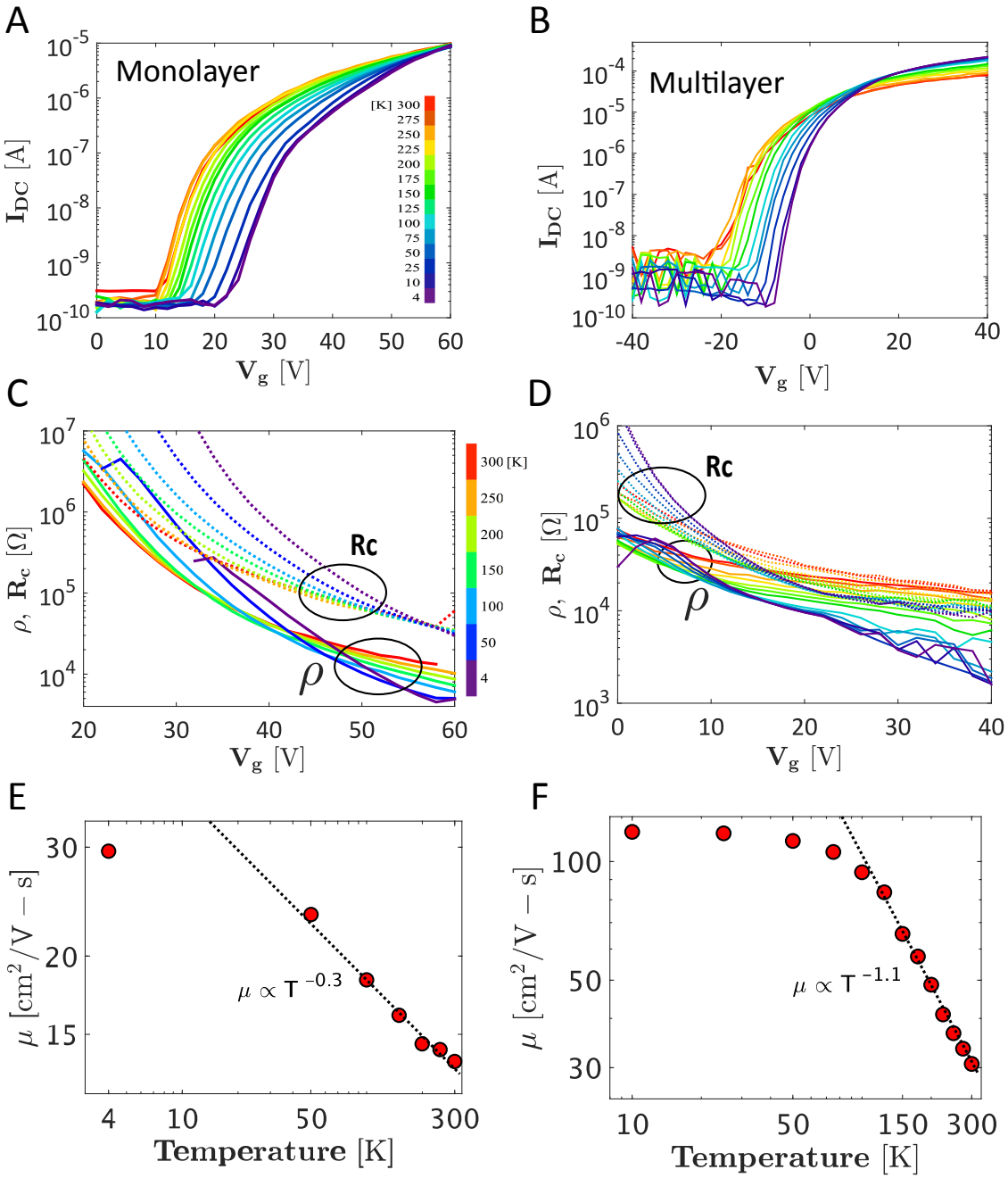

Fig. 3.13. Device electrical characterizations. Transfer characteristics at different temperatures for monolayer (A) and multi-layer (B) MoS_2 devices. Four-probe measurements using type II set up described in Fig. 3.1 to extract sheet resistance ρ and contact resistance R_c in monolayer (C) and multi-layer (D) devices. Extracted field-effect mobility as a function of temperature for monolayer (E) and multi-layer (F) MoS_2.

4. COUPLED VALLEY AND SPIN HALL EFFECT IN MONOLAYER WSE_2

Part of the material in this chapter would be submitted for review, Terry Y.T. Hung, Avinash Rustagi, Shengjiao Zhang, Pramey Upadhyaya1, Zhihong Chen, Experimental observation of coupled valley and spin Hall effect in p-doped WSe_2 devices

Giant spin Hall effect (GSHE) has been observed in heavy metal materials such as Ta, Pt, and W, where spins are polarized in the surface plane and perpendicular to the charge current direction [7–9]. Spins generated in these materials have successfully switched magnets with in-plane magnetic anisotropy (IMA) and perpendicular magnetic anisotropy (PMA) through spin orbit torque (SOT) mechanism. It is generally accepted that PMA magnets are preferred over IMA magnets in data storage applications owing to their large thermal stability even at ultra-scaled dimensions. However, SOT switching of PMA magnets by conventional GSHE materials requires either a small external magnetic field [87, 88], a local dipolar field, or introducing tilted anisotropy to break the symmetry with respect to the magnetization [89, 90]. To deterministically switch a PMA without any additional assistance, nonconventional GSHE materials that can generate spins with polarization perpendicular to the surfaces are needed. Several monolayer transition metal dichalcogenides (TMDs) have been predicted to generate such out-of-plane spins due to their 2D nature and unique band structures [10, 44, 91]. Interestingly, opposite spins are locked to their respective sub-band in each valley of the TMD valence band with a substantial energy splitting, which can be accessed through electrical gating and spatially separated by electric field through the valley Hall effect (VHE) [13, 18–20, 34]. Therefore, spatial separation and accumulation of spins in these 2D TMDs are uniquely defined as spin-locked valley Hall effect (SVHE). Here we report an experiment of electri-

cal generation of spin current with out-of-plane polarization in monolayer WSe_2 and detection of spin signals through a non-local spin valve structure built on a lateral graphene spin diffusion channel that partially overlaps with WSe_2. A p-type doping scheme is employed to allow easy access to sufficient amount of hole carriers in the valence band of WSe_2. Holes with out-of-plane spin polarization selected by the polarity of the charge current through VHE are injected to the graphene channel and finally detected by non-local ferromagnetic contacts. This is the first demonstration of an all electrical device that can generate and accumulate out-of-plane spins, which can be an important spin source for PMA based SOT-random access memory (SOT-RAM) and possibly leads to new spin-valleytronics and novel quantum device applications.

4.1 Introduction

The manipulation of entangled charge, spin, and valley degree of freedom in TMDs materials has attracted a lot of attention. Valley Hall effect has been theoretically predicted in monolayer TMDs [10,44] and experimentally demonstrated in all electrical devices by our group [18] and Wu et al. [34] in MoS_2. Broken inversion symmetry induced non-zero Berry curvature (Ω) in such materials gives rise to an anomalous transverse velocity (second term), in addition to the longitudinal group velocity (first term), which can be described by

$$\mathbf{v} = \frac{\partial \varepsilon}{\partial \mathbf{k}} - \frac{\mathbf{e}}{\hbar}\mathbf{E} \times \mathbf{\Omega}(\mathbf{k}) \tag{4.1}$$

,where ε is the energy, k is the wave vector, E is the electric field, e is the element charge, and $\hbar$ is the reduced Plancks constant. Valley current, therefore, occurs in the transverse direction with respect to the applied electric field. Furthermore, preserved time reversal symmetry enforces opposite signs of Berry curvature and spin polarization in the adjacent K valleys

$$\begin{aligned} \mathbf{\Omega}(\mathbf{K}) &= \mathbf{\Omega}(-\mathbf{K}) \\ \mathbf{s}(\mathbf{K}) &= -\mathbf{s}(-\mathbf{K}) \end{aligned} \tag{4.2}$$

where s is the spin polarization. Due to the large spin splitting ($\Delta E \sim 450meV$) in the valence band of monolayer WSe_2 [44], spin polarized holes are found in K and $-K$ valley with opposite signs at the Fermi level, a phenomenon that is called spin-valley locking. Consequently, spins can then be separated resulting flow of spin current in the transverse direction wherever the valley current flows. Besides, 2D nature of the materials ensures these spins to have out-of-plane polarizations that can switch PMA magnets more efficiently. More importantly, this type of SOT switching does not require external field assistance or special engineering of the PMA magnets. Several optical experiments have shown ultra-long valley life time in TMD and their heterostructure devices and associate that to long spin life time based on the spin-locking theory. However, these measurements, including photoluminescence, pump-probe using circularly polarized light, and Kerr rotation microscopy, the information of spin and valley degrees of freedom are convoluted [14, 71, 74, 92, 93] and do not directly probe the spin polarization. To date, only Luo et al. [16]. succeeded in detecting spin directly by employing a MoS_2/graphene hybrid structure. In their experiment, valleys/spins were optically excited in monolayer MoS_2 with circularly polarized light and subsequently injected to a graphene channel where spins were identified through Hanle measurements. However, a direct proof of electrical generation of spins is yet to be demonstrated. It is important to note that giant spin splitting only occurs in the valence bands of few semiconducting TMDs compared to the negligible splitting in their conduction bands and WSe_2 is predicted to have the largest splitting of $\sim 450meV$ [44]. Here, we demonstrate spin generation and detection all electrically in a WSe_2/graphene hybrid device and provide experimental evidences for the first time that generated spins are indeed out-of-plane polarized and locked to respective valleys that can be spatially separated.

4.2 Anomalous Hall Effect of Ferromagnet

To detect the diffused spins with out-of-plane polarization, a PMA FM is trivial way in the non-local valve setup [33, 94, 95]. However, high quality PMA stacks are normally deposited by sputtering that unavoidably damages the underlying graphene due to the highly energetic sputtered particles. Alternatively, we chose e-beam evaporated Py as the FM contact, which does not damage the underlying graphene but can only carry in-plane magnetic anisotropy. By scanning an out-of-plane magnetic field along the z direction (B_z), the magnetization of the Py spin probe will be gradually pulled out-of-plane and be able to probe the chemical potential of the incoming out-of-plane spins. Operating the spin probe in the hard-axis (z) brings a continuous change of the non-local voltage reading that is corresponding to the magnetization component along the z direction (m_z). To access m_z of Py magnet responding to the applied B_z field, we performed an independent anomalous Hall effect (AHE) measurement on a Py Hall bar device that has gone through the exact same fabrication processes as the test device depicted in Fig. 4.2a. In Fig. 4.1, the anomalous Hall resistance, R_{AHE}, increases with B_z in both field directions since the magnetization of Py continuously rotates from y (in-plane, easy axis) to z (out-of-plane) direction, indicated by the arrows in the side view of the schematic AHE setup. Clear saturation is observed at large B_z fields (marked as blue regions) when the magnetization of the Py electrode is completely pulled out of plane and m_z reached its maximum value, i.e. $m_z^{norm} = m_z/|max(m_z)| = \pm 1$.

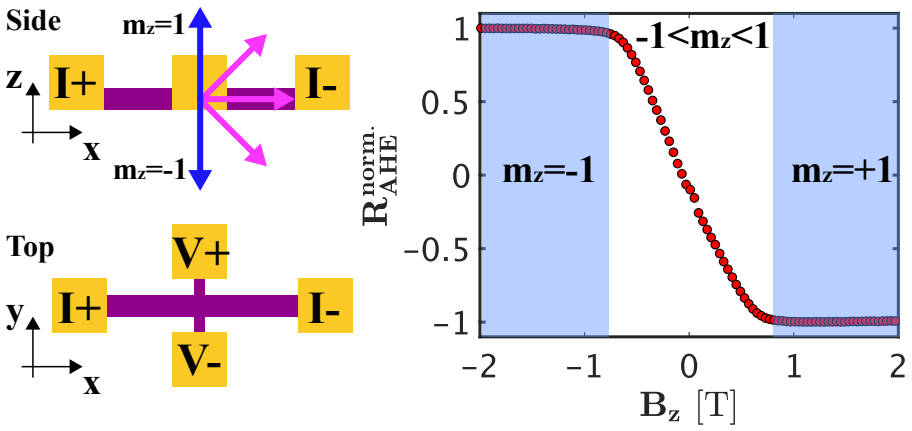

Fig. 4.1. Ferromagnet characterization through anomalous Hall effect (AHE). On the left are the side view and top view of the device where purple area is FM(Py) and yellow areas are contacting NM. Blue and magenta arrows indicate the magnetization of the FM(Py). On the right is the measured AHE which has two blue regions and one white region corresponding to the saturation of m_z and the transition in between respectively.

4.3 Out-of-plane Spins

Knowing how the Py probe behaves under the B_z field, we are now able to understand how it probes the chemical potential of the diffused spins in the graphene channel. In the device shown in Fig. 4.2a, b, when the DC charge current (I_{DC}) is applied across electrodes 1 and 2, spin current generated in WSe_2 through SVHE gets injected into graphene and spins diffuse towards $+x$ direction with chemical potential of the spins exponentially decaying along the graphene channel, as shown in Fig. 4.3 schematic. Therefore, with the field dependent mz change in the Py FM, one can observe the change of non-local voltage (V_{nl}) across electrodes 3 and 4 as a function of the applied B_z field. Non-local resistance, R_{nl}, that is defined by V_{nl}/I_{DC} as a function of applied B_z field was measured over few devices and the average behaviors of three sets of data are shown in Fig. 4.3a. Averaging technique was applied to enhance the signal to noise. The blue regions show clear saturation in R_{nl} that can be correlated

to the saturation of m_z in the FM probe mentioned above. In fact, the overall behavior of R_{nl} as a function of Bz (green dots) can be well described by the change of m_z component in the FM (black line) that was measured independently through the AHE shown in Fig. 4.1. Cartoons presented in Fig. 4.2a illustrate probing of the spin chemical potential under the FM probe when mz reaches its maximum values ($m_z^{norm} \pm 1$) at $|B_z| > 0.8T$. When $B_z = 0T$, no non-local signals are detected since the magnetization of the FM is perpendicular to the spin polarization in the channel. With the increasing $|B_z|$, R_{nl} continuously increases and reaches its maximum(minimum) value when the polarization of the spin current is parallel(anti-parallel) to the FM probe (blue regions marked in Fig. 4.2a). In addition, we fabricated another device with the identical structure except that the Py FM (electrode 3) was replaced with a non-magnetic electrode (NM) as our control sample. In this case, no spin chemical potential can be detected as expected, shown in Fig. 4.2b. The apparent differences between the test device and the control unambiguously point out that the observed increasing R_{nl} and its saturation at $|B_z| > 0.8T$ is the result of the interaction between the out-of-plane spins generated in WSe2 through SVHE and FM.

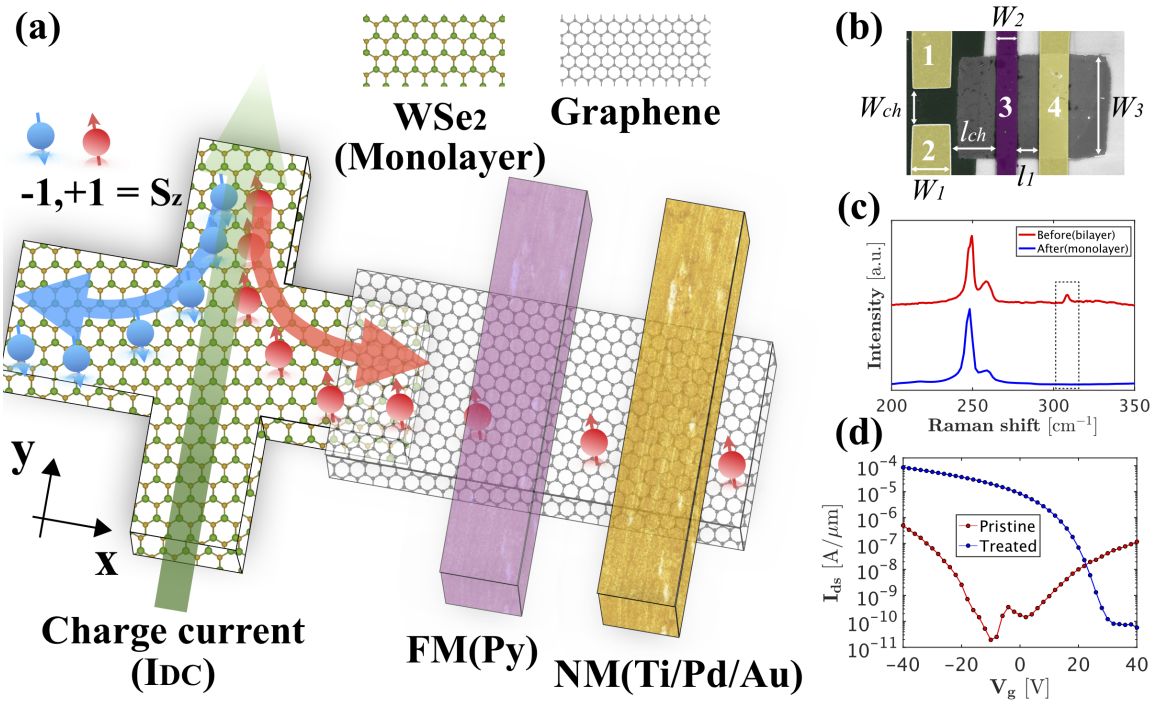

Fig. 4.2. Geometry of the devices and characterizations. a, Schematic of spin-locked valley Hall effect in monolayer WSe_2 and the non-local valve measurement scheme across FM and NM. b, Detailed geometry of the devices where yellow electrodes (1, 2, 4) are NM, purple electrode (3) is FM, green area is monolayer WSe_2, and grey area is graphene. c, Raman spectrum measured on green area shows no peak $\sim 308\ cm^{-1}$ (circled) which is responsible for the interlayer interaction. i.e. The peak around $\sim 308\ cm^{-1}$ will only show up when it is not monolayer. d, Typical transfer characteristic of pristine monolayer WSe_2 (red). The treated monolayer WSe_2 transfer characteristic measured across electrode 1 and 2 (blue).

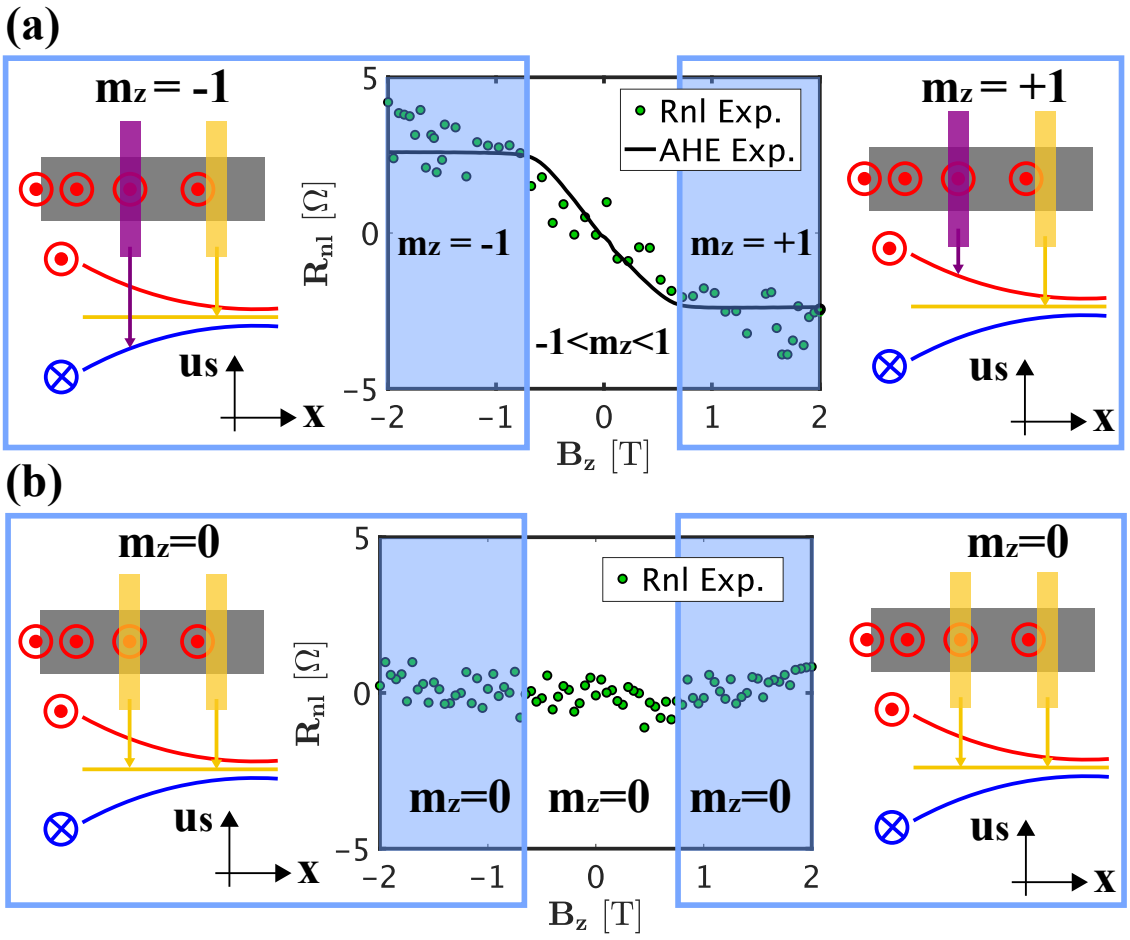

Fig. 4.3. Non-local valve measurements and corresponding probing schemes. a, Non-local measurement of the device depicted in Fig. 1a and the corresponding probing schemes at fixed spin current (polarity). Black line in the plot (named AHE Exp.) is the measurement from Fig. 2 with rescaled R_{AHE} value. Red dots and blue crosses are spin polarization along +z and -z directions. Red, blue, and yellow lines are spin chemical potential of ($m_z = +1$), ($m_z = -1$), and ($m_z = 0$) respectively. b, Same measurement with FM electrode (purple) being replaced with NM electrode (yellow).

4.4 Spin Polarization and Current Polarity

To study the spin polarization under opposite electric field directions, we plot the non-local voltage reading, V_{nl}, as a function of B_z at opposite charge current (I_{DC}) polarities. Anomalous velocity ($= -e/\hbar\ E \times \Omega(K)$) with a given Berry curvature will change its sign when the direction of the electric field is changed. As a result, spin current with the opposite polarization will now diffuse to the graphene channel, as depicted in Fig. 4.4. The two possible states of spin polarization ($s_z = \pm 1$) and two FM magnetization directions ($m_z > 0$ or < 0) give rise to four possible combinations, labeled in their respective quadrant. Such I_{DC} polarity dependency further confirms the generation of out-of-plane spins from WSe_2 and resonates with the spin-locked VHE physics. In summary, we have experimentally demonstrated for the first time that out-of-plane spins can be generated in monolayer WSe_2 electrically through spin-locked VHE in the valence band. For a given current polarity, the measured saturation states showing opposite R_{nl} values at large B_z fields are attributed to the change of the FM magnetization. On the other hand, the measured two R_{nl} states under the same magnetic field with opposite current polarities are attributed to the change of the out-of-plane spin current polarities in the z direction. Our experiment provides unambiguous evidences that valley locked out-of-plane spins can be electrically generated and accumulated, which sheds light on a possible route to achieve PMA based SOT devices that are currently not existing.

In summary, we have experimentally demonstrated for the first time that out-of-plane spins can be generated in monolayer WSe_2 electrically through spin-locked VHE in the valence band. For a given current polarity, the measured saturation states showing opposite R_{nl} values at large B_z fields are attributed to the change of the FM magnetization. On the other hand, the measured two R_{nl} states under the same magnetic field with opposite current polarities are attributed to the change of the out-of-plane spin current polarities in the z direction. Our experiment provides unambiguous evidences that valley locked out-of-plane spins can be electrically gen-

erated and accumulated, which sheds light on a possible route to achieve PMA based SOT devices that are currently not existing.

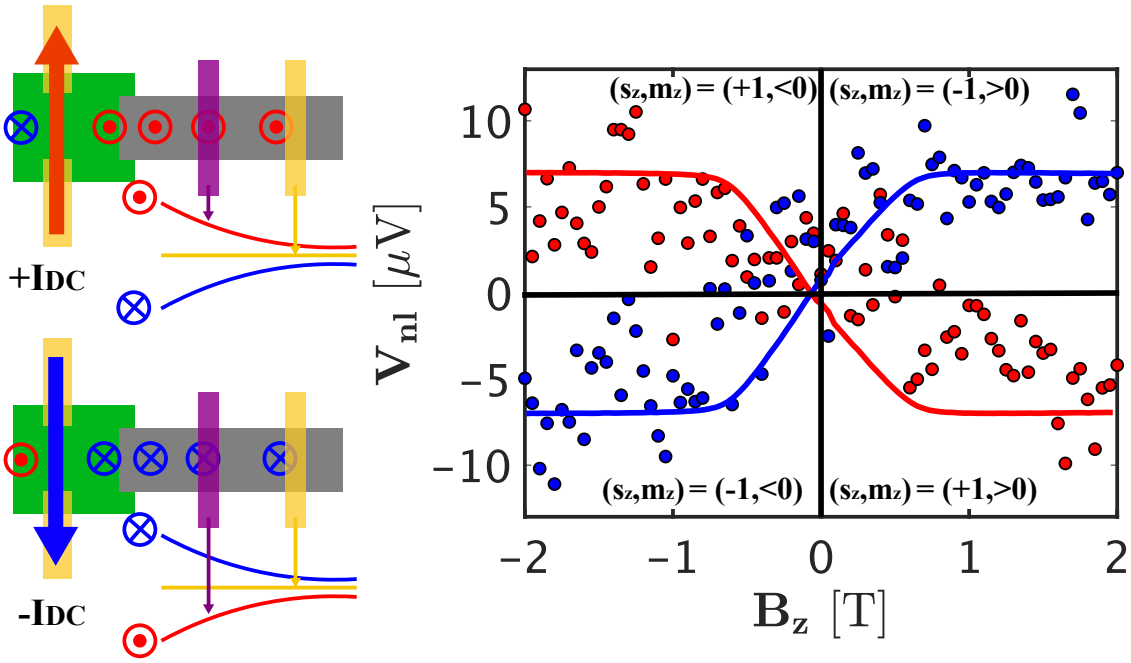

Fig. 4.4. Current and spin polarity relation study through non-local valve measurements. On the left shows the schematics of how spin current (polarity) changes with respect to the change of current polarity. On the right is the $V_n l$ measurements with respect to the applied B_z field at opposite current polarities. Corresponding spin polarity on the right-hand side of current path and FM magnetization (s_z,m_z) are shown in the plot.

4.5 Tight-binding Model and Berry Curvature

Within the $\vec{k} \cdot \vec{p}$ theory, the low energy effective Hamiltonian that describes the energy dispersion near the $\vec{K}$ and $\vec{K}'$ points of monolayer WSe_2 is

$$\mathbf{H} = \frac{\mathbf{at}}{\hbar}(\tau\sigma_{\mathbf{x}}\mathbf{p_x} + \sigma_{\mathbf{y}}\mathbf{p_y}) + \frac{\mathbf{\Delta}}{\mathbf{2}}\sigma_{\mathbf{z}} - \lambda\tau\frac{\sigma_{\mathbf{z}} - \mathbf{1}}{\mathbf{2}}\mathbf{s_z} \tag{4.3}$$

where $a = 3.310\mathring{A}$ is the lattice constant, t = 1.19 eV is the hopping parameter, $\tau = \pm 1$ is the corresponding valley index ($\vec{K}/\vec{K}'$), $\sigma_{x/y/z}$ are the pseudo-spin Pauli matrices corresponding to the sub-lattice degree of freedom, $\Delta = 1.60\ eV$ is the energy gap, $2\lambda = 0.46\ eV$ is the spin-splitting in the valence band, and s_z corresponds to the spin Pauli matrix. The energy dispersion is therefore

$$\mathbf{E(k)} = \frac{\lambda\mathbf{s_z}\tau}{\mathbf{2}} + \alpha\frac{\mathbf{1}}{\mathbf{2}}\sqrt{\mathbf{\Delta'^2} + \mathbf{4a^2t^2k^2}} \tag{4.4}$$

where $\alpha = \pm 1$ corresponds to conduction band (CB) and valence band (VB), $s_z = \pm 1$ corresponds to up/down spin, $\tau = \pm 1$ corresponds to $\vec{K}/\vec{K}'$ valleys, and $\Delta' = \Delta - \lambda\tau s_z$ shown in Fig. 4.5. The absence of inversion symmetry and the presence of large spin-orbit interaction due to the heavy transition metal atoms allows for the bands in monolayer transition metal dichalcogenides to have finite Berry curvature. These curvatures (i.e. effective magnetic field in the momentum space) are

$$\begin{aligned} \mathbf{\Omega(k)} = -\mathbf{z}\tau\frac{\mathbf{2a^2t^2\Delta'}}{\mathbf{(4a^2t^2k^2 + \Delta'^2)^{3/2}}} \equiv -\mathbf{z}\tau\mathbf{\Omega_0} \\ \mathbf{\Omega_c(k)} = -\mathbf{\Omega_v(k)} \equiv \mathbf{z}\tau\mathbf{\Omega_0} \end{aligned} \tag{4.5}$$

where

$$\mathbf{\Omega_0} = \frac{\mathbf{2a^2t^2\Delta'}}{\mathbf{(4a^2t^2k^2 + \Delta'^2)^{3/2}}} \tag{4.6}$$

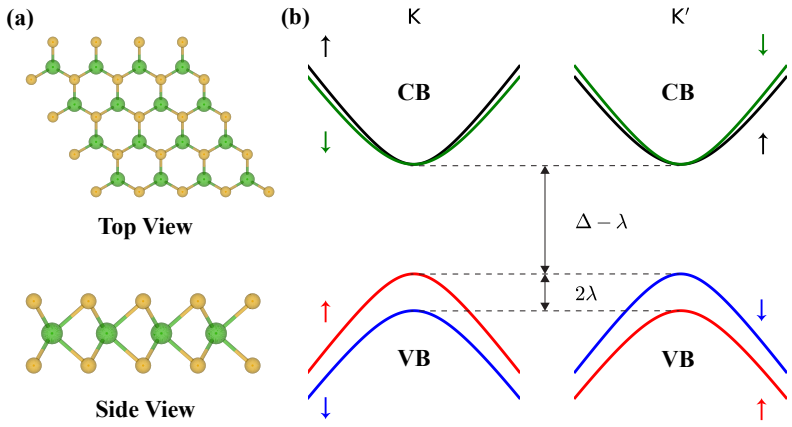

Fig. 4.5. WSe_2 Lattice and Band Structure. a Lattice structure displaying the absence of inversion symmetry. b Tight-binding model bandstructure of monolayer WSe_2.

4.6 Spin Polarity from Theory

The finite Berry curvature of the bands allows for valley Hall effect which can be measured electrically based on the device schematic in Fig. 4.6. Based on the information at hand, it is possible to evaluate the sign of the non-local voltage when the magnet is completely saturated out of plane by the application of a large external field. The semiclassical equations that govern the Bloch electron wavepacket dynamics for electron in the n-th band with wavevector k and position r and experiencing real space electric and magnetic fields are

$$\begin{aligned} \dot{\mathbf{r}} &= \frac{\mathbf{1}}{\hbar}\frac{\partial \mathbf{E}}{\partial \mathbf{k}} - \dot{\mathbf{k}} \times \mathbf{\Omega} \\ \hbar\dot{\mathbf{k}} &= -\mathbf{eE} - \mathbf{e}\dot{\mathbf{r}} \times \mathbf{B} \end{aligned} \tag{4.7}$$

Corresponding to the non-local measurement, a charge current is driven along the $+\hat{y}$ by application of an electric field E=Ey through p-doped WSe_2. Due to the large VB spin splitting in monolayer WSe2, only one of the spin split bands from

each inequivalent K/K valley participate in transport. In absence of any external magnetic field, the equation of motion simplifies to

$$\begin{aligned} \dot{\mathbf{r}} &= \frac{\mathbf{1}}{\hbar}\frac{\partial \mathbf{E}}{\partial \mathbf{k}} + \frac{\mathbf{eE}}{\hbar}\hat{\mathbf{y}} \times \mathbf{\Omega_v} \\ \dot{\mathbf{r}} &= \frac{\mathbf{1}}{\hbar}\frac{\partial \mathbf{E}}{\partial \mathbf{k}} + \frac{\mathbf{eE}}{\hbar}\mathbf{\Omega_v}\tau\hat{\mathbf{x}} \end{aligned} \tag{4.8}$$

where

$$\dot{\mathbf{x}} \propto \frac{\mathbf{eE\Omega_v}}{\hbar}\tau \tag{4.9}$$

Hence, for the K-valley electrons ($\tau = +1$): $\dot{x} > 0$ and those are right moving. Due to spin-split electronic bands in the valley, we can conclude that the K-valley electrons participating in transport are of the spin up type. There are a few key steps in understanding what the magnet measures (spin up/down electrochemical potentials). To resolve this, let us consider the case of magnetization pointing along the $+z$ direction. Magnetization along $+z$ implies the electron spins in ferromagnet (FM) are along $-z$ (reason the negative gyromagnetic ratio for electrons). Since the electrons spins in magnet are along $-z$, the spin down electrons are able to tunnel into/from the magnet and equilibrate. The non-magnetic (NM) metal always measures the average electrochemical potential of the up and down spin electrons. Thus, the non-local voltage defined as $V_{nl} = V_{NM} - V_{FM} = \frac{\mu_{NM} - \mu_{FM}}{-e}$. Due to the established equilibrium, the ferromagnet measures the lower electrochemical potential for spin down electrons. Thus, since $\mu_{NM} < \mu_{FM}$, the non-local voltage V_{nl} measured is < 0. In analogy, when the magnetization of the magnet is along the -z direction, the non-local potential $V_{nl} = V_{FM} - V_{NM} > 0$.

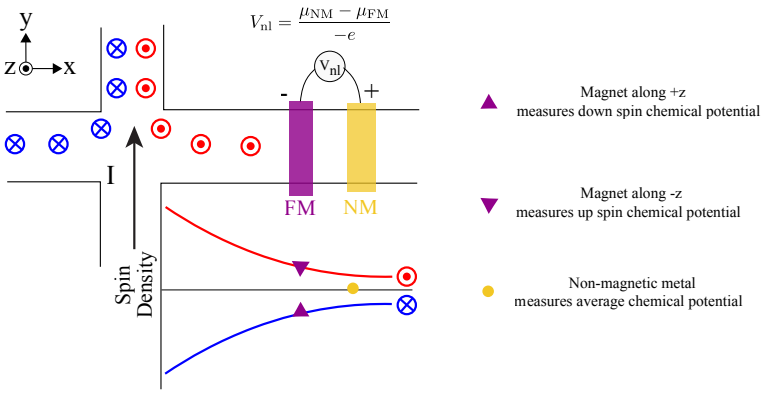

Fig. 4.6. Non-Local Measurement Geometry for the Electrical Detection of Spin-locked VHE.

4.7 Estimation of Non-local Signal from Theory

Theoretical Model for Calculating Non-local Voltage

Our goal here is to model the non-local voltage measured by the FM/NM electrodes for which we will need to estimate the spatially varying valley chemical potential difference $\delta\mu_v = \mu_K - \mu_{K\prime}$. Here we follow the model in [21]. The scheme here is to divide the device into regions as shown in Fig. 4.7. In each region, the diffusion equation describing the valley chemical potential difference $\delta\mu_v = \mu_K - \mu_{K\prime}$ is solved self-consistently with the conductance matrix equation that accounts for the source term. The valley chemical potential difference $\delta\mu_v = \mu_K - \mu_{K\prime}$ follows the diffusion equation

$$\frac{\partial^2}{\partial \mathbf{x^2}}\delta\mu_{\mathbf{v}}^{\mathbf{i}} = \frac{\mathbf{1}}{(\mathbf{l}_{\mathbf{v}}^{\mathbf{i}})^{\mathbf{2}}}\delta\mu_{\mathbf{v}}^{\mathbf{i}} \tag{4.10}$$

where region $i = A, B, C$ and l_v^i is the inter-valley scattering length (processes by which the valley polarization is lost). The regions A and B are WSe_2 and region C is graphene. The equation relating the charge current (along y-direction) and valley current (along x-direction) to their corresponding generalized forces namely electric

field (along y-direction) and gradient of valley chemical potential difference (along x-direction) are related as

$$\begin{pmatrix} j_c^i \\ j_v^i \end{pmatrix} = \begin{pmatrix} \sigma_{xx,i} & -\sigma_{xy,i}^{VH} \\ \sigma_{xy,i}^{VH} & \sigma_{xx,i} \end{pmatrix} \begin{pmatrix} E_i \\ -\frac{1}{2e}\frac{\partial}{\partial x}\delta\mu_v^i \end{pmatrix} \tag{4.11}$$

Typically, when the materials are pure, the inter-valley scattering are caused by the edge of the devices. Thus, for the device geometry shown, $l_v^A = l_v, l_v^B = \infty$ (since there are no edges assuming contacts for charge current flow are ideal), and $l_v^C = l\prime_v$. The WSe_2 regions A and B have non-zero valley hall conductance and are characterized by $\sigma_{xx,A/B} = \sigma_{xx}$ and $\sigma_{xy,A/B}^{VH} = \sigma_{xy}^{VH}$. For region C i.e. graphene, no berry curvature implies absence of valley hall conductance. Therefore, $\sigma_{xx,C} = \sigma\prime_{xx}$ and $\sigma_{xy,C}^{VH} = 0$. The boundary conditions are $\delta\mu_v^A(x = -\infty) = 0$ and $\delta\mu_v^C(x = +\infty) = 0$. As for the interfaces, the assumed conditions are continuity of valley chemical potential difference and continuity of valley current across at the interface of region A and B. However, the WSe_2-graphene interface in general lead to the boundary conditions of discontinuity in valley chemical potential and valley current resulting in valley memory loss. This is similar to the spin memory loss due to interfaces when studying spin hall effect. Analogous to spin hall, the discontinuity in valley chemical potential difference can be thought of as the asymmetry in interface resistance corresponding to the two different valley electrons due to valley conserving scattering. This leads to potential drop across the resistances and thus corresponds to discontinuity in valley chemical potentials. On the other hand, the interface can also lead to valley flip scattering and this in turn implies discontinuity in valley current illustrated through the two-channel resistor model in Fig. 4.9. Thus, in the simplest of models for the interface, we can parameterize the interface effects by means of the opacity parameters and corresponding to discontinuity in valley chemical potential difference and valley current. The charge current and electric field in region B is $j = I/w$ and E respectively. The interface conditions thus imply,

$$\begin{aligned} \delta\mu_{\mathbf{v}}^{\mathbf{A}}\left(\mathbf{x}=-\mathbf{w2}\right) &= \delta\mu_{\mathbf{v}}^{\mathbf{B}}\left(\mathbf{x}=-\mathbf{w2}\right) \\ (\mathbf{1}-\alpha)\delta\mu_{\mathbf{v}}^{\mathbf{B}}\left(\mathbf{x}=\mathbf{w2}\right) &= \delta\mu_{\mathbf{v}}^{\mathbf{C}}\left(\mathbf{x}=\mathbf{w2}\right) \end{aligned} \tag{4.12}$$

where $1-\alpha$ corresponds to the transparency of the valley chemical potential across the WSe2-graphene interface, and for the valley current

$$\begin{aligned} \mathbf{j}_{\mathbf{v}}^{\mathbf{A}}\left(\mathbf{x}=-\mathbf{w2}\right) &= \mathbf{j}_{\mathbf{v}}^{\mathbf{B}}\left(\mathbf{x}=-\mathbf{w2}\right) \\ (\mathbf{1}-\beta)\mathbf{j}_{\mathbf{v}}^{\mathbf{B}}\left(\mathbf{x}=\mathbf{w2}\right) &= \mathbf{j}_{\mathbf{v}}^{\mathbf{C}}\left(\mathbf{x}=\mathbf{w2}\right) \end{aligned} \tag{4.13}$$

where $1-\beta$ corresponds to the transparency of the valley current across the WSe_2-graphene interface. The diffusion equation is solved in a self-consistent manner alongside the conductance equation (which accounts for the source term) to determine the spatially varying valley chemical potential difference in graphene that is measured,

$$\delta\mu_{\mathbf{v}}^{\mathbf{C}} = \mathbf{I}\exp\left(-\frac{\mathbf{x}-\mathbf{w}/\mathbf{2}}{\mathbf{l}\prime_{\mathbf{v}}}\right)\frac{\mathbf{2e}\mathbf{l}\prime_{\mathbf{v}}\sigma_{\mathbf{xy}}^{\mathbf{VH}}}{\sigma_{\mathbf{xx}}\sigma\prime_{\mathbf{xx}}}\frac{\mathbf{1}-\beta}{\left(\frac{\mathbf{1}-\beta}{\mathbf{1}-\alpha}\right)\frac{\mathbf{l}\prime_{\mathbf{v}}}{\mathbf{l}\prime_{\mathbf{v}}}\left[\frac{\left(\sigma_{\mathbf{xy}}^{\mathbf{VH}}\right)^{\mathbf{2}}}{\sigma_{\mathbf{xx}}}+\sigma_{\mathbf{xx}}\right]+\mathbf{l}_{\mathbf{v}}+\mathbf{w}} \tag{4.14}$$

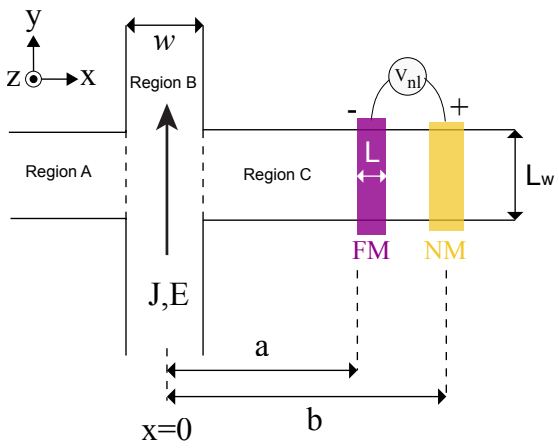

Fig. 4.7. Schematic of device for non-local electrical generation and detection of SVHE.

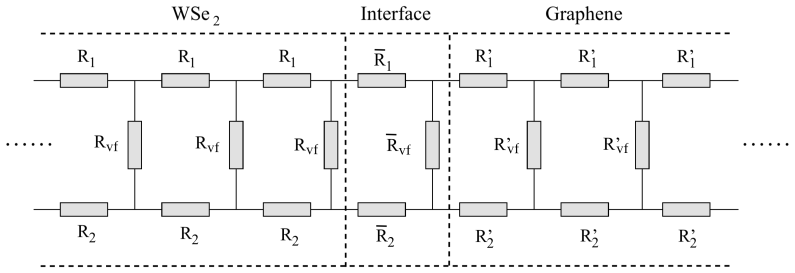

Fig. 4.8. Two-channel Model for the Interface Accounting for the Discontinuity in Chemical Potential ($\bar{R}_{\mathbf{1}}$, $\bar{R}_{\mathbf{2}}$) and valley current ($\bar{R}_{vf}$).

Numerical Estimate: Upper Bond

To make an estimate for the upper bound for the saturated non-local voltage amplitude, we consider the most pristine case where there are no losses at the interface (i.e. $\alpha == 0$). WSe_2 and graphene have similar spin diffusion lengths (i.e. $l_v = 0.6\mu m$ and $l_v = 1\mu m$) and longitudinal conductivities $\sigma_{xx} = 2.5e^2/h(\equiv 10k\Omega)$ and $\sigma\prime_{xx} = 5e^2/h(\equiv 5k\Omega)$. For the Valley Hall $\sigma_{xy}^{VH} \approx 2e^2/h$. The DC current used in measurement is 2 μA. The left edge of the ferromagnet electrode is at $a = 1.2\mu m$ and of width $L = 1\mu m$. Thus, the average chemical potential it measures is

$$\left\langle \delta\mu_{\mathbf{v}}^{\mathbf{C}} \right\rangle = \frac{\mathbf{1}}{\mathbf{L}} \int_{\mathbf{a}+\frac{\mathbf{w}}{\mathbf{2}}}^{\mathbf{a}+\frac{\mathbf{w}}{\mathbf{2}}+\mathbf{L}} \mathbf{dx}\delta\mu_{\mathbf{v}}^{\mathbf{C}}(\mathbf{x}) = \frac{\mathbf{1}}{\mathbf{L}} \frac{\mathbf{2e}\mathbf{l}_{\mathbf{v}}^{\prime\,\mathbf{2}}\sigma_{\mathbf{xy}}^{\mathbf{VH}}}{\sigma_{\mathbf{xx}}\sigma_{\mathbf{xx}}^{\prime}} \frac{\mathbf{e}^{-\mathbf{a}/\mathbf{l}_{\mathbf{v}}^{\prime}} - \mathbf{e}^{-(\mathbf{a}+\mathbf{L})/\mathbf{l}_{\mathbf{v}}^{\prime}}}{\frac{\mathbf{l}_{\mathbf{v}}^{\prime}}{\sigma_{\mathbf{xx}}^{\prime}}\left[\frac{(\sigma_{\mathbf{xy}}^{\mathbf{VH}})^{\mathbf{2}}}{\sigma_{\mathbf{xx}}} + \sigma_{\mathbf{xx}}\right] + \mathbf{l}_{\mathbf{v}} + \mathbf{w}} \tag{4.15}$$

Assuming the contact width $w = 2\mu m$, and that no charge current flowing along the valley current in graphene, there is a symmetry in the chemical potential of the K and K valleys. Therefore$\left\langle \delta\mu_v^K \right\rangle = \left\langle \delta\mu_v^C \right\rangle/2$ and the non-local voltage is

$$\mathbf{V}_{\mathbf{nl}}^{\mathbf{0}} = \frac{\left\langle \delta\mu_{\mathbf{v}}^{\mathbf{C}} \right\rangle}{\mathbf{2e}} = \mathbf{4.6} \times \mathbf{10}^{-\mathbf{4}}\mathbf{V} \tag{4.16}$$

Here, to determine the upper bound of non-local voltage, we have assumed that the magnet is able to sense the chemical potential with unit efficiency. This is true if one of the spins sub-bands in the ferromagnet is full and there is no spin relaxation at the graphene-ferromagnet interface. However, in a general setting, if none of the spins sub-bands in the ferromagnet is full, the measured non-local voltage is reduced

by the polarization efficiency of the detector ferromagnet PD which was determined from experiments on graphene non-local spin valves to be $\sim 4\%$. Thus the upper bound on the measured non-local voltage is

$$\mathbf{V_{nl}^{m} = P_D V_{nl}^{0} = P_D \frac{\langle \delta \mu_v^C \rangle}{2e} = 1.84 \times 10^{-5} V} \tag{4.17}$$

To summarize, the difference between the actual measured non-local voltage and the theoretical upper bound estimation can be attribute to the quality of the WSe_2-graphene.

4.8 Device Characterization and Measurement Setup

Chemical vapor deposition (CVD) grown bilayer WSe_2 fakes were first transferred to a 90 (nm) SiO_2/Si substrate. Standard e-beam lithography was used to define Ti/Pd/Au (0.5nm/15nm/70nm) electrodes for transport measurements. A large area, continuous CVD graphene film was then transferred onto the sample covering all WSe_2 fakes underneath. A ferromagnetic (FM) contact with a capping layer (20nm Py/3nm Al) was defined on top of a graphene only region by another e-beam lithography and metallization step. Al_2O_3 was then deposited by atomic layer deposition (ALD) only in a lithographically patterned rectangular area as an etching mask in order to form an isolated graphene spin diffusion channel that overlaps with a small corner of the WSe_2 flake. Lastly, the sample was exposed to a gentle O2 plasma to finally etch away the unwanted graphene regions and p-dope WSe2 [ref] at the same time. Details of the doping scheme are described in the reference paper. In brief, the top layer of the bilayer WSe_2 gets converted to WO_x, which serves as a strong p-doping layer for the remaining WSe_2 layer underneath, allowing easy access to the hole carriers in the valence band. A schematic of the final device and its operation is illustrated in Fig. 4.2a. Charge current (I_{DC}) is applied on the WSe_2 portion of the device indicated by the green arrow along the y direction. Valleys/spins will be separated due to the valley Hall effect, resulting in a valley/spin current in the x direction with spin polarization pointing in the z direction. The valley/spin current following the $+x$

direction gets injected from the WSe_2 flake to the graphene layer sitting on top and diffuses towards the FM contact. On the right-hand side, spin chemical potentials are probed between the FM and the non-magnetic (NM) electrode. All measurements were conducted at room temperature. Raman spectra were measured to confirm the conversion of the bilayer to monolayer WSe_2 with the vanishing peak around $308cm^{-1}$, shown in Fig. 4.2b. Transfer characteristics of the WSe_2 device (Fig. 4.2c) show a strong hole current branch indicating a successful p-doping from the converted WO_x layer on top, in contrast to ambipolar characteristics with much lower hole current typically measured in monolayer WSe_2 devices.

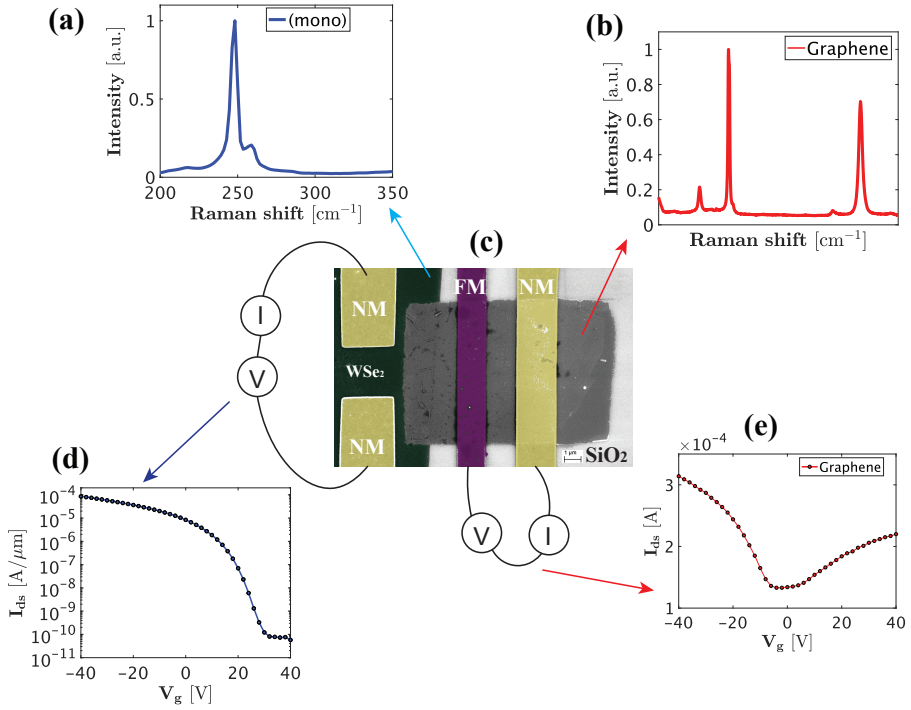

Fig. 4.9. Device Characterizations. (a, b) Raman spectra of monolayer WSe_2 and graphene respectively. (c) Colored SEM image where yellow electrodes are non-magnetic metal of Ti/Pd/Au (0.5nm /15nm /70nm), purple electrode is ferromagnetic metal of Py (20nm), green is monolayer WSe_2, rectangle grey area is graphene, and the substrate is 90nm SiO_2/Si. (d, e) Transfer characteristics of monolayer WSe_2 and graphene respectively.

REFERENCES

REFERENCES

[1] N. Nagaosa, J. Sinova, S. Onoda, A. MacDonald, and N. Ong, "Anomalous hall effect," *Reviews of modern physics*, vol. 82, no. 2, p. 1539, 2010.

[2] Y. Zhang, Y.-W. Tan, H. L. Stormer, and P. Kim, "Experimental observation of the quantum hall effect and berry's phase in graphene," *nature*, vol. 438, no. 7065, p. 201, 2005.

[3] J. Sinova, D. Culcer, Q. Niu, N. Sinitsyn, T. Jungwirth, and A. MacDonald, "Universal intrinsic spin hall effect," *Physical Review Letters*, vol. 92, no. 12, p. 126603, 2004.

[4] S. Murakami, N. Nagaosa, and S.-C. Zhang, "Dissipationless quantum spin current at room temperature," *Science*, vol. 301, no. 5638, pp. 1348–1351, 2003.

[5] J. Wunderlich, B. Kaestner, J. Sinova, and T. Jungwirth, "Experimental observation of the spin-hall effect in a two-dimensional spin-orbit coupled semiconductor system," *Physical review letters*, vol. 94, no. 4, p. 047204, 2005.

[6] Y. K. Kato, R. C. Myers, A. C. Gossard, and D. D. Awschalom, "Observation of the spin hall effect in semiconductors," *science*, vol. 306, no. 5703, pp. 1910–1913, 2004.

[7] L. Liu, C.-F. Pai, Y. Li, H. Tseng, D. Ralph, and R. Buhrman, "Spin-torque switching with the giant spin hall effect of tantalum," *Science*, vol. 336, no. 6081, pp. 555–558, 2012.

[8] C.-F. Pai, L. Liu, Y. Li, H.-W. Tseng, D. C. Ralph, and R. A. Buhrman, "Spin transfer torque devices utilizing the giant spin hall effect of tungsten," *Applied Physics Letters*, vol. 101, no. 12, p. 122404, 2012.

[9] L. Liu, T. Moriyama, D. Ralph, and R. Buhrman, "Spin-torque ferromagnetic resonance induced by the spin hall effect," *Physical review letters*, vol. 106, no. 3, p. 036601, 2011.

[10] D. Xiao, G.-B. Liu, W. Feng, X. Xu, and W. Yao, "Coupled spin and valley physics in monolayers of mos2 and other group-vi dichalcogenides," *Physical Review Letters*, vol. 108, no. 19, p. 196802, 2012.

[11] K. F. Mak, K. He, J. Shan, and T. F. Heinz, "Control of valley polarization in monolayer mos2 by optical helicity," *Nature nanotechnology*, vol. 7, no. 8, pp. 494–498, 2012.

[12] H. Zeng, J. Dai, W. Yao, D. Xiao, and X. Cui, "Valley polarization in mos2 monolayers by optical pumping," *Nature nanotechnology*, vol. 7, no. 8, pp. 490–493, 2012.

[13] K. F. Mak, K. L. McGill, J. Park, and P. L. McEuen, "The valley hall effect in mos2 transistors," *Science*, vol. 344, no. 6191, pp. 1489–1492, 2014.

[14] W.-T. Hsu, Y.-L. Chen, C.-H. Chen, P.-S. Liu, T.-H. Hou, L.-J. Li, and W.-H. Chang, "Optically initialized robust valley-polarized holes in monolayer wse 2," *Nature communications*, vol. 6, p. 8963, 2015.

[15] J. Lee, K. F. Mak, and J. Shan, "Electrical control of the valley hall effect in bilayer mos2 transistors," *Nature nanotechnology*, vol. 11, no. 5, pp. 421–425, 2016.

[16] Y. K. Luo, J. Xu, T. Zhu, G. Wu, E. J. McCormick, W. Zhan, M. R. Neupane, and R. K. Kawakami, "Opto-valleytronic spin injection in monolayer mos2/few-layer graphene hybrid spin valves," *Nano letters*, vol. 17, no. 6, pp. 3877–3883, 2017.

[17] L. D. Landau, E. M. Lifshitz, and L. Pitaevskii, "Statistical physics, part i," 1980.

[18] T. Y. Hung, K. Y. Camsari, S. Zhang, P. Upadhyaya, and Z. Chen, "Direct observation of valley-coupled topological current in mos2," *Science advances*, vol. 5, no. 4, p. eaau6478, 2019.

[19] R. Gorbachev, J. Song, G. Yu, A. Kretinin, F. Withers, Y. Cao, A. Mishchenko, I. Grigorieva, K. Novoselov, L. Levitov *et al.*, "Detecting topological currents in graphene superlattices," *Science*, vol. 346, no. 6208, pp. 448–451, 2014.

[20] M. Sui, G. Chen, L. Ma, W.-Y. Shan, D. Tian, K. Watanabe, T. Taniguchi, X. Jin, W. Yao, D. Xiao *et al.*, "Gate-tunable topological valley transport in bilayer graphene," *Nature Physics*, vol. 11, no. 12, pp. 1027–1031, 2015.

[21] Y. Shimazaki, M. Yamamoto, I. V. Borzenets, K. Watanabe, T. Taniguchi, and S. Tarucha, "Generation and detection of pure valley current by electrically induced berry curvature in bilayer graphene," *Nature Physics*, vol. 11, no. 12, pp. 1032–1036, 2015.

[22] W. Feng, Y. Yao, W. Zhu, J. Zhou, W. Yao, and D. Xiao, "Intrinsic spin hall effect in monolayers of group-vi dichalcogenides: A first-principles study," *Physical Review B*, vol. 86, no. 16, p. 165108, 2012.

[23] A. Splendiani, L. Sun, Y. Zhang, T. Li, J. Kim, C.-Y. Chim, G. Galli, and F. Wang, "Emerging photoluminescence in monolayer mos2," *Nano letters*, vol. 10, no. 4, pp. 1271–1275, 2010.

[24] Y. Liu, J. Guo, E. Zhu, L. Liao, S.-J. Lee, M. Ding, I. Shakir, V. Gambin, Y. Huang, and X. Duan, "Approaching the schottky–mott limit in van der waals metal–semiconductor junctions," *Nature*, vol. 557, no. 7707, p. 696, 2018.

[25] S. Das, H.-Y. Chen, A. V. Penumatcha, and J. Appenzeller, "High performance multilayer mos2 transistors with scandium contacts," *Nano letters*, vol. 13, no. 1, pp. 100–105, 2012.

[26] R. Kappera, D. Voiry, S. E. Yalcin, B. Branch, G. Gupta, A. D. Mohite, and M. Chhowalla, "Phase-engineered low-resistance contacts for ultrathin mos 2 transistors," *Nature materials*, vol. 13, no. 12, p. 1128, 2014.

[27] X. Cui, G.-H. Lee, Y. D. Kim, G. Arefe, P. Y. Huang, C.-H. Lee, D. A. Chenet, X. Zhang, L. Wang, F. Ye *et al.*, "Multi-terminal transport measurements of mos2 using a van der waals heterostructure device platform," *Nature nanotechnology*, vol. 10, no. 6, pp. 534–540, 2015.

[28] J.-R. Chen, P. M. Odenthal, A. G. Swartz, G. C. Floyd, H. Wen, K. Y. Luo, and R. K. Kawakami, "Control of schottky barriers in single layer mos2 transistors with ferromagnetic contacts," *Nano letters*, vol. 13, no. 7, pp. 3106–3110, 2013.

[29] L. Cai, C. J. McClellan, A. L. Koh, H. Li, E. Yalon, E. Pop, and X. Zheng, "Rapid flame synthesis of atomically thin moo3 down to monolayer thickness for effective hole doping of wse2," *Nano letters*, vol. 17, no. 6, pp. 3854–3861, 2017.

[30] M. Yamamoto, S. Nakaharai, K. Ueno, and K. Tsukagoshi, "Self-limiting oxides on wse2 as controlled surface acceptors and low-resistance hole contacts," *Nano letters*, vol. 16, no. 4, pp. 2720–2727, 2016.

[31] P. Zhao, D. Kiriya, A. Azcatl, C. Zhang, M. Tosun, Y.-S. Liu, M. Hettick, J. S. Kang, S. McDonnell, S. KC *et al.*, "Air stable p-doping of wse2 by covalent functionalization," *ACS nano*, vol. 8, no. 10, pp. 10 808–10 814, 2014.

[32] N. Tombros, C. Jozsa, M. Popinciuc, H. T. Jonkman, and B. J. Van Wees, "Electronic spin transport and spin precession in single graphene layers at room temperature," *Nature*, vol. 448, no. 7153, p. 571, 2007.

[33] C.-C. Lin, Y. Gao, A. V. Penumatcha, V. Q. Diep, J. Appenzeller, and Z. Chen, "Improvement of spin transfer torque in asymmetric graphene devices," *ACS nano*, vol. 8, no. 4, pp. 3807–3812, 2014.

[34] Z. Wu, B. T. Zhou, X. Cai, P. Cheung, G.-B. Liu, M. Huang, J. Lin, T. Han, L. An, Y. Wang *et al.*, "Intrinsic valley hall transport in atomically thin mos 2," *Nature communications*, vol. 10, no. 1, p. 611, 2019.

[35] P. Jacquod, R. S. Whitney, J. Meair, and M. Büttiker, "Onsager relations in coupled electric, thermoelectric, and spin transport: The tenfold way," *Physical Review B*, vol. 86, no. 15, p. 155118, 2012.

[36] H. Medina, J.-G. Li, T.-Y. Su, Y.-W. Lan, S.-H. Lee, C.-W. Chen, Y.-Z. Chen, A. Manikandan, S.-H. Tsai, A. Navabi *et al.*, "Wafer-scale growth of wse2 monolayers toward phase-engineered hybrid wo x/wse2 films with sub-ppb no x gas sensing by a low-temperature plasma-assisted selenization process," *Chemistry of Materials*, vol. 29, no. 4, pp. 1587–1598, 2017.

[37] H. Yang, A. Giri, S. Moon, S. Shin, J.-M. Myoung, and U. Jeong, "Highly scalable synthesis of mos2 thin films with precise thickness control via polymer-assisted deposition," *Chemistry of Materials*, vol. 29, no. 14, pp. 5772–5776, 2017.

[38] H. Yu, M. Liao, W. Zhao, G. Liu, X. Zhou, Z. Wei, X. Xu, K. Liu, Z. Hu, K. Deng *et al.*, "Wafer-scale growth and transfer of highly-oriented monolayer mos2 continuous films," *ACS nano*, vol. 11, no. 12, pp. 12 001–12 007, 2017.

[39] Y. Kim, H. Bark, G. H. Ryu, Z. Lee, and C. Lee, "Wafer-scale monolayer mos2 grown by chemical vapor deposition using a reaction of moo3 and h2s," *Journal of Physics: Condensed Matter*, vol. 28, no. 18, p. 184002, 2016.

[40] P. M. Campbell, A. Tarasov, C. A. Joiner, M.-Y. Tsai, G. Pavlidis, S. Graham, W. J. Ready, and E. M. Vogel, "Field-effect transistors based on wafer-scale, highly uniform few-layer p-type wse 2," *Nanoscale*, vol. 8, no. 4, pp. 2268–2276, 2016.

[41] A. Nourbakhsh, A. Zubair, R. N. Sajjad, A. Tavakkoli KG, W. Chen, S. Fang, X. Ling, J. Kong, M. S. Dresselhaus, E. Kaxiras *et al.*, "Mos2 field-effect transistor with sub-10 nm channel length," *Nano letters*, vol. 16, no. 12, pp. 7798–7806, 2016.

[42] S. B. Desai, S. R. Madhvapathy, A. B. Sachid, J. P. Llinas, Q. Wang, G. H. Ahn, G. Pitner, M. J. Kim, J. Bokor, C. Hu *et al.*, "Mos2 transistors with 1-nanometer gate lengths," *Science*, vol. 354, no. 6308, pp. 99–102, 2016.

[43] W. Yao, D. Xiao, and Q. Niu, "Valley-dependent optoelectronics from inversion symmetry breaking," *Physical Review B*, vol. 77, no. 23, p. 235406, 2008.

[44] Z. Zhu, Y. Cheng, and U. Schwingenschlögl, "Giant spin-orbit-induced spin splitting in two-dimensional transition-metal dichalcogenide semiconductors," *Physical Review B*, vol. 84, no. 15, p. 153402, 2011.

[45] T. Cao, G. Wang, W. Han, H. Ye, C. Zhu, J. Shi, Q. Niu, P. Tan, E. Wang, B. Liu *et al.*, "Valley-selective circular dichroism of monolayer molybdenum disulphide," *Nature communications*, vol. 3, p. 887, 2012.

[46] C.-S. Pang, H. Ilatikhameneh, and Z. Chen, "Gate tunable 2d wse 2 esaki diode by sinx doping," in *2017 75th Annual Device Research Conference (DRC)*. IEEE, 2017, pp. 1–2.

[47] C. D. English, G. Shine, V. E. Dorgan, K. C. Saraswat, and E. Pop, "Improved contacts to mos2 transistors by ultra-high vacuum metal deposition," *Nano letters*, vol. 16, no. 6, pp. 3824–3830, 2016.

[48] F. Ahmed, M. S. Choi, X. Liu, and W. J. Yoo, "Carrier transport at the metal–mos 2 interface," *Nanoscale*, vol. 7, no. 20, pp. 9222–9228, 2015.

[49] Y. Guo, Y. Han, J. Li, A. Xiang, X. Wei, S. Gao, and Q. Chen, "Study on the resistance distribution at the contact between molybdenum disulfide and metals," *ACS nano*, vol. 8, no. 8, pp. 7771–7779, 2014.

[50] A. Allain, J. Kang, K. Banerjee, and A. Kis, "Electrical contacts to two-dimensional semiconductors," *Nature materials*, vol. 14, no. 12, p. 1195, 2015.

[51] K. Majumdar, C. Hobbs, and P. D. Kirsch, "Benchmarking transition metal dichalcogenide mosfet in the ultimate physical scaling limit," *IEEE Electron Device Letters*, vol. 35, no. 3, pp. 402–404, 2014.

[52] K. K. Smithe, C. D. English, S. V. Suryavanshi, and E. Pop, "Intrinsic electrical transport and performance projections of synthetic monolayer mos2 devices," *arXiv preprint arXiv:1608.00987*, 2016.

[53] W. Cao, J. Kang, D. Sarkar, W. Liu, and K. Banerjee, "2d semiconductor fetsprojections and design for sub-10 nm vlsi," *IEEE Transactions on Electron Devices*, vol. 62, no. 11, pp. 3459–3469, 2015.

[54] C. M. Smyth, R. Addou, S. McDonnell, C. L. Hinkle, and R. M. Wallace, "Wse2-contact metal interface chemistry and band alignment under high vacuum and ultra high vacuum deposition conditions," *2D Materials*, vol. 4, no. 2, p. 025084, 2017.

[55] P. Bampoulis, R. van Bremen, Q. Yao, B. Poelsema, H. J. Zandvliet, and K. Sotthewes, "Defect dominated charge transport and fermi level pinning in mos2/metal contacts," *ACS applied materials & interfaces*, vol. 9, no. 22, pp. 19 278–19 286, 2017.

[56] C. Kim, I. Moon, D. Lee, M. S. Choi, F. Ahmed, S. Nam, Y. Cho, H.-J. Shin, S. Park, and W. J. Yoo, "Fermi level pinning at electrical metal contacts of monolayer molybdenum dichalcogenides," *ACS nano*, vol. 11, no. 2, pp. 1588–1596, 2017.

[57] C. Gong, L. Colombo, R. M. Wallace, and K. Cho, "The unusual mechanism of partial fermi level pinning at metal–mos2 interfaces," *Nano letters*, vol. 14, no. 4, pp. 1714–1720, 2014.

[58] A. Khosravi, R. Addou, C. M. Smyth, R. Yue, C. R. Cormier, J. Kim, C. L. Hinkle, and R. M. Wallace, "Covalent nitrogen doping in molecular beam epitaxy-grown and bulk wse2," *APL Materials*, vol. 6, no. 2, p. 026603, 2018.

[59] R. Addou, C. M. Smyth, J.-Y. Noh, Y.-C. Lin, Y. Pan, S. M. Eichfeld, S. Fölsch, J. A. Robinson, K. Cho, R. M. Feenstra *et al.*, "One dimensional metallic edges in atomically thin wse2 induced by air exposure," *2D Materials*, vol. 5, no. 2, p. 025017, 2018.

[60] P. R. Pudasaini, A. Oyedele, C. Zhang, M. G. Stanford, N. Cross, A. T. Wong, A. N. Hoffman, K. Xiao, G. Duscher, D. G. Mandrus *et al.*, "High-performance multilayer wse 2 field-effect transistors with carrier type control," *Nano Research*, vol. 11, no. 2, pp. 722–730, 2018.

[61] B. Liu, Y. Ma, A. Zhang, L. Chen, A. N. Abbas, Y. Liu, C. Shen, H. Wan, and C. Zhou, "High-performance wse2 field-effect transistors via controlled formation of in-plane heterojunctions," *ACS nano*, vol. 10, no. 5, pp. 5153–5160, 2016.

[62] S. Das and J. Appenzeller, "Wse2 field effect transistors with enhanced ambipolar characteristics," *Applied physics letters*, vol. 103, no. 10, p. 103501, 2013.

[63] C. M. Smyth, L. A. Walsh, P. Bolshakov, M. Catalano, R. Addou, L. Wang, J. Kim, M. J. Kim, C. D. Young, C. L. Hinkle *et al.*, "Engineering the palladium–wse2 interface chemistry for field effect transistors with high-performance hole contacts," *ACS Applied Nano Materials*, 2018.

[64] D. Xiao, W. Yao, and Q. Niu, "Valley-contrasting physics in graphene: magnetic moment and topological transport," *Physical Review Letters*, vol. 99, no. 23, p. 236809, 2007.

[65] J. R. Schaibley, H. Yu, G. Clark, P. Rivera, J. S. Ross, K. L. Seyler, W. Yao, and X. Xu, "Valleytronics in 2d materials," *Nature Reviews Materials*, vol. 1, no. 11, p. 16055, 2016.

[66] A. M. Jones, H. Yu, N. J. Ghimire, S. Wu, G. Aivazian, J. S. Ross, B. Zhao, J. Yan, D. G. Mandrus, D. Xiao *et al.*, "Optical generation of excitonic valley coherence in monolayer wse 2," *Nature nanotechnology*, vol. 8, no. 9, p. 634, 2013.

[67] Y. Li, Y. Rao, K. F. Mak, Y. You, S. Wang, C. R. Dean, and T. F. Heinz, "Probing symmetry properties of few-layer mos2 and h-bn by optical second-harmonic generation," *Nano letters*, vol. 13, no. 7, pp. 3329–3333, 2013.

[68] D. Abanin, A. Shytov, L. Levitov, and B. Halperin, "Nonlocal charge transport mediated by spin diffusion in the spin hall effect regime," *Physical review B*, vol. 79, no. 3, p. 035304, 2009.

[69] G. Sallen, L. Bouet, X. Marie, G. Wang, C. Zhu, W. Han, Y. Lu, P. Tan, T. Amand, B. Liu *et al.*, "Robust optical emission polarization in mos 2 monolayers through selective valley excitation," *Physical Review B*, vol. 86, no. 8, p. 081301, 2012.

[70] L. Yang, N. A. Sinitsyn, W. Chen, J. Yuan, J. Zhang, J. Lou, and S. A. Crooker, "Long-lived nanosecond spin relaxation and spin coherence of electrons in monolayer mos 2 and ws 2," *Nature Physics*, vol. 11, no. 10, p. 830, 2015.

[71] X. Song, S. Xie, K. Kang, J. Park, and V. Sih, "Long-lived hole spin/valley polarization probed by kerr rotation in monolayer wse2," *Nano letters*, vol. 16, no. 8, pp. 5010–5014, 2016.

[72] H. U. Baranger and A. D. Stone, "Geometrical effects on the hall resistance in ballistic microstructures," *Surface Science*, vol. 229, no. 1-3, pp. 212–215, 1990.

[73] C. Ford, S. Washburn, M. Büttiker, C. Knoedler, and J. Hong, "Influence of geometry on the hall effect in ballistic wires," *Physical review letters*, vol. 62, no. 23, p. 2724, 1989.

[74] J. Kim, C. Jin, B. Chen, H. Cai, T. Zhao, P. Lee, S. Kahn, K. Watanabe, T. Taniguchi, S. Tongay *et al.*, "Observation of ultralong valley lifetime in wse2/mos2 heterostructures," *Science advances*, vol. 3, no. 7, p. e1700518, 2017.

[75] K. Y. Camsari, S. Ganguly, and S. Datta, "Modular approach to spintronics," *Scientific reports*, vol. 5, 2015.

[76] S. Hong, S. Sayed, and S. Datta, "Spin circuit representation for the spin hall effect," *IEEE Transactions on Nanotechnology*, vol. 15, no. 2, pp. 225–236, 2016.

[77] X. Li, J. T. Mullen, Z. Jin, K. M. Borysenko, M. B. Nardelli, and K. W. Kim, "Intrinsic electrical transport properties of monolayer silicene and mos 2 from first principles," *Physical Review B*, vol. 87, no. 11, p. 115418, 2013.

[78] K. Kaasbjerg, J. H. Martiny, T. Low, and A.-P. Jauho, "Symmetry-forbidden intervalley scattering by atomic defects in monolayer transition-metal dichalcogenides," *Physical Review B*, vol. 96, no. 24, p. 241411, 2017.

[79] H. Liu, J. Chen, H. Yu, F. Yang, L. Jiao, G.-B. Liu, W. Ho, C. Gao, J. Jia, W. Yao *et al.*, "Observation of intervalley quantum interference in epitaxial monolayer tungsten diselenide," *Nature communications*, vol. 6, p. 8180, 2015.

[80] C. Zhang, Y. Chen, A. Johnson, M.-Y. Li, L.-J. Li, P. C. Mende, R. M. Feenstra, and C.-K. Shih, "Probing critical point energies of transition metal dichalcogenides: surprising indirect gap of single layer wse2," *Nano letters*, vol. 15, no. 10, pp. 6494–6500, 2015.

[81] T. Olsen and I. Souza, "Valley hall effect in disordered monolayer mos 2 from first principles," *Physical Review B*, vol. 92, no. 12, p. 125146, 2015.

[82] Y.-T. Chen, S. Takahashi, H. Nakayama, M. Althammer, S. T. Goennenwein, E. Saitoh, and G. E. Bauer, "Theory of spin hall magnetoresistance," *Physical Review B*, vol. 87, no. 14, p. 144411, 2013.

[83] G. L. Frey, R. Tenne, M. J. Matthews, M. Dresselhaus, and G. Dresselhaus, "Raman and resonance raman investigation of mos 2 nanoparticles," *Physical Review B*, vol. 60, no. 4, p. 2883, 1999.

[84] H. Li, Q. Zhang, C. C. R. Yap, B. K. Tay, T. H. T. Edwin, A. Olivier, and D. Baillargeat, "From bulk to monolayer mos2: evolution of raman scattering," *Advanced Functional Materials*, vol. 22, no. 7, pp. 1385–1390, 2012.

[85] C. Lee, H. Yan, L. E. Brus, T. F. Heinz, J. Hone, and S. Ryu, "Anomalous lattice vibrations of single-and few-layer mos2," *ACS nano*, vol. 4, no. 5, pp. 2695–2700, 2010.

[86] B. Radisavljevic, A. Radenovic, J. Brivio, i. V. Giacometti, and A. Kis, "Single-layer mos2 transistors," *Nature nanotechnology*, vol. 6, no. 3, pp. 147–150, 2011.

[87] S. Fukami, T. Anekawa, C. Zhang, and H. Ohno, "A spin–orbit torque switching scheme with collinear magnetic easy axis and current configuration," *Nature Nanotechnology*, vol. 11, no. 7, p. 621, 2016.

[88] L. Liu, O. Lee, T. Gudmundsen, D. Ralph, and R. Buhrman, "Current-induced switching of perpendicularly magnetized magnetic layers using spin torque from the spin hall effect," *Physical review letters*, vol. 109, no. 9, p. 096602, 2012.

[89] L. You, O. Lee, D. Bhowmik, D. Labanowski, J. Hong, J. Bokor, and S. Salahuddin, "Switching of perpendicularly polarized nanomagnets with spin orbit torque without an external magnetic field by engineering a tilted anisotropy," *Proceedings of the National Academy of Sciences*, vol. 112, no. 33, pp. 10 310–10 315, 2015.

[90] G. Yu, P. Upadhyaya, Y. Fan, J. G. Alzate, W. Jiang, K. L. Wong, S. Takei, S. A. Bender, L.-T. Chang, Y. Jiang *et al.*, "Switching of perpendicular magnetization by spin–orbit torques in the absence of external magnetic fields," *Nature nanotechnology*, vol. 9, no. 7, p. 548, 2014.

[91] C. J. Ciccarino, T. Christensen, R. Sundararaman, and P. Narang, "Dynamics and spin-valley locking effects in monolayer transition metal dichalcogenides," *Nano letters*, vol. 18, no. 9, pp. 5709–5715, 2018.

[92] P. Dey, L. Yang, C. Robert, G. Wang, B. Urbaszek, X. Marie, and S. Crooker, "Gate-controlled spin-valley locking of resident carriers in wse 2 monolayers," *Physical review letters*, vol. 119, no. 13, p. 137401, 2017.

[93] E. Barre, J. A. C. Incorvia, S. H. Kim, C. J. McClellan, E. Pop, H.-S. P. Wong, and T. F. Heinz, "Spatial separation of carrier spin by the valley hall effect in monolayer wse2 transistors," *Nano letters*, vol. 19, no. 2, pp. 770–774, 2019.

[94] M. Popinciuc, C. Józsa, P. Zomer, N. Tombros, A. Veligura, H. Jonkman, and B. Van Wees, "Electronic spin transport in graphene field-effect transistors," *Physical Review B*, vol. 80, no. 21, p. 214427, 2009.

[95] S. O. Valenzuela and M. Tinkham, "Direct electronic measurement of the spin hall effect," *Nature*, vol. 442, no. 7099, p. 176, 2006.